

---

# Attosecond metrology of multi-PHz currents in solids

Manish Garg

---



München 2017



---

# Attosecond metrology of multi-PHz currents in solids

Manish Garg

---

Dissertation  
an der Fakultät für Physik  
der Ludwig-Maximilians-Universität  
München

vorgelegt von  
Manish Garg  
aus Shahdol, India

München, den 15.11.2016

Erstgutachter: Prof. Dr. Ferenc Krausz

Zweitgutachter: Prof. Dr. Christian Spielmann

Tag der mündlichen Prüfung: 19.01.2017

*In the loving memory of my grandmothers late Smt. Rama Devi Garg & late Smt. Kamla  
Pandey*

# Zusammenfassung

Beherrschung der Elektronenbewegung durch synthetisierte elektrische Felder bildet die Grundlage moderner Informations und Signalverarbeitung. Die Rechengeschwindigkeit (bei Elektronik im allgemeinen) ist dabei begrenzt durch die Rate, mit der Ströme (elektronische Bewegung) durch elektronische Bauteile, meist Transistoren, an und ausgeschaltet werden können. Aufgrund der sehr hohen Streurrate von Elektronen ist elektronische Bewegung in konventionellen Komponenten zumeist inkohärent, weshalb bei diesen nur ein binärer Betrieb, d.h. mit starken und schwachen Strömen, möglich ist. In dieser Doktorarbeit wird die Messung und Steuerung elektronischer Ströme mit Frequenzen von bis zu  $\sim 8\text{PHz}$  präsentiert, welche im Leitungsband eines Dielektrikums ( $\text{SiO}_2$ ) mithilfe optischer Laserpulse induziert wurden. Die Bewegung der Elektronen kann als kohärent betrachtet werden, wenn die Dauer des Laserpulses kurz im Vergleich zur quantenmechanischen Dekohärenzzeit im inneren eines Festkörpers ( $\sim$  wenige fs) ist. Auf kohärenter Elektronenbewegung basierende Elektronik kann sehr viel mehr Information auf einmal verarbeiten, da die Phase der Elektronen während des Betriebs als zusätzliches Informationsmedium genutzt werden kann.

Das Bestreben durch Licht elektrische Ströme zu induzieren fand seinen Anfang um 1900, als K.F.Braun, der Erfinder der Leistungsgleichrichterdiode, erste Schritte in diese Richtung unternahm. Ultrakurze Laserpulse bieten die Möglichkeit in Festkörpern elektronische Bewegung mit sehr hoher Oszillationsfrequenz zu induzieren; bedauernswerter Weise wurde eine genauere Untersuchung der Laser-Festkörperwechselwirkung lange durch laserbedingten Schaden am Kristall verhindert. Neuerdings, bedingt durch verbesserte Fertigungstechniken sind ultradünne Proben schnell und leicht verfügbar und technische Innovationen haben die Laserpulsdauer auf wenige fs reduziert; beides wichtige Entwicklungen um Schäden am Festkörper zu reduzieren.

Vor einigen Jahren wurden mithilfe optisch induzierter Ströme EUV-Strahlung mit Frequenzen bis zu  $10\text{PHz}$  in  $\text{SiO}_2$  erzeugt. Die zugrunde liegende Bewegung der Elektronen, ob vertikale Übergänge entlang der Energiehierarchie von  $\text{SiO}_2$  oder laterale Bewegung (Streuung) entlang des Dispersionsprofils der Elektronen war jedoch unklar. Hier wird gezeigt das die Bewegung der Elektronen in der Energielandschaft des Leitungsbandes (Intrabandströme), die gleiche Bewegung wie in konventioneller Elektronik, der Grund für die Emission von EUV-Strahlung ist. Es wird gezeigt das die streuungsbasierte Emission von EUV-Strahlung aus  $\text{SiO}_2$  signifikant andere zeitliche Merkmale im Vergleich zu rekollisionsbasierten Emission kohärenter EUV-Strahlung aus Edelgasen aufweist. Diese Arbeit präsentiert die Möglichkeit zur direkten, Attosekunden genauen Messung, zeitlichen Beschränkung und Wellenformsteuerung der Intrabandströme in Festkörpern. Damit etabliert sie eine neue Plattform für kohärente multi-PHz Elektronik und neuartige Wege zur Untersuchung von Elektronenbewegung und der Struktur von Festkörpern auf atomaren Skalen. Kollektive Elektroneneigenschaften bei solchen Frequenzen, wie zum

Beispiel dynamische Leitfähigkeit und Stromdichte, wurden gemessen und dabei ein Vorzeichenwechsel der dynamischen Leitfähigkeit innerhalb von knapp 30 as gezeigt. Phasenkohärenz von Intradbandströmen, welche direkt mit der CEP von isolierten EUV-Pulsen korrelieren wird ebenfalls erstmals demonstriert. Als ein Ergebnis dieser Arbeit wurden die ersten aus Festkörpern erzeugten isolierten Attosekundenpulse gemessen.

In einem neuartigen System aus Xenonatomen werden sich auf sub-Femtosekunden Skalen entwickelnde Quanteninterferenzen durch Attosekundenpulse nutzende, spektroskopische Pump-Probe Messungen untersucht. Diese Experimente bilden ein stabiles Fundament zur Untersuchung von Quantenkohärenz in komplexeren Systemen mithilfe von optischen Attosekundenpulsen.



# Abstract

Command over electron motion by synthesized electric fields forms the basis for modern computing, information and signal processing. The rate of computation (electronics in general) is adjudged by the speed at which currents (electronic motion) can be turned on and off through an electronic component per se a transistor. Electronic motion in conventional electronics is primarily incoherent due to very high scattering rate of electrons implying operation of electronics only in a binary mode i.e. high and low currents. In this thesis measurement and control of electric currents induced by optical driving laser pulses in the conduction band of a dielectric material ( $\text{SiO}_2$ ) extending in frequency up to  $\sim 8$  PHz is presented. Driving electrons with ultrashort laser pulses with duration shorter than their quantum dephasing times ( $\sim$  few fs) inside bulk materials essentially make the electron motion coherent. Electronics operating with underlying coherent electron motion carries way more information as the conserved phases of electrons during its operation can be all sources of information.

Human endeavour towards light induced electric currents goes back to 1900s when K. F. Braun the inventor of rectifying diode made pioneering efforts in this direction. Ultrafast laser pulses have the capability to induce electronic motion inside solids at a very high oscillating frequency; unfortunately interaction of laser pulses with solids have been eclipsed for a long time by the material damage on exposure to laser pulses. However, lately with advanced fabrication techniques ultrathin samples are readily available and technological innovation have pushed the pulse duration of laser pulses down to only few fs; both of which are important to mitigate damage.

Generation of EUV radiation extending in frequency upto 10 PHz by optically induced currents inside  $\text{SiO}_2$  was demonstrated a couple of years back, however underlying motion of electrons, whether is was vertical transitions along the energy hierarchy of  $\text{SiO}_2$  or lateral motion (scattering) along the dispersion profile of electronic bands was not clear. Its found that motion of electrons in the energy landscape of conduction bands (intraband current) which is the same as in conventional electronics is the cause behind observation of EUV radiation. The scattering dependent emission of EUV radiation from  $\text{SiO}_2$  is shown to bear significantly different temporal features compared to re-collision based generation of coherent EUV emission from noble gases. This thesis presents the capabilities of direct attosecond probing, confinement and waveform control of the intraband currents inside solids and establishes a new platform for multi-PHz coherent electronics and novel routes for fundamental study of electron dynamics and structure of condensed matter on the atomic scale. Properties of electrons at such frequencies, such as dynamic conductivity and current density have been measured, a switch in the dynamic conductivity has been shown to occur at a timescale close to 30 as. Phase coherence of intraband currents which is also directly linked to the CEP of isolated EUV attosecond pulses is also presented here for the first time. As an outcome of this work generation of first isolated attosecond pulses

from a bulk solid is demonstrated.

Ultrafast quantum interferences evolving on a time scale faster than 1 fs in a novel system of Xe atoms are studied by performing pump-probe spectroscopic measurements utilizing optical attosecond pulses, these experiments form a firm ground for studying quantum coherences in more complex systems with the unique tool of optical attosecond pulses.



# Contents

<b>Summary</b>	<b>vi</b>
<b>Abstract</b>	<b>ix</b>
<b>Introduction</b>	<b>xi</b>
<b>1 Strong field processes in atoms and solids</b>	<b>9</b>
1.1 Light matter interaction: Fundamentals . . . . .	10
1.2 Keldysh Parameter: Tunnel and Multi-photon ionization . . . . .	11
1.3 Attosecond Science . . . . .	13
1.4 Ultrashort laser-pulse interaction in dielectrics . . . . .	15
<b>2 Experimental setup: Laser-system and light field synthesis</b>	<b>17</b>
2.1 Laser-system . . . . .	17
2.1.1 Carrier envelope phase stabilization . . . . .	20
2.2 Light Field Synthesis . . . . .	22
2.3 Overview of experimental set-up at AS1 beamline . . . . .	23
2.4 Attosecond streaking: Complete characterization of optical pulses . . . . .	24
<b>3 Coherent extreme ultraviolet radiation from bulk solids: Polarization spectroscopy of electronic bands</b>	<b>29</b>
3.1 Introduction . . . . .	29
3.2 Experiment . . . . .	30
3.3 HH spectroscopy of solids . . . . .	37
3.4 Conclusions . . . . .	39
<b>4 Real-time tracing and attosecond control of multi-PHz electric currents in solids</b>	<b>43</b>
4.1 Introduction . . . . .	43
4.2 Experimental Details . . . . .	43
4.3 Reconstruction of EUV and driving optical pulses by PCGPA . . . . .	44
4.4 Absolute calibration of delay unit . . . . .	50
4.5 Quantum mechanical modelling of EUV emission in SiO <sub>2</sub> . . . . .	53
4.5.1 Semiclassical model of HHG in SiO <sub>2</sub> . . . . .	55

4.5.2	Time resolved simulation of EUV emission . . . . .	56
4.6	Interband Vs. Intraband dominated dynamics in SiO <sub>2</sub> . . . . .	56
4.6.1	Effect of driving laser intensity on chirp of EUV emission . . . . .	61
4.6.2	Effect of strength of Coulomb interaction on emission strength of the two mechanisms and their temporal characteristics . . . . .	61
4.6.3	Effect of sample crystallinity on mechanism of EUV generation . . . . .	61
4.7	Probing nonlinearity in EUV emission, steering intraband currents in SiO <sub>2</sub>	64
4.8	Controlling the frequency, duration, and structure of intraband currents and attosecond EUV bursts in SiO <sub>2</sub> . . . . .	70
4.9	Spatial dynamics of electrons . . . . .	70
4.10	Nonlinear current density and dynamic conductivity . . . . .	73
<b>5</b>	<b>Phase coherence of Multi-PHz currents in SiO<sub>2</sub></b>	<b>79</b>
5.1	CEP of isolated attosecond pulses generated in SiO <sub>2</sub> . . . . .	79
5.2	Dispersion control of CEP of EUV pulses . . . . .	80
5.3	Origin of fine spectral fringes ( ~ 0.35 eV) in ATI-EUV interference . . . . .	85
5.4	Dependence of CEP of EUV pulses on CEP of driving laser pulses . . . . .	85
<b>6</b>	<b>Ultrafast dephasing of field-induced polarization in SiO<sub>2</sub></b>	<b>93</b>
6.1	Results and Discussion . . . . .	94
<b>7</b>	<b>Optical attosecond pump-probe spectroscopy: Quantum coherences in Xe</b>	<b>99</b>
7.1	Introduction . . . . .	99
7.2	Experimental Details . . . . .	100
7.3	Observed Quantum coherences in Xe . . . . .	102
7.4	Attosecond control over Quantum coherences . . . . .	107
7.5	Conclusions . . . . .	109
<b>8</b>	<b>Conclusions and Outlook</b>	<b>111</b>
<b>A</b>	<b>Reflectivity of Au mirror and transmission curve of 150nm Al</b>	<b>113</b>
<b>B</b>	<b>Calibration of energy axis of TOF spectrometer</b>	<b>114</b>
<b>C</b>	<b>Methodical comparison of spectral phase from simulation and measure- ment set-up</b>	<b>115</b>
C.0.1	Dispersion properties of SiO <sub>2</sub> . . . . .	116
<b>D</b>	<b>Principal Component Generalised Projections Algorithm (PCGPA)</b>	<b>118</b>
<b>E</b>	<b>Calibration of VUV spectrometer</b>	<b>121</b>

F Data Archiving

122

# Introduction

Light has remained an essential tool to investigate matter starting from the development of first compound microscope by Robert Hooke in 1665 when he coined the term *cell* for the first time to describe tiny biological organisms which were possible to observe by a 30X microscope. Interim to this new discovery of microscopy was the advancement of the field of astronomy by Galileo in 1613 who first used the telescope to garner information about moon's surface and revolution of earth around sun. Light has since then been used in all fields of research to study both microscopic and distant objects.

Demonstration of first working laser by Theodore Maiman in 1960 [1] has revolutionised the field of microscopic investigation of matter. Lasers owing to their high degree of spatial and temporal coherence are much more superior than incoherent radiation of light produced by discharge in a noble gas long used by spectroscopists before the invention of laser to study electronic structure of matter by absorption of discrete spectral parts from a broader input spectrum. Continuous wave lasers as demonstrated by Maiman have been extensively used by biologists to trace biological activity by tracing fluorescence (emission) generated by exciting a biological tracer. Multi-photon microscopy [2] has emerged as a powerful tool to this end which exploits the temporal coherence property of lasers allowing the biological sample under study to absorb more than one photon at a time. Nonlinear absorption of photons also increase the spatial resolution of the microscope as the fluorescence in this case will be observed at smaller wavelengths than the exciting photon energy.

Human perception of ultrafast processes in the nature is limited by the resolution of eyes which is dictated by their blinking rate which is close to  $\sim 0.1$ s. Human's thrust to capture ultrafast processes in nature goes back to the year 1878 when Eadweard Muybridge first attempted to capture ultrafast locomotion of animals which is not perceivable by humans for example the motion of legs of a horse while galloping. In 1878 Muybridge used fast mechanical shutters in front of his camera to increase the temporal resolution in order to be able to capture such motions. Unfortunately, Muybridge's idea cannot be extended to capture processes faster than few milliseconds as there can be no mechanical shutters faster than 1 ms, hence a new technique had to be developed which doesn't use mechanical shutters to increase the temporal resolution. After the demonstration of first laser in 1960 efforts were fast in creating ultrashort laser flashes to fulfil this need. Even though CW lasers were useful for many applications to study matter they were not appropriate to study ultrafast processes in matter until the first pulsed laser sources using Titanium doped sapphire as a gain medium were demonstrated in 1982 by Peter F. Moulton at MIT,

USA [3]. Pulsed laser sources were accomplished by devising a technique to pack millions of photons in a very short duration time, which was first implemented by using an electrical modulator.

Classical analogue of an emerging quantum phenomena is best described by a wavepacket which is formed by coherent superposition of many quantum states involved in the quantum phenomena, the time scale of dynamics of this wavepacket is determined by the energy difference ( $\Delta E$ ) of the involved quantum states. Rotation of molecules around their centre of mass unfolds on the timescale of several picoseconds as the energy difference between states which differ in their angular momentum quantum number  $L$  is  $\sim 1$ -50 meV. Similarly the vibrational dynamics of molecules unfolds on the order of few tens to hundred of fs as energy difference between vibration states is  $\sim 200$ -500 meV. Picosecond and femtosecond durations long laser pulses have now been available by commercial laser systems since last two decades. Unfortunately, attosecond laser pulses which could enable us to study electron dynamics inside atoms or molecules unfolding on the order of few to several hundreds of attoseconds are not commercially available and have to be generated by other techniques involving highly nonlinear interaction between ultrafast lasers and matter. In-depth understanding of microscopic dynamics is a key prerequisite to precisely controlling its dynamics which has been rigorously endeavoured in the last decades. Laser control of matter being directed to a specific light-matter interaction output is indeed possible by exercising control over some specific parameters of laser pulse which in turn can control coupling of quantum states and hence the classically detected dynamics of the wavepacket.

### Observation of atomic and electronic motion in real time

Dynamics of bond breaking and bond formation is central to understanding of chemical reactions. Bond formation and breaking can be described as a variant of vibrational dynamics, bonds can break between two atoms if they vibrate very fast around their centre of mass i.e. they lie in a high lying vibration state close to continuum ( $\nu \sim \infty$ ). Bond formation on the other hand has been described to go through an energy barrier or a transition state by Arrhenius. Motion of atoms of Na and Br while forming a bond between them has been probed by Ahmed Zewail and his co-workers, Na moving in the energy landscape of NaBr has been monitored by looking into the variation of intensity of Na  $D$  lines on the timescale of the phenomena. The kinetic theory of bond formation as proposed by Arrhenius was verified as between Na, Br and NaBr there is indeed a high-lying transition state  $NaBr^{++}$  [4][5]. Ahmed Zewail was awarded Nobel prize in year 1999 for his efforts in time resolving atomic dynamics during chemical reactions. Dynamics ensuing interaction of ultrashort intense laser pulses with molecules has been followed in real time, motion of  $H^+$  ion along the energy contour of unbound electronic level of  $H_2^+$  has been followed.  $H_2$  molecule on interaction with laser pulses is ripped off one of its electrons due to sudden ionization and the molecule makes a transition from electronic ground state of  $H_2$  to bound electronic ground state of  $H_2^+$ , an identical laser pulse coming at a certain delay with the pulse triggering the dynamics can bring the  $H_2^+$  ion to an unbound electronic state from where it fragments into  $H^+$  ion and H atom. The kinetic energy of generated  $H^+$  depends

on spatial location of its excitation on the energy contour of dissociative electronic state. Measuring kinetic energy of the  $H^+$  ion at different moments of excitation by second laser pulses enabled Paul Corkum and his co-workers to reconstruct  $H^+$  ion motion in real time [6]. The spatial resolution of this demonstrated technique was  $< 0.1\text{\AA}$ . Real time observation of atomic motion inside molecules including some of biological importance became a reality after ready availability of commercial laser systems easily producing pulses close to  $\sim 5\text{-}10$  fs [7][8]. However, electronic motion remained out of reach of scientists until a new technique to generate attosecond pulses utilising extremely nonlinear interaction of matter with laser pulses was demonstrated by Ferenc Krausz and his co-workers in the year 2001 [9]. A flurry of scientific activity on observing and controlling electron dynamics has started since then. Record achievement of generating attosecond pulses as short as 80 as was demonstrated in 2008 [10]. It has become possible to observe tunnelling of electrons through the Coloumbic barrier of atoms [11]; decay of electron core-hole dipole [12]; motion ensuing quantum interference of electrons between different spin-orbit states in Kr atoms in real time [13].

### Electron dynamics in condensed phase

Microscopic structure of condensed phase systems have long been studied by the techniques of scanning and tunnelling electron microscopy, X-ray and neutron diffraction. However, temporal studies of the electron dynamics which affect several interesting processes in solids such as phase transitions, conduction of electricity through them have not been possible till the early 1980s even though ultrafast laser pulses were available this was mainly due to dispersive and absorption characteristics of solids. Fabrication of ultrathin samples of solids eventually became readily available to scientists (after 1980s) and the pursuit to study electron dynamics inside bulk solids has not slowed down since then. Optical techniques which offer to record dynamics of electrons in solids by tracking dynamics of emitted, reflected or transmitted radiation have been driving this field of research. Onset of Coloumbic screening among electrons has been studied in real time in a electron-hole plasma generated by resonant absorption of infra-red photons in GaAs[14]. Also the motion of a quasiparticle *polaron* has been studied inside GaAs by recording changes in the THz pulse reflectivity as a function of its interaction with an infra-red pulse[15]. First application of attosecond pulses to study electron dynamics in solids was done in the year 2007[16], wherein attosecond pulses centred at 120 eV were focused on a sample consisting of several layers of Tungsten on a substrate, the photoelectrons hence generated were probed by an infra-red pulse and the delay reconstructed on arrival of photoelectrons from different layers of the sample was closely correlated to electronic excursion through the multi-layered sample. Dynamics of lattice atoms while undergoing phase transitions on a multidimensional energy landscape of  $\text{VO}_2$  has been studied by recording time-resolved diffraction patterns with 100 fs long electron pulses[17]. Efforts to create a 4D space-time movie of motion of atoms inside solids utilising attosecond electron pulses are currently being pursued[18].

### High-harmonic generation and spectroscopy of dielectrics

Inducing highly nonlinear polarization in atoms and molecules by laser pulses and analysing the emerging radiation has become an established field of spectroscopy commonly known as high harmonic spectroscopy which involves high-harmonic generation (HHG) understood via the three step model of Paul Corkum[19]. This nonlinear polarization based spectroscopic technique can reveal several features of electronic levels of atoms and molecules hidden in the emitted spectrum. Meticulous study of the change of HH spectra as a function of one of the parameters of a laser pulse can reveal the shape of the wavefunction of the electronic levels involved in HHG. HHG requires recombination of tunnel ionized electronic wavepacket to recombine with its parent ion, this intuitively imitates the standard technique of collision physics where scientists infer the structure of a molecular entity by colliding it with an atomic or ionic beam. The molecular orbital of the ground electronic state of  $N_2$ [20] was reconstructed by measuring HH spectra for different orientations of  $N_2$  molecule with respect to the laser polarization axis, as here indeed the tunnel ionised electron collides with the ion of  $N_2$ . Tunnel ionization of a molecule by a laser pulse couples several electronic levels of the molecule, a replica of this information is engraved in the HH spectrum. Relative phases in this quantum interference of electronic levels can be extracted as was demonstrated for  $CO_2$  molecule[21]; where the relative phases between multiple ionization channels was extracted.

Inducing nonlinear polarization (higher than 5th order) deep inside solids has not been easy due to damage caused to them by the laser pulses. Solids inherently suffer from linear absorption by laser pulses which can be mitigated by thinning down their thickness as it reduces the chances due to heat damage and also using laser pulses whose central frequency comfortably lies lower than the band gap of solids under study. In 2011 observation of HH from a nonlinearly polarized solid ZnO ( $E_g \sim 3eV$ ) was first reported which was driven by a mid infra-red laser pulse[22]. The HHG mechanism in solids is fundamentally different from gases owing to its high density of atoms and periodicity. HH spectra extending upto the extreme ultraviolet (EUV) range has been recently demonstrated by our group[23] and the information imprinted in the HH spectra has been used to extract electronic structural information of  $SiO_2$ . Fine details of the dispersion profile of first conduction band of  $SiO_2$  was retrieved. The demonstrated proof-of-concept experiments have opened a new avenue for polarization based spectroscopic techniques in solids. The capability to capture fine details varying on the spatial scale of  $\sim 0.1\text{\AA}$  connotes to a very high spatial resolution being offered by such a technique.

### Coherent Electronics

Esaki and Tsu in their seminal paper in 1969 [24] predicted the possibility of generating coherent THz radiation by electrons oscillating periodically in presence of a DC field inside an artificially developed semiconductor superlattice with a long range periodicity; this was achievable by growing alternating layers of wide and narrow bandgap semiconductors. Grasping the fact that emerging THz radiation is the macroscopic marker of underlying mi-

croscopic currents generated by electrons in the artificial structure opened up new routes to following electron dynamics inside solids. The recent demonstration of capability to generate coherent EUV radiation out of SiO<sub>2</sub> connotes to extremely fast underlying electric currents whose frequency spans in the range of several PHz and pushes the frontier of frequency of electron oscillations (current) from THz to several PHz. Moreover, as the demonstrated coherent nature of EUV emission connotes that underlying electron oscillations or motion inside solids is also coherent which is in contrast to motion of electrons in electronic circuits where they primarily are incoherent due to the randomness in their relative phases caused by frequent collision with other electrons and the lattice. Driving electrons with ultrashort laser pulses whose half-cycle variation is faster than quantum dephasing time in solids immediately overcomes the barrier of driving electrons coherently inside solids. Light-driven coherent electronics does not seem to be a distant future.

### Multi-Petahertz Electronic Metrology

The basic prerequisite to advance electronics to previously inaccessible frequency ranges is the establishment of a metrology which allow scientists to trace electronic function inside electronic circuits in real time and on relevant time scales. In this work we demonstrate an electronic meteorology technique which allows us to trace electronic motion in the energy landscape of solids in real time. This work demonstrates the advancement of electronic metrology into the multi-PHz range, a regime that earlier techniques cannot attain. To do so, we exploited the time-resolving power of the most established tool in attosecond science, the attosecond streak camera [25][26], to trace the time structure of extreme ultraviolet radiation emerging from a strong field driven solid. As a first application of measuring real electric currents in solids, we have deciphered the underlying nature of electronic motion pertinent to EUV emission.

In the following we briefly outline the contents of this thesis.

- Chapter 1 of this thesis presents basics of light-matter interactions very briefly. Electron-hole dynamics in a semiconductor/dielectric on interaction with an ultrashort laser pulse is also discussed succinctly.
- Details of experimental set-up in AS1 laboratory at Max Planck Institute for Quantum Optics is presented in chapter 2; which includes description of carrier envelope phase (CEP) stable laser system in AS1. We give an overview the conceptual framework of generating isolated attosecond pulses by HHG process in noble gases and their characterization by the technique of attosecond streaking. Generating field-tailored light pulses is at the core of the work presented in this thesis, to this end a 2<sup>nd</sup> generation light-field-synthesizer (LFS) was used and the light-pulses were synthesized and characterised by attosecond streaking; a brief overview of workings of LFS are provided in chapter 2.
- Chapter 3 briefly summarises a new nonlinear polarization based spectroscopic technique to reconstruct the band structure of dielectric materials. Its based on gen-

eration of coherent extreme ultraviolet generation from bulk solids ( $\text{SiO}_2$ ). Several testimonial comparison between experimentally measured spectra and the ones simulated from theory connote to one dominant mechanism of EUV generation. Spectral measurements may not unambiguously reveal the mechanism behind EUV generation from  $\text{SiO}_2$  which calls for time-resolved measurements of the induced nonlinear polarization inside  $\text{SiO}_2$ . The chapter presents multiple experimental results which support coherent nature of EUV emission from  $\text{SiO}_2$  and also the superiority of EUV emission from  $\text{SiO}_2$  compared to standard gas sources used routinely in the lab for EUV generation. Spectral control of EUV emission is demonstrated by using optical attosecond pulses which is not possible when long duration pulses are used. Even though a major part of the work presented in this chapter has been the subject of another PhD thesis [27], nevertheless foremost results are presented to provide a firm introduction for the work to be presented in chapters 4, 5 and 6.

- Time resolved experiments which help us unveil the dynamics underlying EUV emission in  $\text{SiO}_2$  are presented in chapter 4 of this thesis. Two different models of EUV emission are compared, a comparison of EUV emission mechanism by a noble gas in identical energy region as in  $\text{SiO}_2$  experiment has been performed and the two mechanisms are found to contrast each other significantly. Generation of isolated attosecond pulses which is deemed to be a critical milestone in the field of HHG from solids from the work of other groups is demonstrated here for the first time. The mechanism governing EUV emission from  $\text{SiO}_2$  is found to be of the same nature as that of electronic motion in semiconductors in conventional electronics, the validation of this fact from our time-resolved experiments has granted us the access to the dynamic variation of current density and nonlinear conductivity in  $\text{SiO}_2$ . The measured dynamic nonlinear conductivity is 20 orders of magnitude higher than the static conductivity of  $\text{SiO}_2$  and the magnitude of current density is an order of magnitude higher than the measurement at sub-PHz current density in the past.
- Electrons can be transported at multi-PHz frequency in  $\text{SiO}_2$  generating microscopic electric currents as demonstrated in chapter 4. Envelope and frequency sweep of this current is retrievable from our experiments, however phase coherence (field reproducibility) of this current in every shot of the laser pulse is not obvious. In chapter 5 we demonstrate for the first time field reproducibility of this microscopic current which is inherently linked to the carrier envelope phase of EUV attosecond pulses in  $\text{SiO}_2$ . Attosecond streaking is a powerful field characterization technique but it fails to provide information of absolute phase of EUV attosecond pulses. Efforts are currently underway to experimentally access the absolute phase of EUV attosecond pulses.
- Chapter 6 of this thesis presents a conceptual framework for studying the time it takes for electron-hole pairs generated ensuing excitation by laser pulse to go out of phase with respect to each other. The dephasing of induced polarization between electron-hole pairs conceivably arises due to strong correlation among them and their

scattering from lattice sites. Experiments directed towards these efforts should look into the spectral region which comfortably lies in the polarization domain between electron-hole pairs i.e. below the bandgap of solids. First experiments to this end have been performed and this chapter presents simulations which support presence of ultrashort dephasing time in the relaxation of electron-hole pairs.

- Chapter 7 of this thesis presents coherent control of quantum coherences in atoms of Xe by optical attosecond pulses. Interference among several electronic levels can be initiated by exciting a quantum system with coherent light, the ensuing dynamic coherent oscillations between these levels can be probed by the replica of pulse exciting the coherence. The quantum interference among electronic levels has been shown to be controllable by intensity of the light pulse exciting the system, which primarily commands the initial phase of the generated electronic wavepacket. We demonstrate first optical attosecond pump-probe spectroscopy of a system which forms a basis for future experiments probing electronic coherences in more complex systems.
- Conclusion and outlook for future work are discussed in chapter 8.

#### List of publications in the context of the work presented in this thesis

- **M. Garg**, M. Zhan, T. T. Luu, H. Lakhota, T. Klostermann, A. Guggenmos, and E. Goulielmakis. *Multi-petahertz electronic metrology*, Nature, 359-363, **538** (2016) .
- T. T. Luu\*, **M. Garg\***, S. Y. Kruchinin, A. Moulet, M. T. Hassan, and E. Goulielmakis. *Extreme ultraviolet high-harmonic spectroscopy of solids*, Nature, 498-502, **521** (2015)

\* Authors with equal contribution.

#### Further publications of the author

- M. Th. Hassan\*, T. T. Luu\*, A. Moulet, O. Razskazovskaya, P. Zhokhov, **M. Garg**, N. Karpowicz, A. M. Zheltikov, V. Pervak, F. Krausz, and E. Goulielmakis. *Optical attosecond pulses and tracking the nonlinear response of bound electrons*, Nature, 530, **66** (2016)).
- A. Moulet, J. B. Bertrand, A. Jain, **M. Garg**, T. T. Luu, A. Guggenmos, S. Pabst, F. Krausz, and E. Goulielmakis. *Attosecond Pump-Probe Measurement of an Auger Decay*, International Conference on Ultrafast Phenomena (2014)
- **M. Garg**, A. K. Tiwari, and D. Mathur. *Quantum dynamics of proton migration in H<sub>2</sub>O dications: H<sub>2</sub><sup>+</sup> formation on ultrafast timescales*, J. Chem. Phys., 024320, **136** (2012)

- **M. Garg**, A. K. Tiwari, and D. Mathur. *Quantum Dynamics of  $H_2^+$  in Intense Laser Fields on Time-Dependent Potential Energy Surfaces*, J. Phys. Chem., 8762-8767, **116** (2012)
- K. Dota, **M. Garg**, A. K. Tiwari, J. A. Dharmadhikari, A. K. Dharmadhikari and D. Mathur. *Intense two-cycle laser pulses induce time-dependent bond hardening in a polyatomic molecule*, Phys. Rev. Lett., 073602, **108** (2012)

# Chapter 1

## Strong field processes in atoms and solids

The development of ultrashort sources of light over the last two decades which last only few femtoseconds ( $10^{-15}s$ ) in time and can have an average power of  $10^{12}W/cm^2$  have enabled scientists to study electronic processes where the Coloumb forces binding the electrons with their ionic core both in atoms and solids can be easily defeated by the field strength of laser fields. A plethora of interesting electronic phenomena follow interaction of atoms/solids with strong electric fields. Electrons which serve as a marker for electronic structure of matter as well as a glue holding the microcosm have long been studied by photo-ionization techniques following the photoelectric effect, this gives first hand information on the energy of electrons in matter and therewith that of their position in the quantum hierarchy in matter. Strong electric fields of ultrashort laser pulses open up several ionization pathways for electrons which have individual physical signatures thereby assisting in the pursuit of investigating matter. Interaction of atoms with ultrashort laser pulses has served as a tool to generate high harmonics of the fundamental frequency extending to keV in energy and is a key to generate isolated attosecond pulses. Nonlinearity induced by strong laser pulses gives a unique way of steering electrons inside matter which is not possible otherwise. This steering of electrons inside atoms has served as one of the benchmarks of human endeavour to coherent controlling of matter. Theoretical description of strong field processes in atoms is well established whereas for solids the understanding of strong-field process has been limited mainly because of lack of experiments. Recent experiments in solids have indeed triggered theoretical efforts in this direction as well. In this chapter we review strong field processes in atoms and solids starting from fundamentals of light matter interaction, theoretical description of strong field processes and coherent processes in semiconductors and dielectrics.

## 1.1 Light matter interaction: Fundamentals

Light matter interaction can be generally studied in the context of scattering arising from interaction of an electromagnetic field with a charged particle. For the purpose of illustration only, matter can be modelled as an ensemble of harmonic oscillators where one end of the spring is fixed to atomic core and the other is attached to an electron. An electric field of the form  $E = E_0 \cos(\omega t)$  will have an electromagnetic interaction with the charged particle given by  $F = qE$  which accelerates the charged particles. As a result of this acceleration, charged particles can absorb or emit radiation. Equation of motion for the charged particle can be written as;

$$m \frac{d^2 x}{dt^2} = qE_0 \cos(\omega t) - Kx \quad (1.1)$$

where the first and second terms on right hand side are Lorentz force from the electric field and restoring force from the atomic core respectively. The displacement of charged particle follows simply;

$$x(t) = \frac{q/m}{\omega_0^2 - \omega^2} E_0 \cos(\omega t). \quad (1.2)$$

Following the above simple formulation, bound charges are forced to oscillate at the same frequency as the incident field and the amplitude and phase of this oscillation depends on electro-magnetic field.

Linear interaction of light with matter in everyday life induces a linear polarization which serve as local antenna (inside matter) and thereby emitting almost instantaneously the light of same frequency as was incident on it. When the intensity of incident light is strong enough to generate an antenna with nonlinear response, the induced antenna inside matter generates frequencies higher (different) which are originally not present in the incident light. This nonlinear regime of interaction of electromagnetic field with matter can be bifurcated into two different regimes; one where the induced nonlinear response can be modelled with some definiteness i.e. perturbative regime and where the response is not *a priori* known i.e. nonperturbative regime and doesnot follow any definite nonlinear scaling with field strength of incident electromagnetic field.

Polarization induced in matter on linear interaction with light is given as;

$$P(t) = \epsilon_0 \chi_1 E(t) \quad (1.3)$$

where  $\epsilon_0$  and  $\chi_1$  are permittivity of free space and linear susceptibility of matter. Nonlinear perturbative interaction of matter with light makes  $P(t)$  follow different scaling (higher order) with respect to electric field instead of a just linear dependence of field as;

$$P(t) = \epsilon_0 [\chi_1 E(t) + \chi_2 E(t)^2 + \chi_3 E(t)^3 + \chi_4 E(t)^4 + \chi_5 E(t)^5 + \dots] \quad (1.4)$$

The above mathematical expression for treating perturbative nonlinear interaction comprises an approximation where the dominant contribution to induced polarization is still

linear and all higher order responses are added to model the system. When the intensity of light fields become stronger than  $10^{13}W/cm^2$ , the light-field induced polarization cannot be expressed as in equation 1.4 but more meticulous modelling has to be performed. Microscopic description of such processes at high intensities of driving fields can be performed with a complete quantum mechanical approach. In the semiclassical treatment of this problem, we treat the matter quantum mechanically and the light fields as being purely classical, the Hamiltonian of the system in this case assuming only dipole interaction between charges in matter and light field is given as;

$$H = H_0 - \mu \cdot E \quad (1.5)$$

and evolution of the wavefunction with such a Hamiltonian is described by the time dependent Schroedinger equation (TDSE);

$$i\hbar \frac{\partial \Psi}{\partial t} = H\Psi. \quad (1.6)$$

The above equation describes all dynamic properties of the system in presence of laser fields with only insurmountable challenge being its computation. The above equation can be simplified if the quantum system is modelled with only few states and the wavefunction be reduced to a matrix formulation of TDSE resulting into optical Bloch equations, this formulation is heavily used in studying quantum coherences and will be discussed in chapter 7 of this thesis.

## 1.2 Keldysh Parameter: Tunnel and Multi-photon ionization

L.V. Keldysh in his seminal paper in 1965[28] provided a unified formulation for different regimes of ionization pathways which depend on ionization potential ( $I_p$ ) in case of atoms and Band gap ( $E_g$ ) in case of solids and the intensity of the driving laser fields.

Ionization in case of atoms imply electrons being removed from their bound states in the Coulomb potential of the ionic core to a far lying continuum state. In case of solids it implies transition of electrons from their valence bands to the conduction band. Ultrashort intense laser pulses with high photon flux ( $\sim 10^{15}$  per shot) can force the atoms or solids to absorb several photons with their energy equal to the frequency of driving field in a ladder like situation as shown in Figure1.1 and reach the continuum (in atoms) or the conduction band (in solids) thereby ionizing from the parent ionic core. Electrons in this case go through several virtual states with their life time being equal to  $\sim$  ns much slower than the duration of laser pulses  $\sim$  fs hence allowing absorption of several photons. Tunnel ionization on the other hand is a field effect, where the Coulomb potential binding the electron with the ionic core is bent by the field of the laser pulses and the initially bound electronic wavefunction can tunnel out and go to the continuum. The selection of either of these two ionization pathways is governed by the Keldysh parameter,  $\gamma$ , which is described

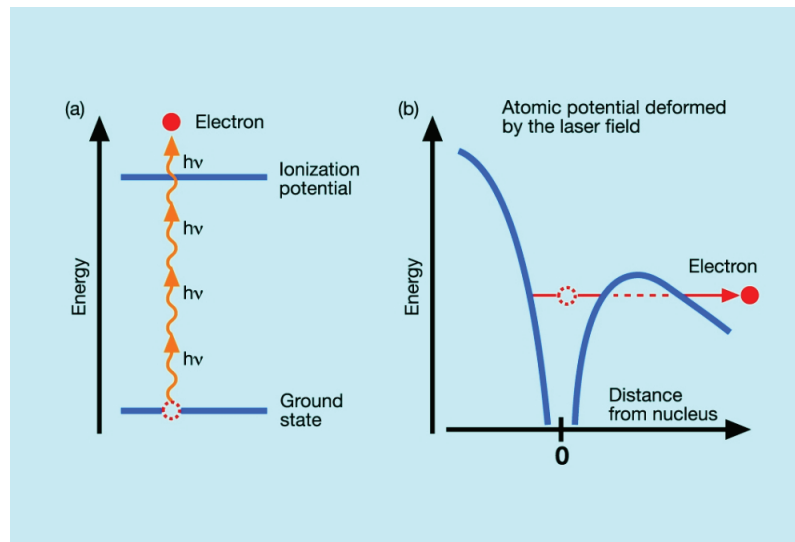


Figure 1.1: Ionization of atoms: transition of electrons from their bound states to continuum in presence of ultrashort laser pulses can occur either by a **a**, multiphoton absorption process or by **b**, tunnel ionization. This figure is adapted from <http://wof-cluster.desy.de/>.

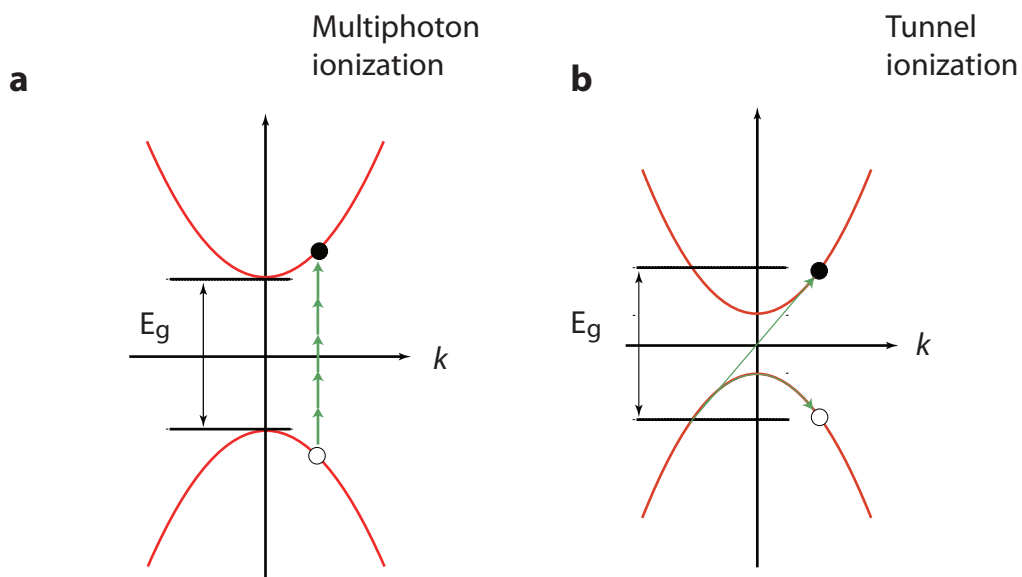


Figure 1.2: Ionization of semiconductors: transition of electrons from valence to the conduction band in presence of ultrashort laser pulses can occur either by a **a**, multiphoton absorption process or by **b**, tunnel ionization, tunnel ionization of electrons in solids is also known as Zener tunnelling. Electrons are represented with black circles whereas holes with white circles. This figure is adapted from Tamaya *et al.* [29].

as the ratio between tunnelling time of electrons through the Coloumbic barrier and the laser period. For atoms, Keldysh parameter is defined as:

$$\gamma = \frac{\omega_L \sqrt{2m_e I_p}}{eE_0} = \sqrt{\frac{I_p}{2U_p}} \quad (1.7)$$

where laser electric field is defined as  $E(t) = E_0 \cos(\omega_L t)$ ,  $m_e$  is the mass of electron and  $e$  is the electronic charge. Equivalently,  $\gamma$  can also be defined as the square root of the ratio between cycle averaged ponderomotive energy,  $U_p$  and ionization potential of the atom. When the applied field strength from laser pulses is much smaller than the Coloumbic field strength, the tunnelling time for the electrons is much longer and  $\gamma \gg 1$ , implying multiphoton process being the dominant ionization pathway. Conversely, when the applied field strength is stronger than the Coloumbic strength the tunnelling time is faster than the laser period which makes  $\gamma \ll 1$  making tunnelling as the dominant ionization pathway.

In case of solids (smmiconductors and dielectrics),  $\gamma$  is defined as,  $\gamma = \omega \sqrt{\frac{m^* E_g}{eE}}$ ,  $E_g$  is the bandgap of solid and  $m^*$  is the electron-hole reduced mass, switch in the regimes from multiphoton to tunnelling in case of solids follows the same thumb rule as in case of gas,  $\gamma \gg 1$  is multiphoton regime whereas  $\gamma \ll 1$  is tunnelling regime.

## 1.3 Attosecond Science

Observation of high harmonics(HH) on interaction of intense laser-pulse with noble gases in 1991 has revolutionized the field of non-linear optics. The spectra of HH were shown to follow a cut-off law which was linearity dependent on intensity, with an offset of the ionization potential of the noble gas,  $E_{cutoff} = I_p + 3.2U_p$ . HHG in gases was explainable by a simple semiclassical model which involved i) tunnelling of the initially bound electrons by the laser field followed by their ii) acceleration in presence of the driving laser pulses and eventually their iii) recombination with the atomic core [19]. Quantum mechanically HHG can also be elucidated by interference of a wavepacket which is split by the laser electric field taking an excited wavepacket  $\Psi_e$  with it and leaving behind the ground state wavepacket  $\Psi_g$ , this split of the wavepacket in presence of oscillating electric field generates an oscillating dipole ( $\Psi_g + \Psi_e$ ) which thereby leads to burst of HH[30]. This generation of HH bursts happen in every half-cycle of the multi-cycle driving laser pulses, interference of the dipoles from all the half-cycles leads to structured HH spectrum.

Availability of shorter driving laser pulses which consisted of only few-cycles of their carrier frequency led to a super-continuum generation in the HH spectra in the EUV to soft X-ray spectral regime and sowed confidence in utilizing this super-continuum spectra to generate even shorter pulses by utilizing this bandwidth rather than the driving laser pulse in the soft-X ray domain. Simultaneous to this availability of short driver pulses was the need to develop techniques to characterise these short pulses in the soft-Xray spectral domain. Concept of attosecond streak camera was introduced and experimentally demonstrated few years later[25][31][9]. Several innovations including spectral filtering of

the HH spectra by metallic foils, development of optics for reflection of EUV pulses and phase stabilization of laser pulses eventually led to generation of first isolated attosecond pulses in 2001 which were characterized by the techniques of streak camera[9].

Two distinct trajectories of electrons may exist in HHG process depending on the moment of their tunnel ionization and recombination with atomic core. Electrons ionized earlier and having a longer excursion in the laser fields are known as having long trajectories whereas electrons tunnel ionized later in time and having short excursion in the half-cycle of the laser field are known as having short trajectories. These two different types of electron trajectories exhibit distinct temporal features, EUV burst arising from short trajectory dominated emission is positively chirped whereas EUV burst coming from long trajectory dominated emission is negatively chirped. Macroscopic phase matching criterion dictates which of the two trajectories will dominate the emission of EUV bursts, gas targets when placed few millimetres after the focus of the driving laser are shown to be dominated by short trajectories[32], implying the EUV emission to be positively chirped. Metallic filters are known to exhibit negative dispersion at their transmission edges, this property has been extensively used to compensate for the positive chirp in the HHG process and EUV pulses with duration  $\sim 80$  as have been generated[26] and routinely used in the labs to study fundamental electronic processes.

Multi-cycle driver pulses on the other hand produce EUV bursts from their consecutive half-cycles hence generating a pulse train with individual bursts lasting close to  $\sim 650$  as[33], they are usually called attosecond pulse trains (APTs). Attosecond streak camera as mentioned in the above paragraph to characterize isolated attosecond pulses doesn't work in the case of train of attosecond bursts and a new methodology had to be put in place to characterize trains of attosecond bursts. A way to characterize APT is given the name of sideband oscillations. Sidebands in the discrete photoelectron spectra of EUV bursts are generated by weak driving pulses, which undergoes periodic modulation on variation of delay between the APTs and driving laser pulse, this technique is known as reconstruction of attosecond beating by interference of two photon transitions (RABBIT)[33].

Generation of EUV pulses as in the three step semiclassical model depends heavily on the very low recombination probability of tunnel ionized electrons with the atomic core owing to the small cross-sections of the atomic cores, this low probability manifests itself by low conversion efficiency ( $< 10^{-6}$ ) of HHG process. Pump-probe techniques in the conventional way have always required triggering and probing of ultrafast processes by a pair of identical pulses which is unfortunately not possible with attosecond pulses. So, attosecond pulses can only be used either as a pump or probe for the electronic processes which are triggered/probed by a different pulse. Numerous experiments using attosecond EUV pulses have been performed studying many electronic processes both in atomic and condensed phases.

## 1.4 Ultrashort laser-pulse interaction in dielectrics

Electrons can be set into a linear motion on application of a static voltage across any bulk solid, this linear motion of electrons is unfortunately not coherent due to very large scattering rates ( $\sim 10^{15}/s$ ) with the lattice of solids and other electrons forcing electrons to lose their phase coherence. After the pioneering work of Esaki and Tsu in 1980 producing semiconductors with alternating layers of high and small band gaps also known as semiconductor superlattices, the scattering rate of electrons can be dramatically reduced and electrons embark on a coherent (quantum) motion inside solids. Electrons inside superlattices with a bias of a static voltage perform oscillatory motion both in real and reciprocal space, as given by the acceleration theorem;

$$\hbar \frac{dk}{dt} = -eE \quad (1.8)$$

Considering a periodic one dimensional band structure with  $E_c(k) = 1 - \cos(kd)$ , the group velocity of electrons in real space is given by derivative of  $E_c(k)$  with respect to  $k$ ,  $v_g = \frac{\partial E_c(k)}{\partial k} \propto \sin(kd)$ , this sinusoidal behaviour of group velocity of electrons results into an oscillatory motion of electrons in a single band of superlattice with a frequency given by  $\omega_B = eEd/\hbar$ , it is also known as the Bloch frequency. Electrons are not quasiparticles but have a definite distribution both in real and reciprocal space,  $f(k, t)$  which forms a link between experimentally measured quantities and the quantum nature of electrons. The motion of this distribution of electrons under presence of a static electric field is given by;

$$\frac{\partial}{\partial t} f(k, t) = -\frac{e}{\hbar} E(t) \frac{\partial}{\partial k} f(k, t) - \frac{f(k, t)}{\tau} \quad (1.9)$$

where  $\tau$  is inserted to account for loss of coherence introduced in the electron wavepacket from scattering with lattice. Acceleration of electrons in superlattices by static electric fields leads to emission of terahertz radiation, whose frequency is identical to the Bloch frequency and depends on the strength of the applied electric field. Superlattices can be fabricated in such a way that it forms minibands of electronic levels, electrons when artificially injected (pumped by a Thz pulse) in any of these levels will undergo cascaded transition among the minibands which are separated by identical energies leading to a cascaded emission of terahertz pulses; amplification of Thz emission can be eventually obtained; this notion is extensively used to produce commercially tunable laser sources and are known as Quantum cascade lasers.

Electrons in presence of low field strengths move linearly around the minima of parabolic profile of conduction band with their velocity being proportional to the field strength, which is generally known as Ohm's law. Classical motion of electrons does not quite follow electric field lines as they continuously scatter from the lattice inside the solid. Quantum nature of electron transport in semiconductor sets in only when the field strength is strong enough to move the electrons away from the inflection point of the conduction band, the effective mass of electrons around the maxima of the conduction band is negative forcing electrons to move against the direction of applied field hence causing an oscillatory motion i.e. Bloch

oscillations. This oscillatory motion of the electrons competes with another quantum effect i.e. tunnelling where electrons around the maxima of a conduction band can tunnel to the next band, following linearly the field. This tunnelling effect of electrons between the bands at high field strength is known as Zener tunnelling. Electrons when follow the field lines of electric field are known to have *Ballistic* transport which is possible by having lower number of scattering events by reducing the impurity in a sample or using a superlattice in contrast to a *drift* transport which occurs in presence of many scattering events.

In presence of a static electric field coherent quantum motion of electrons in semiconductors is not possible owing to the presence of very high scattering rates which can be defeated by steering the electrons not with static voltage but by ultrashort laser pulses significantly faster than the scattering time. Interaction of bulk dielectrics with ultrashort laser pulses first leads to creation of electron hole pair either by multiphoton ionization or the tunnel ionization. The generated electron-hole pairs follow electric field and perform periodic motion in the conduction and valence bands respectively which is commonly known as dynamical Bloch oscillations in the literature. Motion of electron-hole pairs in the electronic bands of semiconductors/dielectrics open a plethora of interesting phenomena which are described in detail in chapters 3, 4 and 5 of this thesis.

Interaction of a model dielectric with two electronic bands with laser pulses can be emulated by an ensemble of two level atomic like systems at all the reciprocal space  $k$ -points. The atomic-like two level systems at different  $k$ -points are cross-coupled to each other by electronic correlations arising from Coulombic interaction (or other types of correlation) between electron-hole pairs. This dipole coupled interaction of electrons and holes can be meticulously modelled by semiconductor Bloch equations (SBEs), which is heavily used in the work presented in this thesis. Both perturbative and non-perturbative light-matter interactions in dielectrics are captured by SBEs with a single effective electron moving in presence of an effective potential being created by the rest of the electrons and lattice.

Driving electrons in atoms or solids by ultrashort laser pulses give rise to a microscopic current, controlling amplitude and frequency of this current opens up the avenue for electronics being operated by laser pulses at their frequency in close analogy with microwave electronics which relies on synthesis and use of fields at microwave frequencies. Conventional microwave electronics requires motion of electrons in the conduction band for performing logic operations with diodes and transistors by amplifying or reducing an electronic current. Interaction of dielectrics with laser pulses generate carriers (electrons and holes) which can undergo both vertical transitions among the bands as well as lateral transport along the bands which is required for electronics. In this thesis we present lateral motion of electrons along the conduction band of  $SiO_2$  leading to electronic currents with frequency as high as 8 PHz, and have also extracted properties of electrons at such high frequency such as its conductivity and current density. Further work is required to demonstrate operation of electronics with light waves but fundamental steps towards achieving it have already been taken which is indeed the capability to coherently drive electrons at frequencies as high as 8 PHz in the conduction bands of a dielectric material.

# Chapter 2

## Experimental setup: Laser-system and light field synthesis

In this chapter, laser-system and the experimental set-up used to perform experiments reported in this thesis are briefly discussed. Also the principles of light field synthesis and its implementation in a day to day work in the lab are presented.

### 2.1 Laser-system

All experiments presented in this thesis were performed at AS1 beamline at MPQ. The front end of the beamline is a commercial laser system from Femtolasers GmbH producing laser pulses of 1 mJ energy at 3 kHz repetition rate with the central wavelength of the pulses at 800nm, the pulse duration being  $\sim 23$  fs. The laser system consists of a Kerr-Lens mode locked oscillator [34] producing  $\sim 6$  fs pulses at a repetition rate of 78 MHz with 3-4 nJ energy. The pulses coming out of the oscillator are seeded into a multi-pass amplifier to boost the energy of the pulses from 3-4 nJ to nearly 1 mJ. The laser pulses are first stretched in time by letting them propagate through a thick glass slab resulting into pulses with duration  $\sim 25$  ps. These pulses are then amplified by a Ti:sapphire pumped crystal by letting the pulses go through it 4 times in a crossed-beam set-up as shown in Figure 2.1 before the pulse is picked up to be sent to a Pockel cell to reduce the repetition rate from 78 MHz to 3 kHz. Inside the Pockel cell an ultrahigh voltage of  $\sim 6.4$  kV is applied to an electro-optic crystal (in our case, Potassium di-deuterium phosphate, KDP) for a time period as short as 3-4 ns, effectively the Pockel's effect is experienced by a single pulse in the whole pulse train coming at 78 MHz repetition rate. After passing through the Pockel cell only a single pulse in the whole pulse train will have its polarization switched from  $s$  to  $p$ . The pulse with the switched polarization compared to the rest of the pulses in the train is then further amplified inside the amplifier 5 more times in the crossed-beam set-up and rest of the pulses in the pulse train are dumped, this reduces the repetition rate from 78 MHz to only 3 kHz. Laser pulses on every pass through the Ti:sapphire crystal will have their bandwidth reduced due to the gain narrowing effect which is detrimental

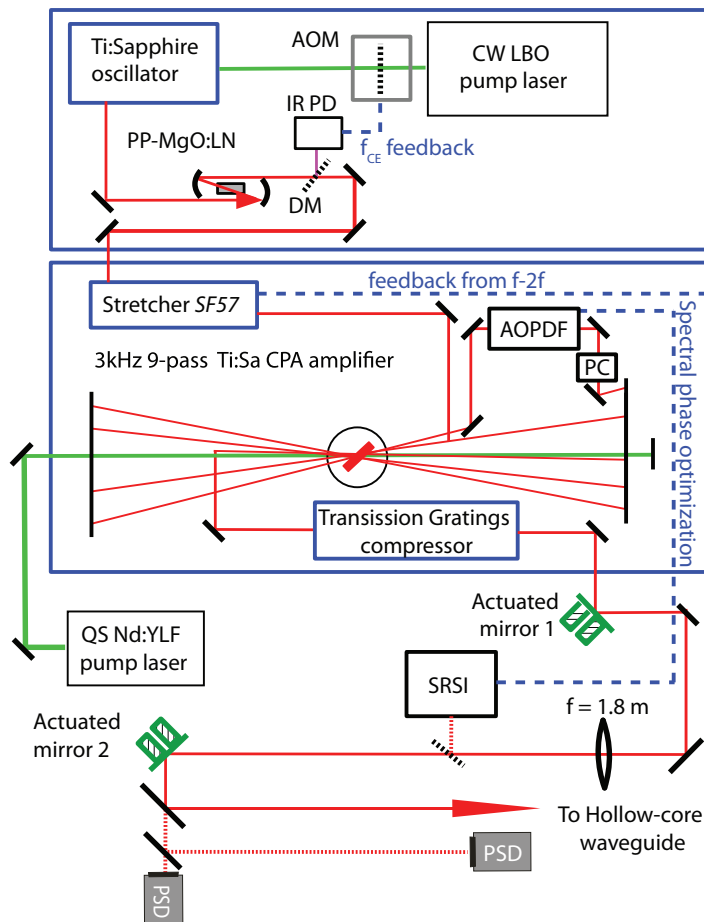


Figure 2.1: Schematic of the laser system used for experiments presented in this thesis. 6 fs, 3-4 nJ energy pulses at a repetition rate of 78 MHz from a Kerr lens mode-locked oscillator are seeded into a multipass amplifier where the repetition rate is reduced from 78 MHz to 3 kHz by a Pockel cell and the energy of the pulses is amplified from 3-4 nJ to 1 mJ, the pulse duration after compression from the transmission grating compressor is  $\sim 23$  fs. An AOPDF is hosted inside the amplifier to overcome the gain narrowing effect in the spectral bandwidth of pulses during amplification. The laser pulses from the amplifier are seeded into an hollow core fibre (HCF) filled with Ne gas, the beam being seeded to HCF is position locked by a feedback system with two mirrors being mounted on actuators. Stabilization of the carrier envelope phase is accomplished by a  $f$ - $\theta$  self-referencing technique with DFG taking place inside a periodically poled lithium niobate crystal (PPLN), the pump power of CW LBO pump laser is modulated by an AOM for CEP stabilization.

to the pulse duration which can be achieved. To overcome this shortcoming an Acousto Optic Programmable Dispersive Filter (AOPDF) is used just after the pulses come out

of the Pockel cell. An AOPDF consists of a birefringent crystal with a radio frequency generator on top of it generating acoustic waves inside the crystal. Interaction of laser pulses with acoustic waves diffracts them with the diffraction efficiency being a function of the wavelength of the laser pulse, this property can be used to generate spectral hole in the bandwidth of laser pulses. A spectral hole in the centre of the bandwidth of laser pulses is helpful to overcome the gain narrowing effect. AOPDF is also useful to tune the spectral phase of the laser pulses, helping to avoid high-order distortions in it and produce spectrally clean laser pulses. After the completion of 9 passes inside the amplifier, the laser pulses are compressed by a transmission grating compressor finally producing laser pulses with a bandwidth of  $\sim 60$  nm with a pulse duration of 23 fs and 1 mJ energy at a repetition rate of 3 kHz.

The bandwidth of laser pulses from the laser system can be further broadened by letting the pulses propagate through a hollow core-fibre filled with Neon gas. Third order non-linear process of self-phase-modulation adds higher and lower frequency components to the original band width of the laser pulse. An ultrashort pulse of light, when travelling in a medium induces a time varying refractive index of the medium due to the optical Kerr effect. For an ultrashort pulse the intensity profile can be given by;

$$I(t) = I_0 \exp\left(-\frac{t^2}{\tau^2}\right). \quad (2.1)$$

Time varying refractive index  $\eta(t)$  on interaction of laser pulse with matter is given as;

$$\eta(t) = \eta_0 + \eta_2 I(t) \quad (2.2)$$

this time variation of refractive index produces an instantaneous phase shift of the pulse;

$$\phi(t) = \omega_0 t - \frac{2\pi}{\lambda_0} \eta(t) L, \quad (2.3)$$

and the instantaneous frequency is then given by,

$$\omega(t) = \frac{d\phi(t)}{dt} = \omega_0 - \frac{2\pi L}{\lambda_0} \frac{d\eta(t)}{dt} \quad (2.4)$$

The instantaneous frequency will shift to redder frequencies in leading edge of the pulse as the slope of  $I(t)$  Vs.  $t$  is positive whereas in the trailing edge of the pulse the instantaneous frequency shifts to bluer frequencies due to negative slope of  $I(t)$  Vs.  $t$ . Unfortunately, this self phase modulation process produces broadband pulses which are positively chirped and has to be compensated later on. Laser pulses from the amplifier are focused by a 1.8 m long focal length biconvex lens in front of a 1.1 m long hollow core fibre which is filled with Neon gas, this leads to generation of more than two and half octave spectral bandwidth starting from 230 nm to 1000 nm.

### 2.1.1 Carrier envelope phase stabilization

Absolute phase of the carrier wave under the envelope of an ultrashort pulse is an important parameter governing light-matter interaction for pulses with duration of only few femtoseconds ( $\sim 5fs$ ) consisting of only 2-3 wave-cycles at the central wavelength of 800 nm. In very basic terms, an offset in the carrier envelope phase arises due to difference in the group and phase velocity of laser pulses inside the cavity.

$$\Delta\phi_{CEP} = \frac{2\pi l_c}{\lambda} \left( \frac{1}{v_g} - \frac{1}{v_p} \right) \quad (2.5)$$

where  $v_p$  and  $v_g$  are phase and group velocity respectively of pulse inside the cavity which has a length of  $l_c$ . A  $\Delta\phi_{CEP}$  is the measure of offset in the maxima of the carrier wave and envelope.

The concept of CEP can be understood both in the time and the frequency domain [35]. An ultrashort laser pulse from an oscillator has an underlying frequency comb with comb lines made of longitudinal modes coming from a model-locked laser, the separation between these comb lines is the repetition rate of the laser. Although ultrashort pulses from oscillator are obtained by locking the phases of lasing longitudinal modes, the CEP of such pulses in principle should be fixed but thermal and mechanical drifts in the cavity force the frequency comb to drift slightly from one pulse to the other. The small drift  $\delta$  in the comb line results into a CEP shift of  $\Delta\phi_{CEP} = 2\pi \frac{\delta}{f_r}$ , where  $f_r$  is the repetition rate of the laser. Thus stabilizing  $\delta$  gives the control over  $\Delta\phi_{CEP}$ , if  $\delta$  is set as a  $r^{th}$  fraction of  $f_r$  i.e.  $\Delta\phi_{CEP}$  varies as  $\frac{2\pi}{r}$  from one pulse to the other, then every  $r^{th}$  pulse will have the same  $\Delta\phi_{CEP}$ . A pictorial depiction of concept of CEP in the time and frequency domain is shown in Figure 2.2. Stabilization of offset in the successive frequency combs  $\delta$  requires capability to measure it in the first step, this can be accomplished by a self-referencing technique. The laser pulses are made to undergo a difference frequency generation (DFG) process, which implies generation of a difference frequency (DF) comb from a fundamental comb. A DF comb will have comb lines with frequency of  $(m - n)f_r$ ,  $(m - n + 1)f_r$ ,  $(m - n + 2)f_r$  and so on, a DF comb will be free of the offset  $\delta$  and will be exclusively CEP stable. An interference between DF comb and fundamental comb will produce frequency of the offset i.e.  $\delta$ . The frequency  $\delta$  is much smaller than the repetition rate of the laser and is thus easily separable in the interference process by a low-pass frequency filter, in this case we use a Radio-frequency filter. The interference signal after low-pass filtering is detected by an avalanche photodiode and converted into frequency domain electronically. Once  $\delta$  is measured, it is brought closer to  $\frac{f_r}{4}$  by adjusting the dispersion inside the cavity, varying dispersion in the cavity changes the group velocity  $v_g$  which in turn changes  $\Delta\phi_{CEP}$  hence also changing  $\delta$ . Locking of  $\delta$  at a fixed value is achieved by an electronic feedback system where both  $\delta$  and  $f_r$  are continuously monitored and small drift in  $\delta$  is given as feedback to an acoustic optic modulator (AOM) which modulates the incident pump power on the crystal of the oscillator, modulation of the pump power changes the spectral phase introduced in the pulse by the Kerr effect. Variation of the spectral phase by the AOM changes the instantaneous frequency of the comb thereby stabilising it at the desired

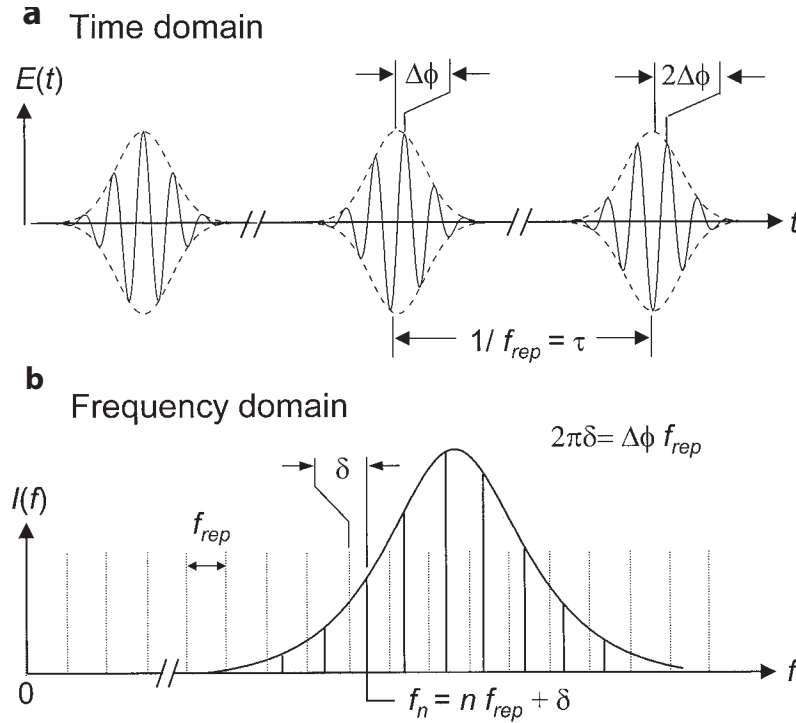


Figure 2.2: Relation of carrier envelope phase in the time and frequency domain. **a**, In the time domain laser pulses will have an offset between the maxima of their carrier wave (solid curve) and the envelope (dashed curve), every consecutive pulse from the laser will have an offset of  $\Delta\phi$ . **b**, In the frequency domain, every ultrashort laser pulse has an underlying frequency comb whose comb lines are the longitudinal modes of the mode-locked oscillator with a spacing of the repetition rate of the oscillator and all the lines are integral multiple of it i.e  $m f_r$ . External perturbation on the laser will have the frequency comb drifting, where all the comb lines drift by  $\delta$  ( $n f_r + \delta$ ) every consecutive laser pulse. Correspondence between  $\delta$  and  $\Delta\phi$  is given by  $\Delta\phi = 2\pi \frac{\delta}{f_r}$ , CEP stabilization works in the frequency domain where the first step is to measure  $\delta$  by a self-referencing technique and later locking it at a fixed value of  $r^{th}$  fraction of the  $f_r$  such that every  $r^{th}$  pulse from the laser will have the same CEP. This figure is adapted from Jones *et al.*(2000) [35].

position.

In our laser-system every 4th pulse coming from the oscillator is CEP stabilised and it is this pulse which is picked up by the Pockel cell for further amplification inside the amplifier. Laser pulses on their propagation through the amplifier and the hollow-core fibre accumulate small drifts in CEP which can be compensated by another feedback which is slower than the one working in the oscillator. This slow feedback works by a self-referencing technique where interference fringes between fundamental pulse and its second harmonic are detected and the feedback is given to the system which modulates the dispersion inside the amplifier to compensate for the slow drifts in  $\Delta\phi_{CEP}$ .

## 2.2 Light Field Synthesis

Producing manipulated microwave electric fields is an important milestone in electronics which requires availability of broadband microwave fields. Availability of ultra broadband coherent light source coming from the hollow core fibre provides a firm base for manipulation of electric fields at optical frequencies as well. Broadband light coming from the hollow core fibre is split by dichroic beam-splitters (DBS) and separated into four different spectral channels as shown in Figure 2.3, the mirrors in each individual channel compensate for the positive chirp accumulated during the SPM process inside the hollow core fibre. The pulses coming from individual channels are eventually combined by the same kind of DBS which initially separated them. Pulse durations of each channel is measured by a transient grating frequency resolved optical gating (TG-FROG) apparatus, intensity profiles of individual channels is shown in Figure 2.3. Two mirrors in each channel are placed on a piezoelectric stage to generate relative delay among them.

Spatial overlap of the beams from different spectral channels can be performed by imaging their near and far field beams profiles onto a CCD camera. Temporal overlap of the channels can be achieved by maximising a highly nonlinear process of high harmonic generation, channels can be moved relative to each other so as to maximise EUV counts by HHG on a EUV CCD camera. The bandwidth  $\Delta_L = 1.1 - 4.6eV$  of pulses in the synthesizer is sufficient to support pulses with duration as small as  $\sim 350$  as. These sharp optical transients unfortunately cannot be characterised by any FROG characterization techniques as FROG is only sensitive to the envelope of the pulses whereas for sub-cycle pulses, the precise information of field under the envelope is more important. Attosecond streaking which is a direct field characterization technique is used to characterize the pulses coming out of the synthesizer. Attosecond streaking is briefly discussed in the next sections. Contribution of field waveforms from all the spectral channels to the final electric field as retrieved by attosecond streaking can be obtained by performing a Fourier analysis. Synthesis of desired field profiles for the experiment can then be performed with known relative temporal movements of channels with respect to each other. The CEP of each individual channel is also controllable by inserting or removing glass from the beam path. This whole process as described above completes the cycle of light-field-synthesis. Lately, we have been able to generate pulses as short as  $\sim 400$  as, where only one half-cycle of the pulses has more than 50% of energy of the pulse. For such pulses the pulse duration is not defined by its envelope but rather by its field profile. Demonstration of field synthesis by adjustment of temporal phases of individual spectral channels retrieved from a measured streaking spectrogram is demonstrated in figure 2.5.

Thermal drifts resulting into slippage of relative temporal synchronization between the different channels can be compensated by both an active and a passive stabilization. Passive stabilization is achieved by maintaining a constant temperature on the monolithic piece of Aluminium on which all the optics are mounted. Active stabilization of the temporal slippage between the channels can be performed by feedback to the piezoelectric stages by monitoring spectral inference between the overlapping regions in adjacent spectral channels of the synthesizer. Even in the case of perfect temporal synchronization between

the channels its possible to observe spectral interference between adjacent channels as all the dispersive optics in the synthesizer are designed for  $p$  polarization which implies even though the  $p$  polarization of all the channels are temporally synchronized the tiny contribution of  $s$  polarization is still off-synchronous and can produce spectral interference between the adjacent channels. More details on the working principles of light field synthesizer can be found in references [36] and [37].

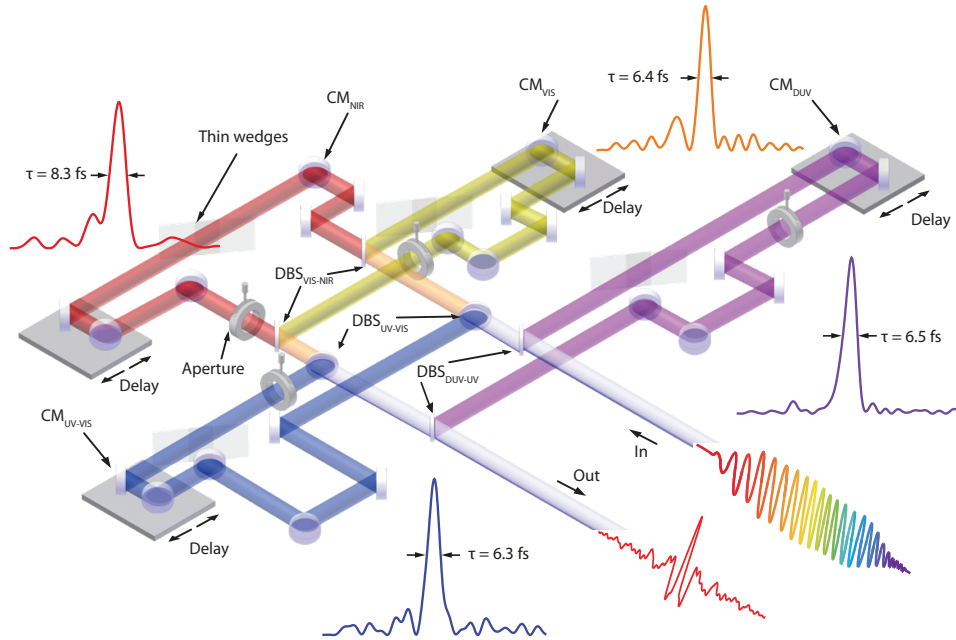


Figure 2.3: Light Field Synthesizer (LFS): Ultra-broadband light coming out of the hollow core fibre (see text) is split into different spectral channels by dichroic beam splitters (DBS), in the individual channels the pulses are spectrally tuned to compress them temporally, the intensity profiles of the pulses as measured by TG-FROG are displayed next to each channel. Relative delay between individual channels is generated by piezoelectric stages on which two mirrors of each channel are mounted. Pulses from all the spectral channels are combined in the end by same kind of DBS which initially split them, sub-cycle pulses from the synthesizer are eventually characterized by the technique of attosecond streaking.

## 2.3 Overview of experimental set-up at AS1 beamline

Here we briefly overview the experimental set-up at AS1 beamline at MPQ, further details of the beamline can be found in [38][39], the set-up is extremely versatile and can be used for different kinds of experiments. The experimental set-up consists of two main ultrahigh vacuum chambers with their pressure being maintained at  $1 \times 10^{-3}$  mbar and  $1 \times 10^{-6}$  mbar

respectively. Optical pulses from 2nd generation light field synthesizer are focused by a 32.5 cm focusing mirror onto a Ne gas target and the optical and generated EUV pulses are spatially separated by small metallic filters (Zr or Al) which are suspended by a pair of tungsten wire ( $\sim 30\mu\text{m}$  thickness). The beam profile of generated EUV pulses can be seen with a back illuminated yield calibrated EUV camera from Rooper Scientific, spectra of EUV pulses can also be recorded by replacing the mirror directing the beam to EUV camera by a 1200 grooves/mm flat field grating from Hitachi. EUV and optical pulses are focused under a time of flight mass (TOF) spectrometer by a dual mirror module where inner and the outer parts are made from a 12.5 cm concave mirror. The coating on the outer and inner cores are different; optimised for the spectral range of optical pulses and EUV spectral range respectively. Inner mirror reflecting the EUV pulses in the mirror module is placed on a Piezo stage where a delay as precise as 20 as can be generated between EUV and optical pulse. Temporal overlap between the two mirrors in the module can be found by linear interference of the optical beams for which the optical beams in the focus under TOF are imaged by an aberration corrected biconvex lens and the focal spot is magnified by  $\sim 4$  times. EUV and optical pulses are focused on a gas target filled with Ne/Ar placed under TOF. Once the optical field characterization is done by attosecond streaking, optical pulses can be used for various experiments like transient absorption or EUV generation with solids, EUV emission from solids is recorded either by a commercial EUV spectrometer from McPherson or a home-built spectrometer. Unwanted thermal or mechanical drifts between the mirrors in the mirror module can be controlled by observing optical interference of a He-Ne laser beam reflected-off from the surface of two mirrors and providing feedback to the Piezo hosting the inner mirror.

Concave mirror focusing the optical pulses on the HH gas target can be replaced by a longer focal length to generate EUV emission from  $\text{SiO}_2$  and the input intensity on the sample can be controlled by a motorised iris. A 3D stage hosting a gas nozzle and  $\text{SiO}_2$  sample was assembled to enable experiments with EUV emission from a noble gas or solid samples.

An ion detector (HH meter) which detects ions of residual gas between the two experimental chambers being ionized by EUV radiation from the first chamber is used to monitor stability of the generated EUV flux, it can also be used to bring closer individual channels temporally in the LFS as the ion yield will increase with better temporal overlap between the pulses. In case of low EUV flux from solids an external gas source of Xe can be used to amplify the signal in HH meter and help temporally overlap the channels from LFS.

## 2.4 Attosecond streaking: Complete characterization of optical pulses

Attosecond streaking is a cross-correlation technique between an optical driver pulse (from synthesizer) and an EUV pulse generated by HHG. Optical pulses from the synthesizer are focused on a Ne gas jet to generate EUV pulses by HHG process. The information of EUV

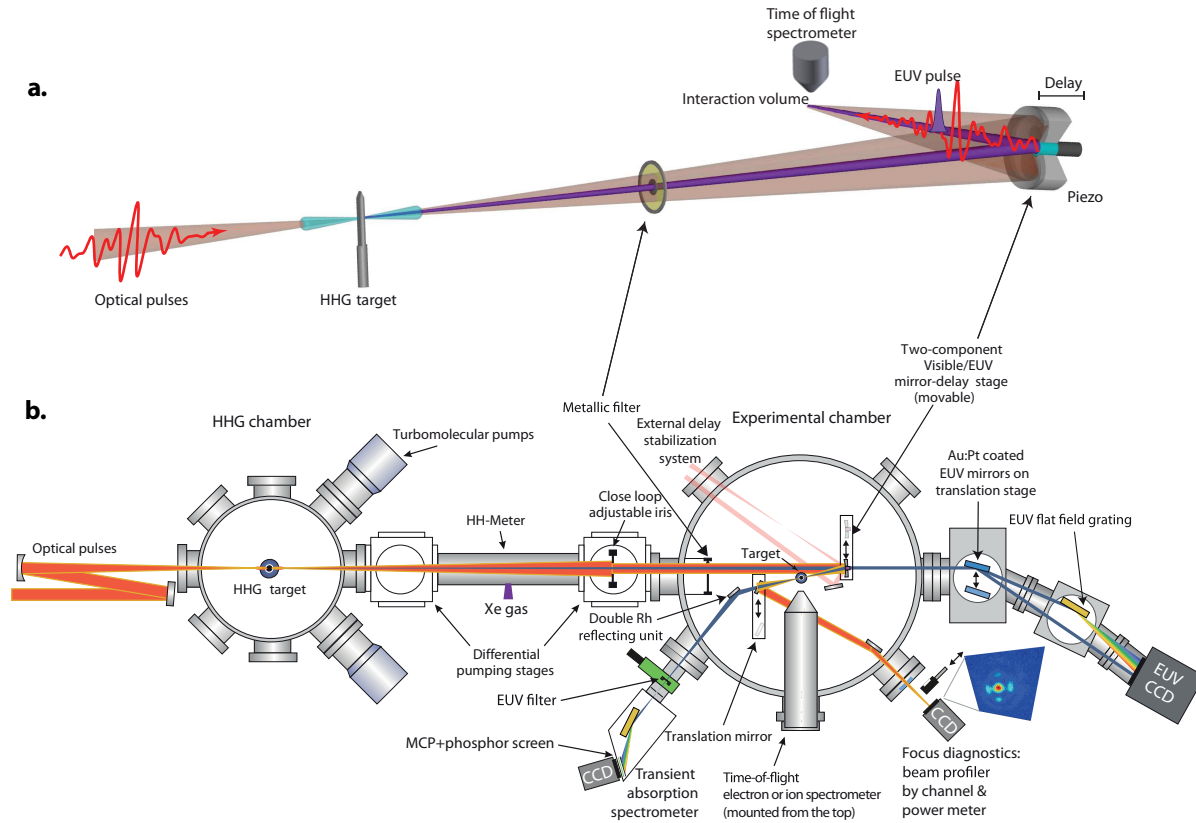


Figure 2.4: **Overview of set-up at AS1 beamline.** AS1 beamline hosts two separate chambers at an ultrahigh vacuum level, the first chamber is used to generate EUV emission and the second chamber is used to perform field characterisation of optical pulses via attosecond streaking and experiments. **a**, Schematic of attosecond streaking set-up; after EUV pulses are generated in HH target they are spatially separated from optical pulses by use of small metallic filters in the beam path, the pulses are delayed relatively by a piezo stage, electrons photoionised by EUV pulses are recorded in a time of flight mass spectrometer. **b**, A schematic of the experimental set-up with all major components, the set-up hosts two EUV spectrometers and an yield calibrated EUV camera. Diagnostic tools of the set-up are also displayed. The 3D set-up for AS1 beamline is adapted from [40].

pulse i.e. its spectral phase and envelope can be transferred by single photoionization to electrons, making them the replica of EUV pulse. The optical driving pulse from synthesizer acts as a phase gate on photoelectrons. Measurement of photoelectron spectra as a function of delay between the optical and EUV pulses results into a FROG like spectrogram which can be conveniently treated by reconstruction algorithms as will be discussed in detail in Chapter 4 of this thesis as well as in Appendix D.

Photoelectrons will be accelerated by optical field of laser as per the Newton's laws of

motion;

$$\ddot{x} = -\frac{eE_L(t)}{m_e}, \quad (2.6)$$

which after integration becomes,

$$\dot{x}(t) - \dot{x}(t_0) = -\frac{e}{m_e} \int_{t_0}^t E_L(t') dt' \quad (2.7)$$

$t_0$  is the time of ionization or the birth of photoelectrons, as photoelectrons are detected after sufficiently long time ( $\sim$  ns) compared to the laser pulse duration ( $\sim$  few fs), the final time can be considered infinitely separated from the moment of ionization  $t_0$ , thus the final velocity and change in momentum of electrons is,

$$\begin{aligned} v(\infty) &= v(t_0) - \frac{e}{m_e} A_L(t_0); \\ p(\infty) &= p(t_0) - eA_L(t_0); \\ \Delta p(\infty, t_0) &= -eA_L(t_0) \end{aligned} \quad (2.8)$$

where  $A_L(t_0)$  is the vector potential of the electric field. The final kinetic energy of electrons as detected is thus,

$$E_{KE}(\infty, t_0) = \frac{1}{2} m_e \left[ v(t_0)^2 - \frac{2e}{m_e} A_L(t_0) v(t_0) + \left( \frac{e}{m_e} \right)^2 A_L(t_0)^2 \right] \quad (2.9)$$

Ionization of atoms by optical pulses is prevented by keeping their intensity as low as  $10^{12} W/cm^2$  which results into simplification of the above equation where the term  $\left( \frac{e}{m_e} \right)^2 A_L(t_0)^2$  can be ignored compared to  $\frac{2e}{m_e} A_L(t_0) v(t_0)$ . The final change in the kinetic energy of the photoelectrons is thus simplified to,

$$\Delta E_{KE}(\infty, t_0) \approx -\frac{2e}{m_e} A_L(t_0) v(t_0) \quad (2.10)$$

The above analysis shows transparently that an attosecond streaking spectrogram is a direct measurement of vector potential of electric field, a simpler analysis without FROG reconstruction of spectrograms can be thus performed for rapid evaluation of spectrograms [36]. The swift evaluation of electric fields from spectrogram and their Fourier analysis helps on-line synthesis by adjustment of relative temporal phases of individual channels of LFS to generate electric field of choice in experiments.

Here we demonstrate applicability of the above analysis used in a routine day in the lab to generate ultrashort light transients. An attosecond streaking spectrogram measured with random phases of individual spectral channels in LFS is shown in Figure 2.5a, a Fourier analysis of the electric field retrieved from the spectrogram allows us to reconstruct relative temporal phases among the spectral channels of LFS (Figure 2.5c). Relative phases of the spectral channels in the LFS can be synchronised (Figure 2.5d) by appropriate feedback to LFS to produce an ultrashort pulse where the contrast between main and adjacent

half-cycles in the intensity profile is nearly 4.5 as shown in Figure 2.5f. Conventional definition of pulse duration for an ultrashort pulses is with respect to its envelope, but for pulses where one half-cycle dominates and carries more than 50 % of the pulse energy this definition is not reasonable, for such pulses pulse duration is defined as FWHM of the main half-cycle which comes around to be close to 400 as. As the central wavelength of these pulses is close to  $\sim 580$  nm, these pulses are now termed as optical attosecond pulses.

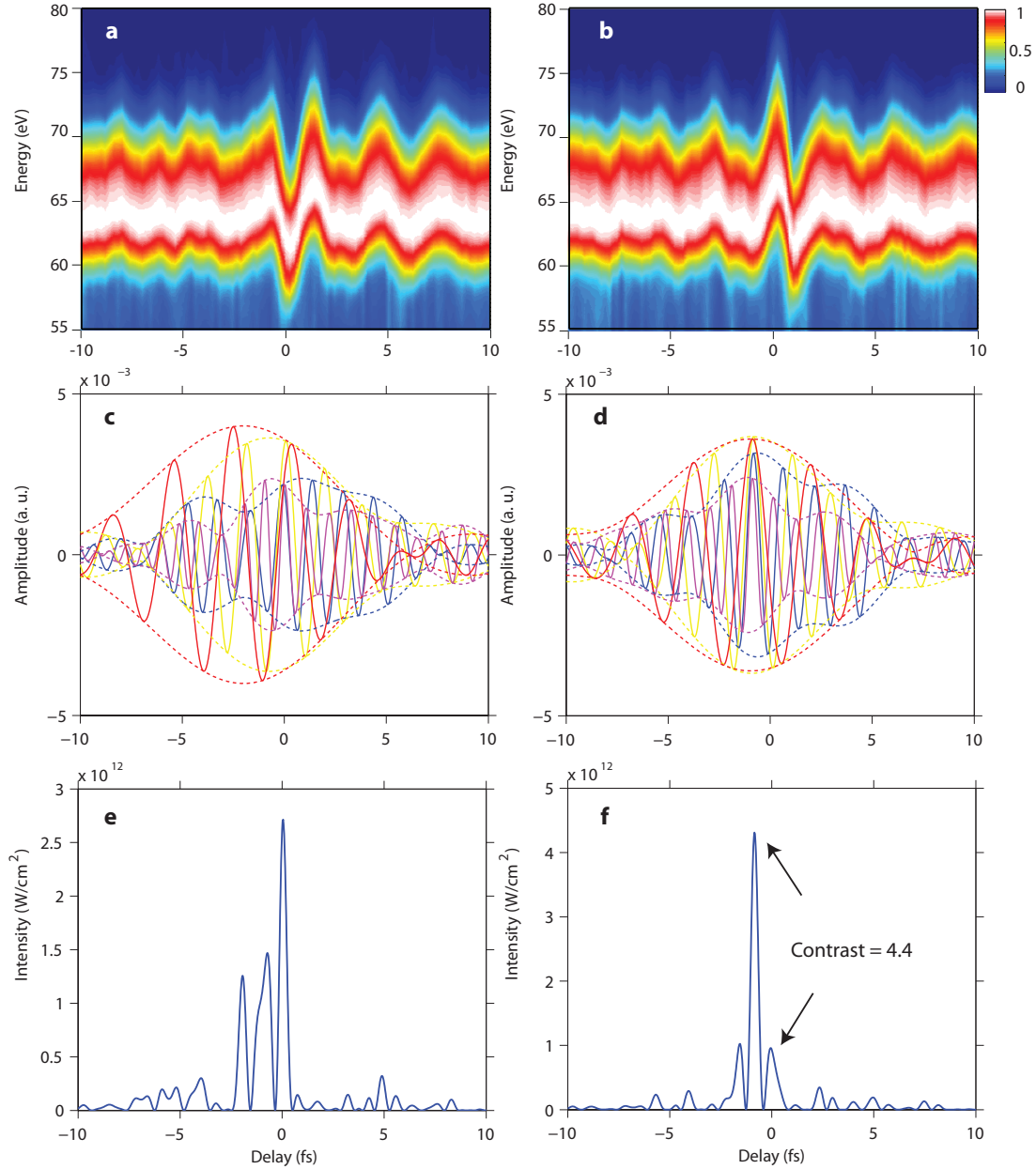


Figure 2.5: **a**, **b**, Measured attosecond streaking spectrograms with random and perfectly synchronised relative temporal phases between individual spectral channels in LFS respectively. **c**, **d**, Reconstructed temporal profiles of individual spectral channels in LFS as retrieved from measured spectrograms in **a** and **b** respectively. **e**, **f**, Reconstructed intensity profiles of electric fields retrieved from streaking spectrograms in **a** and **b** respectively.

# Chapter 3

## Coherent extreme ultraviolet radiation from bulk solids: Polarization spectroscopy of electronic bands

### 3.1 Introduction

Nonlinear interaction of light with matter has paved the way towards many modern microscopic [41] and spectroscopic techniques [42][30] to investigate matter on its fundamental space-time realms. Manifestation of high-harmonics [43][19] (HH) of the fundamental laser frequency is a generic response of matter to nonlinear interaction with laser pulses. Even though observation of non-perturbative HH emission from gases [44] and plasmas [45] has long been reported but none such experiments were possible with solids. Theoretical efforts in the past have predicted the observation of HH emission from Graphene [46] and GaSe [47], but it was not until 5 years ago when the first observation of non-perturbative HH emission in transmission through a solid was measured from ZnO [22]. HH emission was also reported recently from intense THz driving laser pulses interacting with GaSe [48]. HH spectra in the above two experiments extended till the UV region of the spectrum, lately we have been successful in extending the HH emission from a solid, in this case SiO<sub>2</sub> to extreme ultraviolet (EUV) domain of the spectrum [23]. The underlying mechanism for HH emission in solids is fundamentally different from gases owing to its high density and periodicity. The energy of the HH in case of gases comes from the driving field strength and the electron trajectories ensuing their generation through tunnel ionization being described abstractly via the three step model [19]. In case of solids, the HH emission can come either from the interband polarization being created by the driving laser pulse by dipole coupling between the electronic bands or the carriers can gain nonlinearity by moving in the dispersive energy landscape of bands i.e. by intraband currents. The debate to which one of mechanisms is the dominant one in HH from solids is still going

on [49][29][50][51]. Spectral domain measurements of HH emission from ZnO has earlier been attributed to intraband currents [22] but more recent time-resolved measurements [52] point to interband dominated dynamics alike to three step model in gases. Whereas THz HH emission in GaSe has been attributed to be arising from an interplay between inter and intraband mechanism [48]. Contrary to the above two mechanisms, HH EUV emission in SiO<sub>2</sub> which is much above its bandgap of  $\sim 9.4eV$  can be entirely modelled by the intraband contribution; but conformity with a time resolved measurement was still pending.

The collision and acceleration of electrons and holes is prevalent for HH emission in case of both gases and solids. In case of atoms and molecules, the re-collision of electron with the ionized core can probe the structure of matter [20][53] just as in collision physics where high energetic ions can probe the electronic structure of target under study. While in solids if the underlying mechanism of HH emission is intraband, the acceleration of electrons and holes over the energy landscape of bands can encompass the information leading to the reconstruction of their dispersion profiles [23]. The reconstruction of fine details in the dispersion profile of the first conduction band [23] of SiO<sub>2</sub> has been recently reported and it has sowed confidence in reconstructing complete tomographic structural information inside solids with purely polarization based spectroscopic techniques rather than with photoemission techniques [54]. Also, re-collision of electrons and holes in the interband dominated mechanism in ZnO has been employed recently to reconstruct the dispersion profiles of the bands [55].

Time-resolved measurements of HH emission in ZnO [52] and GaSe [56] have lead to new insights into re-collision of electron-hole based process and existence of non-perturbative quantum interferences in electronic transitions between the bands likely behind HH generation in solids. EUV spectral range is the most instrumental one in the field of attosecond science and performing temporal profile measurements of EUV fields from HH emission in SiO<sub>2</sub> hold great promise to the field of attosecond science. Unlike atoms, driving electrons inside a bulk solid like SiO<sub>2</sub> leads to currents of multi Peta Hertz (PHz) frequencies, capability to measure and hence control this current gives new opportunity towards realizing all solid-state based light-wave electronics [39]. Contemporary work on HH generation in solids has promised on possibility of developing all solid-state based attosecond sources [52][56]. Accomplishing such a solid-state based attosecond source holds an exemplary benefit to many areas of modern ultrafast science.

A major part of the results presented in this chapter have been the subject of a doctoral thesis [27], nevertheless we summarize briefly the previous results along with the new ones for furnishing a concrete stage for the work which will be presented in the next chapters.

## 3.2 Experiment

Illuminating ultrathin free-standing polycrystalline samples of SiO<sub>2</sub> (thickness  $\sim 120nm$ ) to intense field-sculpted optical waveforms gives rise to EUV radiation which were spectrally recorded in our experiments; the experimental set-up is presented in Figure 3.1a.

The optical waveforms used to generate EUV radiation were first synthesized in a 2<sup>nd</sup> generation light-field-synthesizer [37][57][36] and characterized by the technique of attosecond streaking [31][26] before being shone on the SiO<sub>2</sub> nanofilms. One such attosecond streaking spectrogram used to characterize the driving optical waveform is shown in Figure 3.1b. EUV spectra with discernible peaks corresponding to odd high-harmonics of driver energy of 1.5 cycle optical driver waveform were measured as depicted in Figure 3.1c; variation of spectral amplitude of the measured harmonics on a linear scale (plateau-like) in the cut-off region suggests as to a much less-nonlinear mechanism being in place behind EUV generation in SiO<sub>2</sub> compared to gases where the spectral amplitude variation in the cut-off region is typically on an exponential scale. EUV spectra were methodically investigated by increasing the intensity of a 1.5 cycle optical driver waveform by adjusting the aperture of a motorized iris along the beam path falling on the SiO<sub>2</sub> sample. At incident peak field strengths of more than 1.1V/Å the samples suffers from absorption induced damage which can be mitigated by driving the sample recursively along the direction lateral to the beam, at an speed commensurable to laser repetition rate. Linear scaling of the cut-off energy with respect to the driving field strength of the optical waveforms is observed experimentally which is in contrast to quadratic variation in gases.

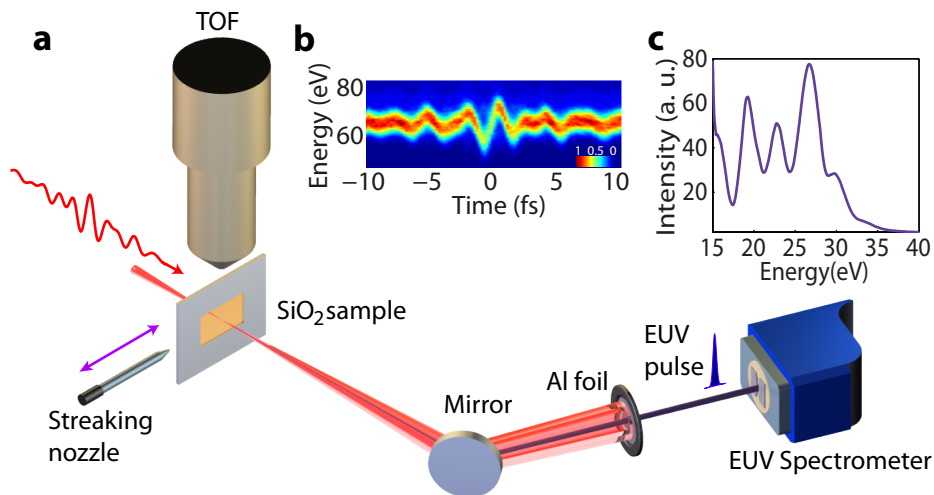


Figure 3.1: **a**, Experimental set-up used for measuring HH EUV emission from SiO<sub>2</sub> nanofilms (thickness  $\sim 120\text{nm}$ ). **b**, Attosecond streaking spectrogram recorded to retrieve the optical field waveform before being focused on SiO<sub>2</sub>. **c**, A typical EUV spectrum measured by a 1.5 cycle driving optical waveform.

Interaction of intense optical waveforms with wide bandgap dielectric material like SiO<sub>2</sub> creates electron-hole pairs in the valence and the conduction bands. The dynamic interaction of these electron-hole pairs within the optical field is facilitated by the dipole matrix elements which is a function of reciprocal wave vector,  $k$ ; this dynamic interaction involving vertical transitions of the carriers in the electronic band structure of dielectrics is known as interband polarization. Simultaneous to the build-up of interband polarization is

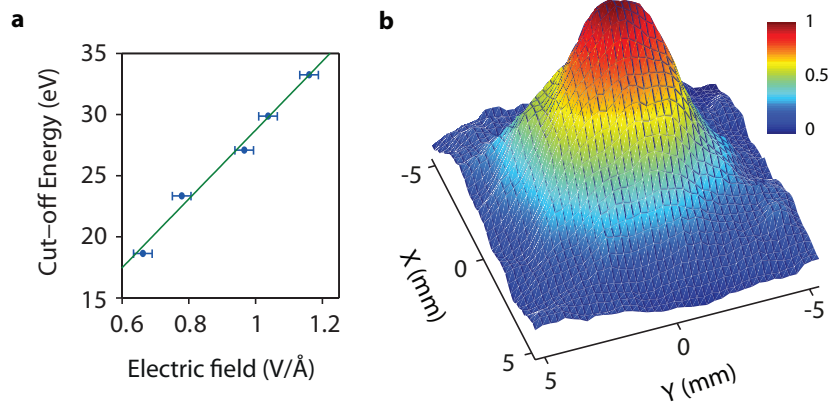


Figure 3.2: **a**, Scaling of cut-off energy with the driving field strength of EUV emission measured with a 1.5 cycle driving waveform. **b**, Far-field spatial intensity profile of EUV emission measured with an image intensifier. This figure has been adapted from [23].

the motion of the generated carriers; electrons and holes along the valence and the conduction band respectively. A meticulous modeling of the interaction of dielectrics with optical fields can be performed with the help of Semiconductor Bloch equations [47][58][59][60] (SBEs) wherein bifurcation of contribution of field induced dipole into inter and intraband contributions is possible. It helps us to discreetly say about the dominant mechanism underlying high harmonic generation. A simpler path of modelling the optical field interaction with dielectrics is to ignore the excitation step leading to generation of carriers but rather consider solely the intraband motion of a pre-excited wavepacket along the bands, this semiclassical approach can be implemented by using the Boltzmann transport equation [61][24].

Extrapolation of the cut-off energy Vs. field strength plot to void field strengths brings  $E_{cutoff} \sim 0.6 \pm 2.0 eV$ , which suggests to the intraband motion of the carriers (i.e.  $E_{cutoff} \approx 0$  for  $F=0$ ) being the mechanism behind HH emission in  $SiO_2$  else  $E_{cutoff} \sim E_g$  for an interband mechanism where for field strength approaching void values we expect to have minimally the polarization build-up corresponding to the bandgap at the  $\Gamma$  point, as the carriers may not be excited elsewhere along the dispersion profile of the bands due to weak field strengths. Lately, HH emission in ZnO crystals driven by mid infrared laser pulses has been linked to interband polarization interpreted within a three step model, wherein the first step is a tunneling step i.e. generation of carriers via a vertical transition from valence to the conduction band followed by motion of electron-hole pairs in opposite directions along the band and eventually their recombination. Within the scope of such experimental conditions an offset in  $E_{cutoff}$  corresponding to the bandgap of the material under study for  $F=0$  is expected but it remains still to be demonstrated.

Investigating spectral amplitude scaling of particular harmonic orders lends additional support in favour of intraband over interband mechanism for EUV emission in  $SiO_2$ . As shown in Figure 3.3 is the spectral amplitude scaling for 11<sup>th</sup> harmonic order, it follows more

closely with theoretically calculated scaling from intraband term compared to the scaling computed from interband mechanism in a two band SBE calculation. Spectral amplitude scaling from interband contribution varies much more nonlinearly compared to intraband term.  $\text{SiO}_2$  has a hexagonal closed packing lattice structure (hcp) which implies that there are three important directions inside Brillouin zone (BZ) i.e.  $\Gamma$ -K,  $\Gamma$ -M which lie in one plane and  $\Gamma$ -A which is perpendicular to this plane (along c-axis of  $\text{SiO}_2$ ). Of these three directions, band structure along  $\Gamma$ -M direction is most dispersive and hence dominates the spectrum in the entire investigated bandwidth in this work as is shown in Figure 3.4, so the SBE calculations were performed considering only the  $\Gamma$ -M direction. Even a better agreement in spectral amplitude scaling can be achieved with semiclassical approach i.e. intraband spectra generated by acceleration of a pre-existing electronic wavepacket in the first conduction band along  $\Gamma$ -M direction.

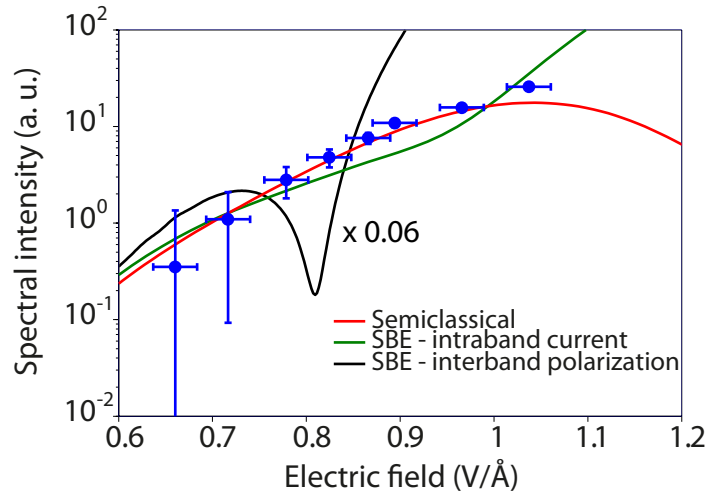


Figure 3.3: Spectral amplitude scaling of 11<sup>th</sup> harmonic as measured in our experiment compared to that simulated from semi-classical and Quantum-mechanical simulations. This figure has been adapted from [23].

Comprehension of the fact that discrete odd HH peaks in EUV spectra arise from interferences of the nonlinear dipoles generated from consecutive half-cycles of the optical driver waveform attests to the high degree of coherence of EUV generation process in  $\text{SiO}_2$ . Coherent properties of EUV emission in  $\text{SiO}_2$  can be further verified by measuring its far field beam profile. EUV beam-profile measurements from  $\text{SiO}_2$  reveal a nearly circular (ellipticity  $\sim 0.93$ ) and an almost diffraction limited beam with an evaluated divergence of  $\sim 7$  mrad. The measured divergence of EUV beam is very close to the divergences of the beam measured for gas HH [62][63].

Profound spectral control over EUV emission in gases can be achieved by variation of the carrier envelope phase [64] (CEP) of the driving few-cycle laser pulses. In contrast to gases only limited spectral control can be achieved on variation of CEP while using few-cycle, 1.5 cycle and a single cycle driving waveforms. Only when optical attosecond

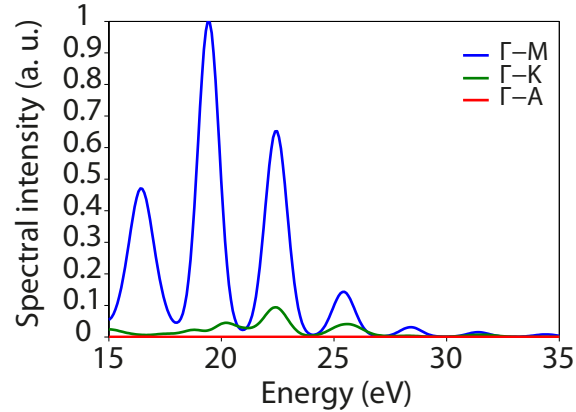


Figure 3.4: Spectra calculated by intraband motion of electrons in the first conduction band of SiO<sub>2</sub> along three different directions of Bouillon zone driven by a 1.5 cycle optical pulse. This figure has been adapted from [23].

pulses are used to generate EUV emission, spectral control is achieved by variation of CEP from 0 to  $\pi/2$  rad as presented in Figure 3.5. Spectral control is also manifested when one of the constituent channels of light-field-synthesizer is moved  $\pi/2$  rad out of phase with respect to other channels from their temporal overlap configuration generating an optical attosecond pulses as shown in Figure 3.5. The reduced sensitivity of EUV emission on CEP of driving pulses can be attributed to the fact that intraband scattering of carriers along the bands in SiO<sub>2</sub> is a much less nonlinear process following a Bessel type scaling [65][23]. The achieved spectral control is primarily dependent on the ability of controlling carriers trajectories by sculpting driving optical waveforms; contrary to HH process in gases where EUV emission is not merely dependent on electrons trajectories but also on the tunneling step which follows exponential dependence on field strength and strongly affects the ability to spectrally control the emission.

Finite recombination probability ( $< 10^{-6}$ ) of electrons with ionic core in gas phase EUV generation process limits the EUV photon flux that can be achieved. Intraband dominated EUV emission from SiO<sub>2</sub> does not require this stringent criterion and hence is expected to be a superior source compared to gases for EUV generation under similar conditions of experiment. We have recorded EUV spectra from Kr, Ar (two standard gas phase EUV sources) and SiO<sub>2</sub> with increasing intensity of a 1.5 cycle driver pulse. For an equitable comparison with SiO<sub>2</sub>, number density of gas-phase entities in the laser interaction region were made similar to SiO<sub>2</sub>. Comparison of spectral flux scaling in Figure 3.6 shows that indeed SiO<sub>2</sub> is a superior EUV source compared to gases in the investigated range of experimental parameters. We foresee the possibility of generating bright solid-state EUV sources.

Coherent build-up of flux of EUV photons in SiO<sub>2</sub> is hindered by their absorption during propagation inside the nanofilm along with the phase matching criterion for EUV photon wavevectors generated from different points inside the nanofilm. Following the

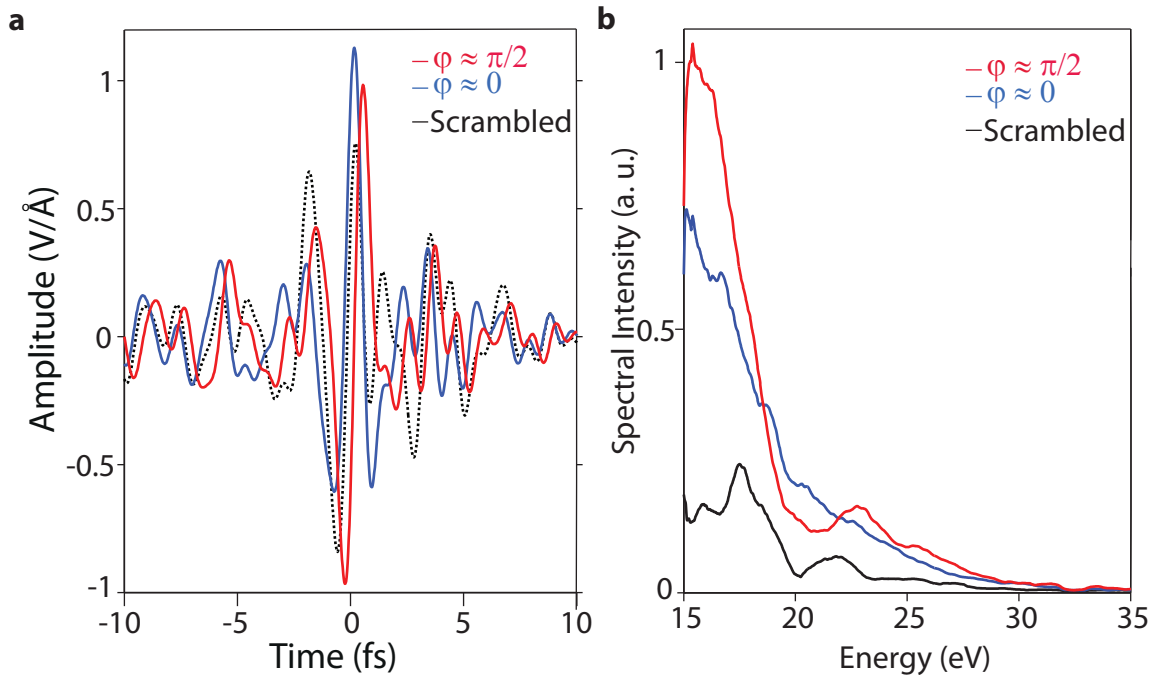


Figure 3.5: Spectral control over EUV emission steered by sculpted light waveforms: **a**, optical attosecond pulse; red curve - CEP = 0 rad; blue curve - CEP =  $\pi/2$ rad and a scrambled waveform (black dashed curve). **b**, EUV spectra generated by optical waveforms shown in **a**.

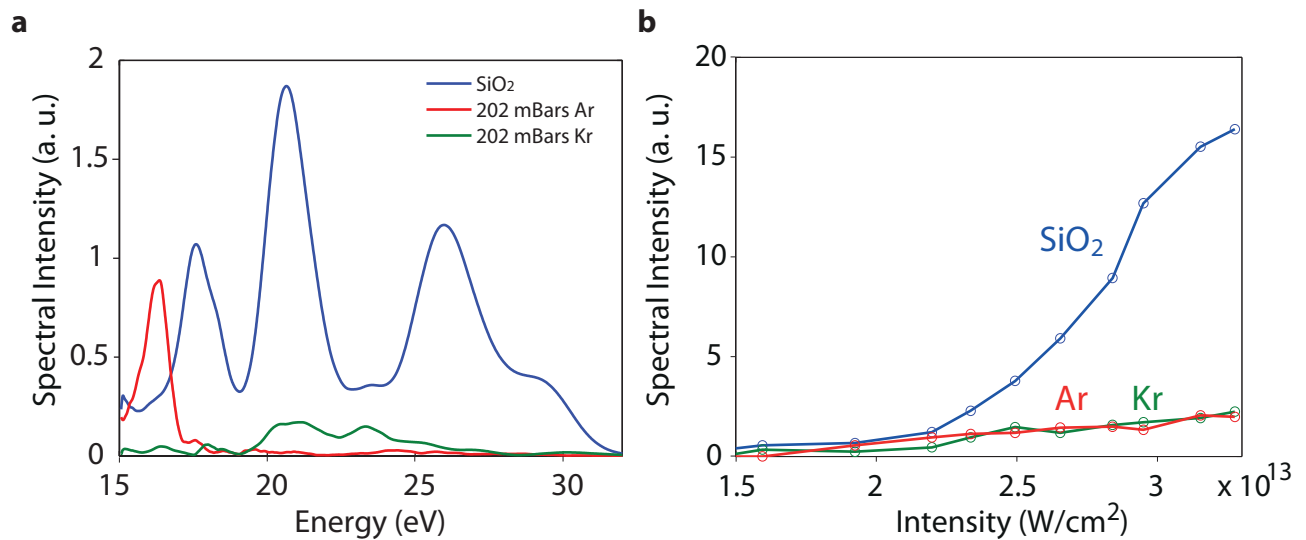


Figure 3.6: **a**, Comparison of spectra emitted by identical number of emitters in  $\text{SiO}_2$ , Ar and Kr with intensity of driving optical pulse being  $2 \times 10^{13} \text{W/cm}^2$ . **b**, Comparison of spectral flux scaling of  $\text{SiO}_2$  with Ar and Kr under similar experimental conditions.

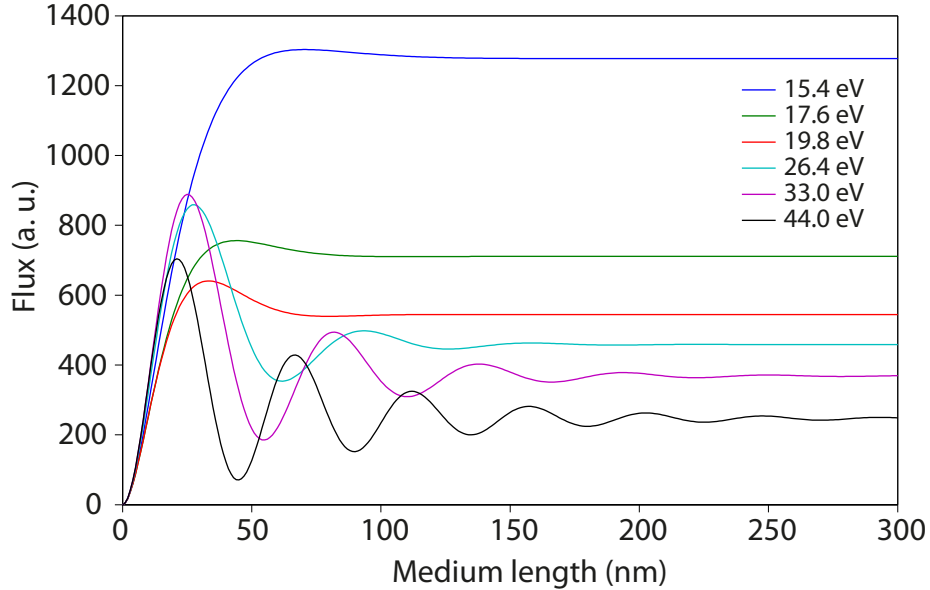


Figure 3.7: Phase matching considerations of EUV generation in  $\text{SiO}_2$ . Buildup of EUV flux versus propagation length calculated for representative photon energies (mentioned in the legend). Material parameters are taken from Ref. [68]. Comparable results (within 10% accuracy) can also be obtained based on data from Ref. [69] for photons higher than 30 eV.

work of Constant, E. et al [66][67] we calculate the flux for different photon energies assuming constants for silica found in Ref. [68]. The results shown in Figure 3.7 suggest that the lowest EUV photon energies in our spectrum undergo a coherent buildup for propagation lengths on the order of 80-100nm while corresponding lengths for the higher photon energies of our spectra are  $< 50\text{nm}$ . For these reasons the selection of a film of a thickness of  $\sim 100\text{nm}$  is a reasonable choice and permits minimization on nonlinear and linear distortion of the ultrafast driving fields (particularly the optical attosecond pulses) caused by propagation through the medium.

Extension of EUV photon energies to more than 40 eV was possible by driving the  $\text{SiO}_2$  samples with intense optical attosecond pulses with peak field strengths  $\sim 1.4 \text{ V/\AA}$ , gradual increase in spectral amplitude as well as cut-off scaling of EUV emission with field strength of optical attosecond pulses is shown in Figure 3.8. The physical damage of the sample in this case was also subdued by their lateral movement with respect to the optical beam. In the future, we anticipate that it will be possible to appropriately engineer the band structure [70] of solids so as to be able to generate even more nonlinear intraband currents leading the way eventually to soft X-ray solid-state sources.

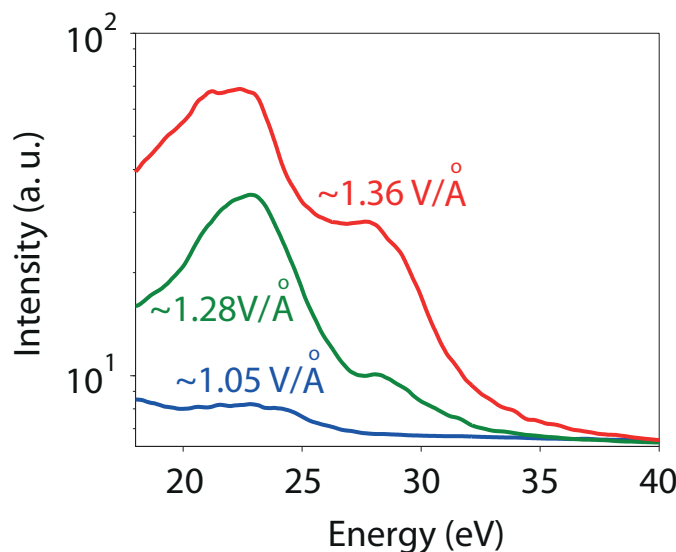


Figure 3.8: Cut-off scaling of EUV emission continua to more than 35 eV by driving  $\text{SiO}_2$  nanofilms with increasing field strengths of an optical attosecond pulse.

### 3.3 HH spectroscopy of solids

Meticulous study of changes in HH spectra as a variation of one of the parameters of driving laser pulses e.g. intensity or one property of system under study e.g. its alignment angle with respect to laser polarization axis has enabled researchers in the past to discern several features of electronic states, evolution of electrons through which is directly imprinted on HH spectra as well as tomographic imaging of the electronic wavepackets was also possible [53][20]. In the same spirit we explore the possibilities of extracting band structure information from our measurements of different spectral amplitude scaling as a function of driving field strength observed for different HH orders. As the physical signatures from our measurements point to intraband mechanism behind EUV generation but involvement of multiple electronic bands cannot be ruled out in such a case and the EUV spectrum may be arising from an intricate coupling of intraband currents arising from different bands. The first conduction band of  $\text{SiO}_2$  is distantly separated from rest of the conduction bands hence the population of electrons generated in first conduction band compared to the rest drops exponentially; also the spectral amplitude scaling from first conduction band alone is sufficient to justify the experimentally observed scaling for 11th harmonic order as shown in Figure 3.3. The contribution of the intraband current generated by the holes in the highest valence band can also be ignored owing to its less dispersive profile hence contributing negligibly to the EUV spectra from  $\text{SiO}_2$  [23]. Convincingly we can only consider the intraband currents generated from first conduction band in the  $\Gamma$ -M direction alone to be responsible for EUV emission in  $\text{SiO}_2$ .

Herein we attempt to reconstruct fine details of the dispersion profile of the first conduction band of  $\text{SiO}_2$ . Within the tight-binding model beyond the nearest-neighbour approx-

imation, the energy dispersion of the  $i^{th}$  band can be written as summation over several spatial harmonic components as;

$$E_i(k) = \sum_{n=0}^{max} \epsilon_{i,n} \cos(nka) \quad (3.1)$$

The intraband current generated by the carriers for different spatial harmonic orders is given by;

$$J(t) = \frac{-2e}{((2\pi)^3)} \int_{BZ} v_c(k, t) f_c(k) d^3k \quad (3.2)$$

Group-velocity of the carriers is proportional to curvature of the respective bands  $v_c(k, t) = \frac{1}{\hbar} \frac{\partial E_c(k(t))}{\partial k}$ , which entails to higher nonlinear current coming from higher spatial order contribution to the overall intraband current. Higher nonlinear current connotes to superior contribution in the overall spectrum coming from higher spatial harmonic terms than the lower ones. The simulated spectra arising from different spatial order component of decomposed dispersion profile as per Eqn. (3.1) of the first conduction band are shown in Figure 3.9. Evidently the higher spatial orders contribute more to the spectral amplitude for all the energy bandwidth investigated in the present study. Also, the power scaling laws followed by different spatial harmonic components for harmonic orders  $11^{th}$  and  $15^{th}$  of the fundamental driving laser pulse are significantly different as shown in Figure 3.9d, Figure 3.9e. The measured spectral amplitude scaling with respect to driving field strengths for the  $11^{th}$  and the  $15^{th}$  HH (Figure 3.10) component in the spectra can be reproduced well by only considering the contribution coming from the  $5^{th}$  ( $E_c(k) = \epsilon_5 \cos(5ka)$ ) and  $6^{th}$  ( $E_c(k) = \epsilon_6 \cos(6ka)$ ) spatial harmonic terms respectively in the band dispersion profile within the semiclassical approach as presented in Figure 3.10b, c. Semiclassical theory predicts the spectral scaling of  $N^{th}$  harmonic of fundamental driving frequency at  $\omega_L$  to follow Bessel function type dependence on field strength and is given by;

$$I_N \propto (N\omega_L)^2 \left| J_N \left[ \frac{eF_0 a}{\hbar\omega_L} \right] \right|^2 \quad (3.3)$$

where  $J_N(z)$  is the Bessel function of the first kind of order  $N$  and  $F_0$  is the peak field strength of driving laser pulse. A band whose dispersion profile can be expressed by considering only few spatial harmonic terms, the above relation for spectral amplitude scaling for  $N^{th}$  harmonic can be generalized as

$$I_{c,N}(\omega_L, F_0) \propto (N\omega_L)^2 \left| \sum_{n=1}^{n_{max}} n \epsilon_{c,n} J_N \left[ \frac{n\omega_B}{\omega_L} \right] \right|^2 \quad (3.4)$$

From the above equation, the experimentally measured ratio of the spectral scaling of  $11^{th}$  and  $15^{th}$  harmonic  $\frac{I_{c,15}}{I_{c,11}} \propto \frac{\epsilon_{c,6}}{\epsilon_{c,5}}$  yields the ratio of the amplitudes of  $6^{th}$  spatial harmonic with respect to the  $5^{th}$  spatial term in the dispersion profile of the first conduction band. The evaluated ratio of  $\frac{\epsilon_{c,5}}{\epsilon_{c,6}} \approx -5.1 \pm 0.6$  is very close to the one theoretically calculated. The ability to measure the effect of  $6^{th}$  spatial harmonic terms contribution to EUV spectrum

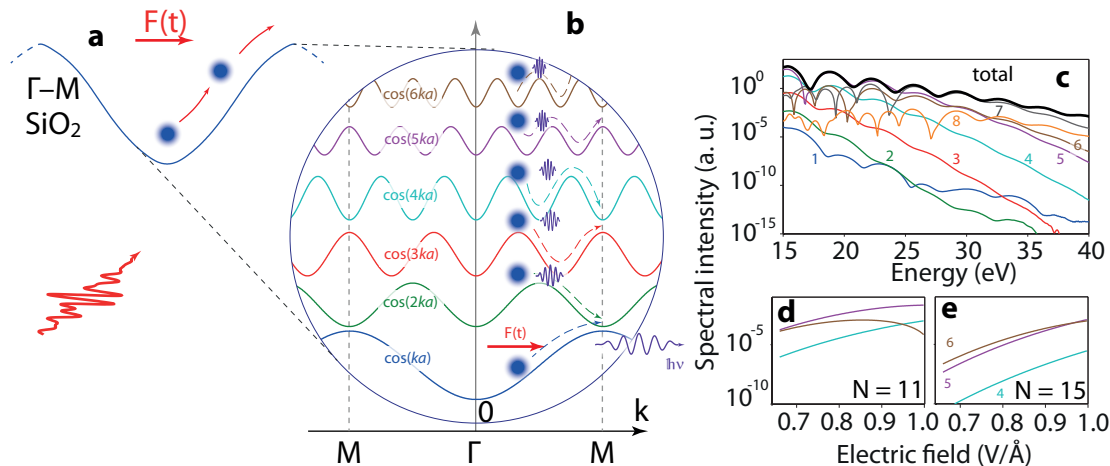


Figure 3.9: High harmonic spectroscopy of solids: **a**, Schematic description of an electronic wavepacket being driven by the laser pulse in the first conduction band of  $SiO_2$ . **b**, Decomposition of the band dispersion profile shown in **a** to different spatial harmonic components, the relative amplitudes of the decomposed spatial profiles are scaled for clarity. **c**, Spectra arising from nonlinear intraband current generated by the electronic wavepacket motion in different spatial harmonic dispersion profiles. **d**, **e**, Comparison of spectral amplitude scaling of 11<sup>th</sup> and 15<sup>th</sup> HH component in the simulated spectra obtained from nonlinear currents generated from 4<sup>th</sup>, 5<sup>th</sup> and 6<sup>th</sup> spatial harmonic components independently. This figure has been adapted from [23].

implies to a spatial resolution of  $\sim \pi/6a \approx 0.1 \text{ \AA}^{-1}$  which is competent with the resolution offered by modern angular resolved photoelectron spectroscopy [54]. Measurement of lower harmonic orders ( $< 15 \text{ eV}$ ) in the future will further enable us to extract information of the amplitudes of lower spatial harmonic terms in the dispersion profiles of the conduction band. Efforts towards a complete reconstruction of the real space potential of a solid from the HH spectroscopy are also being currently pursued.

## 3.4 Conclusions

In conclusion, emission of coherent EUV radiation from a bulk solid SiO<sub>2</sub> has been demonstrated. The physical signatures present in the recorded EUV spectra indicate to the intraband motion of electrons in the first conduction band of SiO<sub>2</sub> playing the significant role towards EUV emission. The methodical study of EUV spectra has enabled for the first time to unveil fine details of dispersion profile of first conduction band of SiO<sub>2</sub> within the scope of a polarization spectroscopy which was hitherto not possible with conventional photoemission techniques in wide bandgap dielectric materials due to spatial charging effects leading to a reduced resolution. The capability to probe fine spatial details of dispersion profile varying in the scale of only 0.1 Å shows that spatial resolution offered by EUV

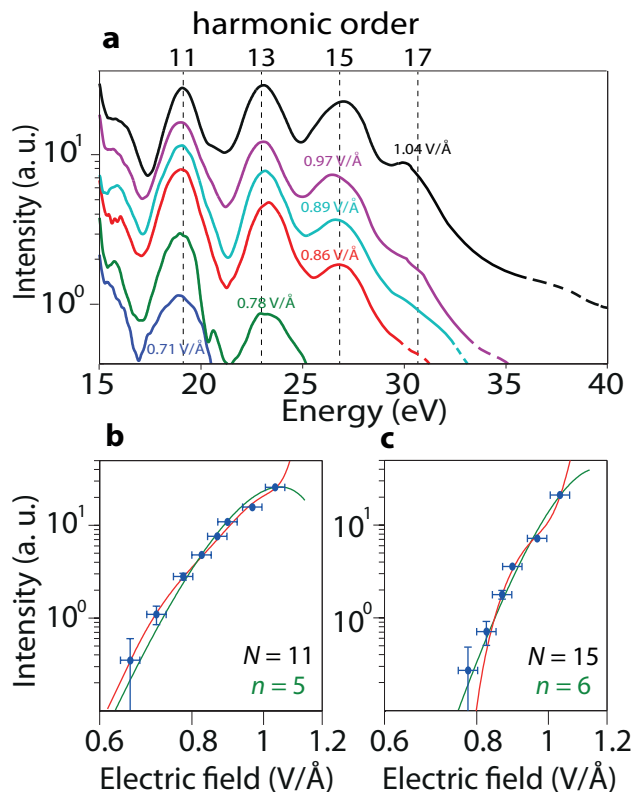


Figure 3.10: HH spectroscopy of solids: **a** EUV spectra measured by increasing the peak field strength of a 1.5 cycle driving optical waveform. **b**, **c**, Spectral amplitude scaling measured for 11<sup>th</sup> and 15<sup>th</sup> harmonic order respectively by methodically increasing the field strength of the driving waveform of 1.5 cycles. The observed spectral scaling of 11<sup>th</sup> and 15<sup>th</sup> harmonic order can be reproduced well by only considering 5<sup>th</sup> and 6<sup>th</sup> spatial harmonic component respectively of the first conduction band in the semiclassical approach of simulating EUV spectra. This figure has been adapted from [23].

HH spectroscopy is competent with the one from photoemission spectroscopies (ARPES). Measurements toward a full reconstruction of real space potential in SiO<sub>2</sub> are currently being pursued.

Spectral studies of EUV emission may not transparently bring about information of underlying dynamics of carriers emitting coherent radiation in SiO<sub>2</sub>, as has been the case for HHG in ZnO where spectral and time-resolved measurements support contrasting mechanisms of HH emission [52][22]. So performing time-resolved experiments of EUV emission from SiO<sub>2</sub> is inevitable to decipher mechanism of EUV emission in SiO<sub>2</sub>. Also, the spectral domain studies suggest CEP variation of single-cycle optical pulses being capable of spectrally controlling the EUV emission, performing a time-resolved measurement would allow us to directly impart this control in the time domain, where temporal features of emitted EUV pulses for two different CEPs of driving optical pulses may encompass signatures of

dominant mechanism of EUV emission. Such measurements would also open up the way to generate isolated attosecond pulses from solids which is deemed as a major milestone in laser-driven high harmonics in solids [52][56][71].



# Chapter 4

## Real-time tracing and attosecond control of multi-PHz electric currents in solids

### 4.1 Introduction

In the previous chapter an earlier work on EUV generation from  $\text{SiO}_2$  extending upto  $\sim 40\text{eV}$  [23] was presented. Means of EUV generation is attributed to intraband motion of optically generated electrons in the first conduction band of  $\text{SiO}_2$ . Time-resolved studies of HHG in  $\text{ZnO}$  [52] has revealed interband dominated mechanism in contrast to conjectured intraband dominated mechanism from spectral domain measurements [22]. Also, HHG in THz driven  $\text{GaSe}$  was earlier reported to be arising from dynamical Bloch oscillations assisted by interband transitions between the bands [48]; although after time-resolved experiments were performed experimentally observed dual chirp behaviour was explainable by the dynamical Bloch oscillations but observed synchrony between HH field and driving THz field could only be explained by interference of transitions of electrons-hole pairs between the electronic bands [56]. In view of the situation that time-resolved studies connote to contrasting mechanisms of HHG with respect to spectral domain measurements and at the same time they can provide more insights into the process, performing a time-resolved study for EUV generation from  $\text{SiO}_2$  is inevitable.

Scrutinizing temporal characteristics of EUV emission holds exemplary benefit in the field of light-wave electronics [39]; where insights into the mechanism of EUV emission which connote to underlying ultrafast charge oscillations will eventually open up the gateway for electronics operating at multi-PHz frequencies.

### 4.2 Experimental Details

Herein we have exploited the toolbox of attosecond metrology [31][26] to study the temporal features of EUV emission from  $\text{SiO}_2$ . Optical pulses from a light field synthesizer [37] [36]

[57] were focused by a 60 cm concave mirror onto a 120 nm thick SiO<sub>2</sub> polycrystalline nanofilm and the emerging EUV emission from SiO<sub>2</sub> was spectrally filtered by 150 nm thick Al foil and spatially separated from optical pulses by exercising the fact that divergence of EUV emission is much smaller than that of laser pulse, also Al foil blocks the transmission of laser pulse. In order to have minimal artificial effect on spectral phase of EUV pulses due to reflection from a mirror, we have used a Gold coated mirror instead of standard multilayer mirrors routinely used for reflection of EUV pulses [72]; multilayer optics may affix undesired spectral phase jumps on the EUV pulse. Optical driver and EUV pulses are delayed with respect to each other by a piezo stage before being focused on a Ar gas nozzle, photoelectrons hence generated are detected and analysed by a time of flight (TOF) mass spectrometer. The intensity of the optical pulses is kept low ( $< 10^{12}W/cm^2$ ) such that they do not generate photoelectrons by themselves. The pressure of Ar in the gas nozzle was optimised so as not to have any spatial effect on the photoelectron spectrum (per se *broadening*) while still maintaining good counts on TOF. A photoelectron spectrogram is recorded as a function of delay between the two pulses. The momentum of photoionized electrons generated by EUV pulse is streaked up and down in energy by the optical pulse. The experimental set-up is shown in Figure 4.1, free standing SiO<sub>2</sub> nanofilm was put on a 3D stage for convenience of moving the sample in and out of focus and also moving the sample in a direction lateral to the optical beam after every photoelectron spectrum measurement. The spectral phase introduced by  $\sim 150nm$  Al foil and Au-coated EUV mirror are shown in Figure A.1 in Appendix A along with their transmission and reflectivity curves respectively.

Measuring a photoelectron spectrum arising from SiO<sub>2</sub> and a simultaneous measurement of spectrum in a EUV spectrometer reveals the spectral response of electrostatic lens in the TOF spectrometer, which is found to be a Gaussian with a FWHM of  $\sim 9$  eV. The voltage in electrostatic lens can be adjusted to increase the acceptance angle of photoelectrons with a specific central energy in TOF spectrometer. Energy axis in TOF spectrometer was calibrated using  $N_{4,5}OO$  Auger lines in Xenon [73] excited by a EUV pulse centered at 95 eV. Figure B.1 in Appendix B shows measured Auger lines in Xenon and its comparison with a reported  $N_{4,5}OO$  spectral lines measured at a synchrotron facility. All the photoelectron spectrum were also corrected with a Jacobian multiplier accounting for spectral axis conversion from time to energy.

A methodical comparison of the spectral phases imparted by different components in the measurement set-up is made in Appendix C and a discussion to their significance in the conclusion reached in this work is also presented.

### 4.3 Reconstruction of EUV and driving optical pulses by PCGPA

A principal component generalized projections algorithm [74][75] (PCGPA) has been used to analyse the experimental spectrogram (see Appendix D for more details). For better

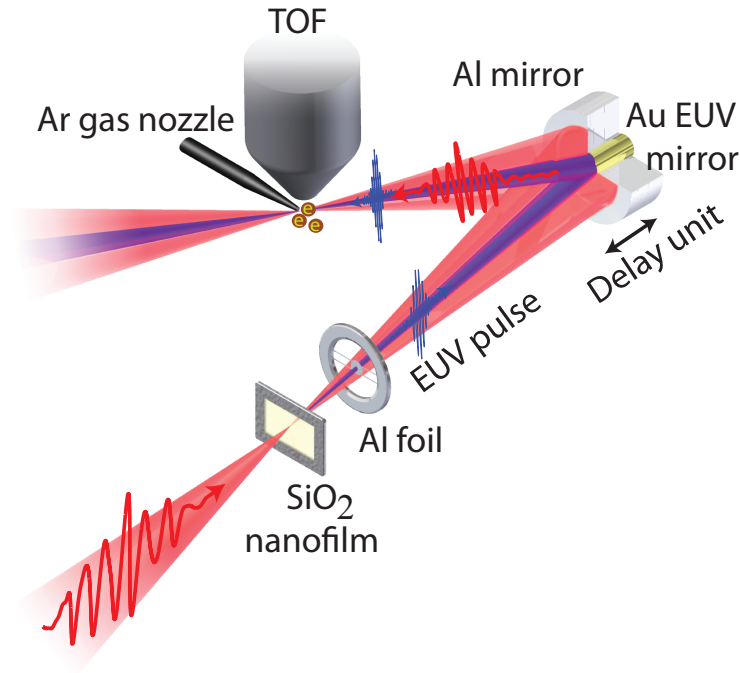


Figure 4.1: **Experimental setup.** The radiation emanating from SiO<sub>2</sub> nanofilms ( $\sim 120\text{nm}$ ) was spectrally filtered ( $> 15\text{ eV}$ ) and spatially separated from the light waveform generating EUV radiation. Both beams were temporally delayed with respect to each other and were focused on an Ar gas target by a two-component concentric mirror assembly. The photoelectron spectra were recorded by a time-of-flight (TOF) spectrometer as a function of the time delay between the two pulses.

reconstruction of spectrograms a Gaussian filter correction (subtracting each spectrum by 10 % of its peak amplitude) was applied to each photoelectron spectrum, this correction is only to make spectrograms cleaner for analysis, in other terms removing the part of the photoelectron spectrum which is unperturbed (not streaked) by the optical pulse. A comparison of measured and reconstructed spectrogram after the convergence of the algorithm in approximately  $10^4$  iterations with a final error of less than 2% is shown in Figure 4.2. PCGPA reconstruction algorithm allows extraction of both the driving optical pulse and the EUV pulse. The retrieved EUV pulse with its field envelope are shown in Figure 4.2. Pulses as short as  $\sim 450$  as are measured, this is the first measurement of an isolated attosecond pulse generation from a solid. Spectral phase and EUV spectrum retrieved from PCGPA are shown in Figure 4.2 , features of the spectral phase will be commented on later. The pulse duration of the optical driver as retrieved by PCGPA is  $\sim 2.8\text{ fs}$  and its bandwidth varies from  $\Delta_L \approx 0.9 - 3\text{ eV}$  with centre frequency being at  $\omega_L \approx 1.9\text{ eV}$ . The weak phase and amplitude distortion imposed on the photoelectron

spectra by the dipole matrix elements describing transitions from ground to continuum states [76] (for Ar) in the studied spectral range is also accounted for in the reconstruction, data for the complex dipole matrix elements is taken from Wei et al. [76]. Yet these distortions are minor and do not significantly affect the retrieved quantities.

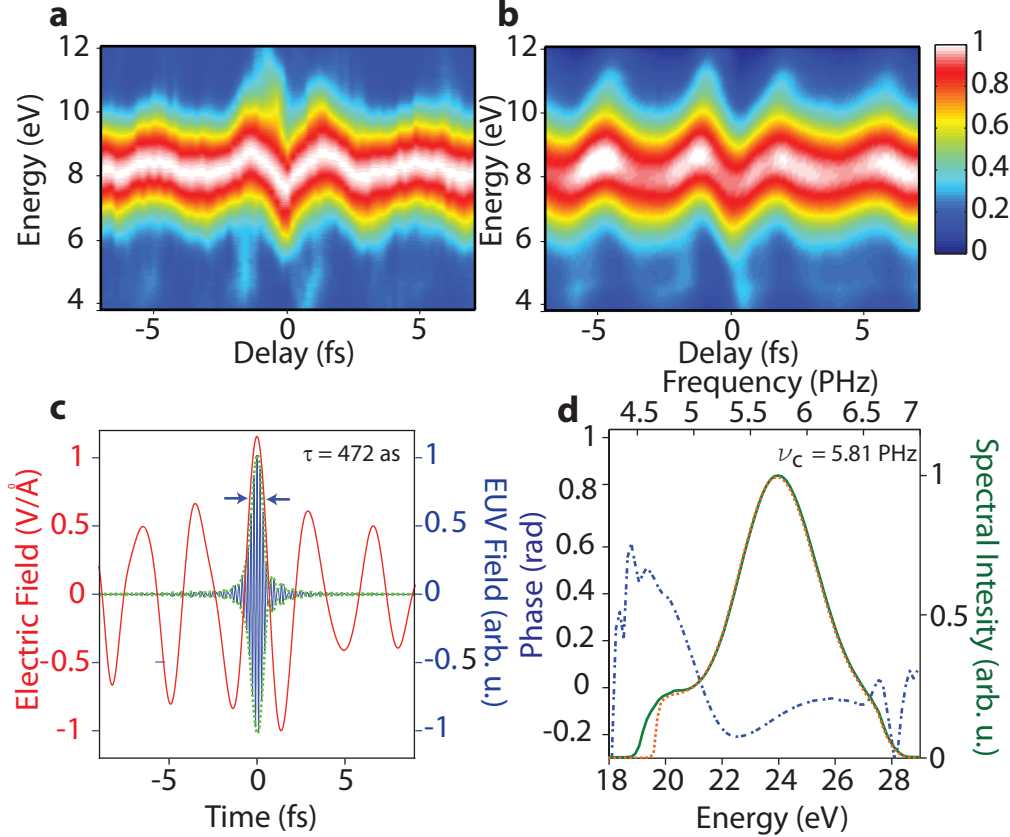


Figure 4.2: **Reconstruction of Attosecond streaking spectrograms measured with EUV emission from SiO<sub>2</sub>.** **a**, Experimentally measured attosecond-streaking spectrogram. **b**, Reconstructed streaking spectrogram. **c**, Retrieved temporal profiles of an isolated attosecond pulse (blue line) and the driving optical field (red line) with peak field strength of  $\sim 1.1$  V/Å inside the nanofilm, and their timing at the source. **d**, Retrieved spectral phase (blue dashed line) and spectrum (orange dashed line) of the EUV pulses. The green solid line represents the spectrum of the EUV pulses measured in the absence of the streaking field.

To investigate the extent to which the fine details of temporal features of an attosecond pulse from SiO<sub>2</sub> can be reconstructed from our experimentally measured data we turn to gas phase measurements where the discrete feature of chirped nature of EUV emission [33][10] has to be deducible. We generate and characterize EUV pulses in Ar gas under identical experimental conditions of intensity, driving pulse duration and spectral range with that of our SiO<sub>2</sub> experiments as shown in Figure 4.2. Figure 4.3 shows the measured streaking

spectrogram and retrieved attosecond pulse from Ar.

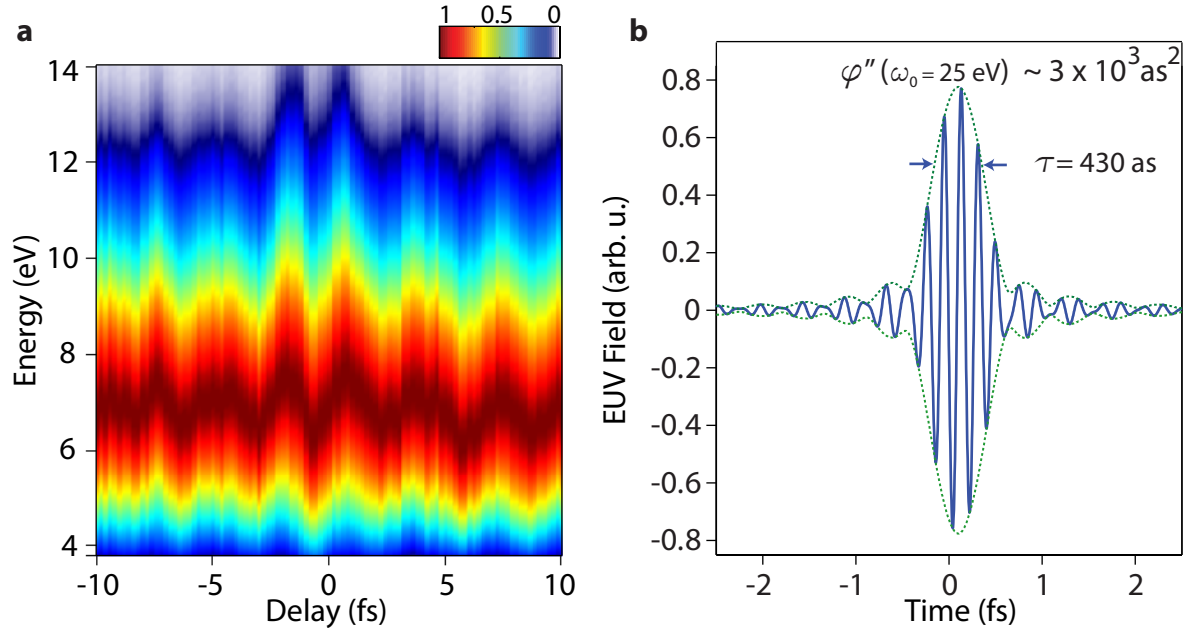


Figure 4.3: **a**, Measured attosecond streaking spectrogram with EUV pulses generated in Ar. **b**, Retrieved attosecond pulse and GDD carried by its field waveform.

The time-frequency analysis of the retrieved attosecond pulse in Figure 4.3b is shown in Figure 4.4 and reveals a positively chirped EUV emission. Orange-curve is to guide the eyes. The retrieved GDD of attosecond pulse is  $\sim 3 \times 10^3 \text{ as}^2$  ( $\omega_0 = 25 \text{ eV}$ ). The retrieved group delay (emission time) of EUV photons as experimentally measured is in close agreement with the simulations from semiclassical model [77] shown in Figure 4.5. This measurement attests to high temporal resolution of our experimental set-up and provides a firm base to study temporal features of EUV pulses retrieved from  $\text{SiO}_2$ .

We now attempt to look for the spectral features of positive chirp in our experimentally recorded spectrograms in Figure 4.3 as well as the ones reconstructed. Positive chirp of the generated attosecond pulses in Ar (Figure 4.3) is directly manifested in the experimental data, most profoundly on spectra recorded at the minima (zero-transitions) of the vector potential (Figure 4.6a). The corresponding narrowing and broadening of photoelectron spectra (Figure 4.6c) sampled at the negative and positive slopes of the vector potential respectively is the typical evidence of positive chirp which is also captured and reproduced by the reconstruction algorithm Figure 4.6c, d. The capability to capture in such detail the spectral features corresponding to chirp in our experimental and reconstructed spectrograms connote to measurement of a high quality data as well as its corresponding reconstruction.

The attosecond streaking spectrogram measured with EUV attosecond pulses generated in  $\text{SiO}_2$  (Figure 4.7) exhibit very different features in comparison to those in the gas

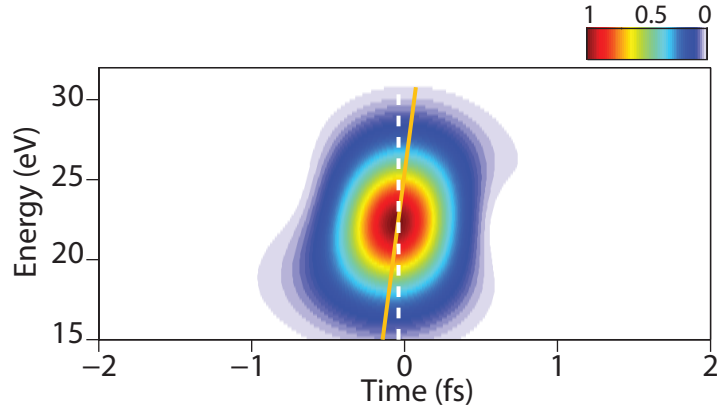


Figure 4.4: Time-frequency spectrogram of the retrieved EUV attosecond pulse from the measured streaking spectrogram shown in Figure 4.3. Solid orange curve is tilted and white dashed curve is vertical to connote for positive chirp of EUV emission.

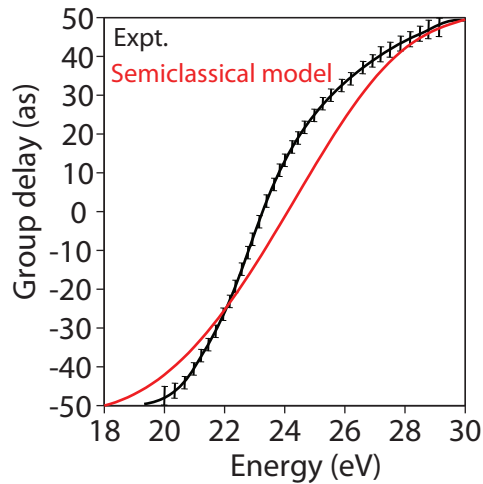


Figure 4.5: Comparison of experimentally retrieved group delay of the EUV attosecond pulse generated in Ar with the predictions of semiclassical model [77].

phase study. Indeed, spectra sampled at the zero-crossings of the vector potential of the streaking field reveal a very minor change in the width (FWHM) of the photoelectron spectra suggesting the absence of a linear chirp but reveal dynamics at both ends of the spectrum. These dynamics are perfectly captured by the reconstruction algorithm and are compatible with the generation of pedestals around the main EUV burst. The pedestals on the main EUV attosecond burst are required for the formation of these discrete spectral features as shown in Figure 4.7d, Figure 4.7e (see chirp free spectrogram Figure 4.7c). These features are not satellite EUV bursts in the conventional sense [78] as they are not generated at the adjacent field maxima but are closely attached to the main burst

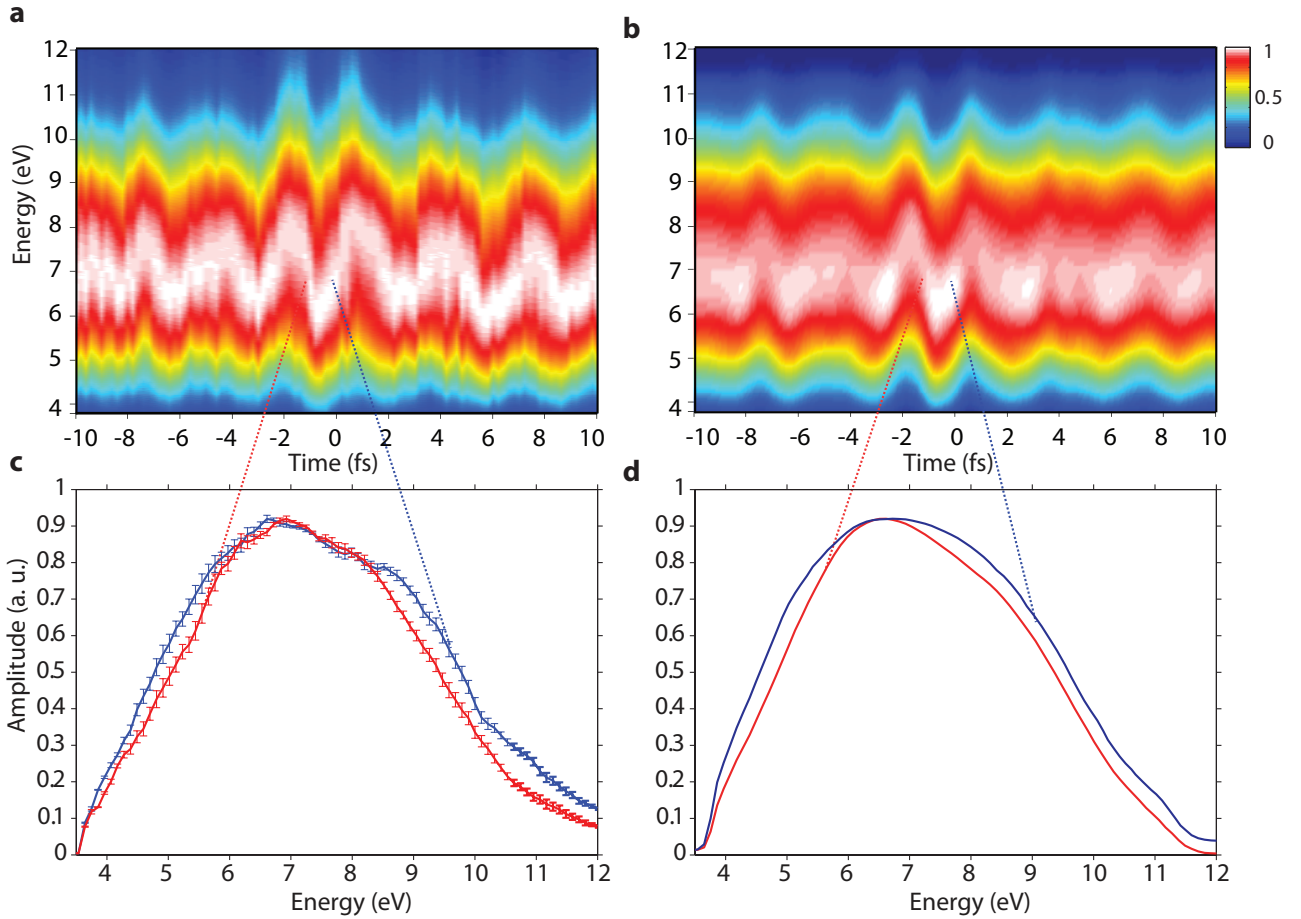


Figure 4.6: **a**, Attosecond streaking spectrogram measured with EUV attosecond pulses generated in Ar. **b**, Reconstructed spectrogram of measurement in **a** by PCGPA. **c**, **d** Representative spectra sampled at zero-crossings of the vector potential around the peak of the streaking field provide direct evidence of the positively chirped EUV dynamics. Error bars on experimental spectra are the standard error derived from consecutive measurements under identical conditions.

(Figure 4.2c). Their presence or disappearance can be controlled by the CEP of the driving field (which can adjust their spectral shape and cutoff, and it is responsible for spectral modifications of the emitted pulses under the high pass spectral filter set by Au mirror and Al foil in the experiment. These spectral features are discussed later and are directly relevant to the physics of the intraband current.

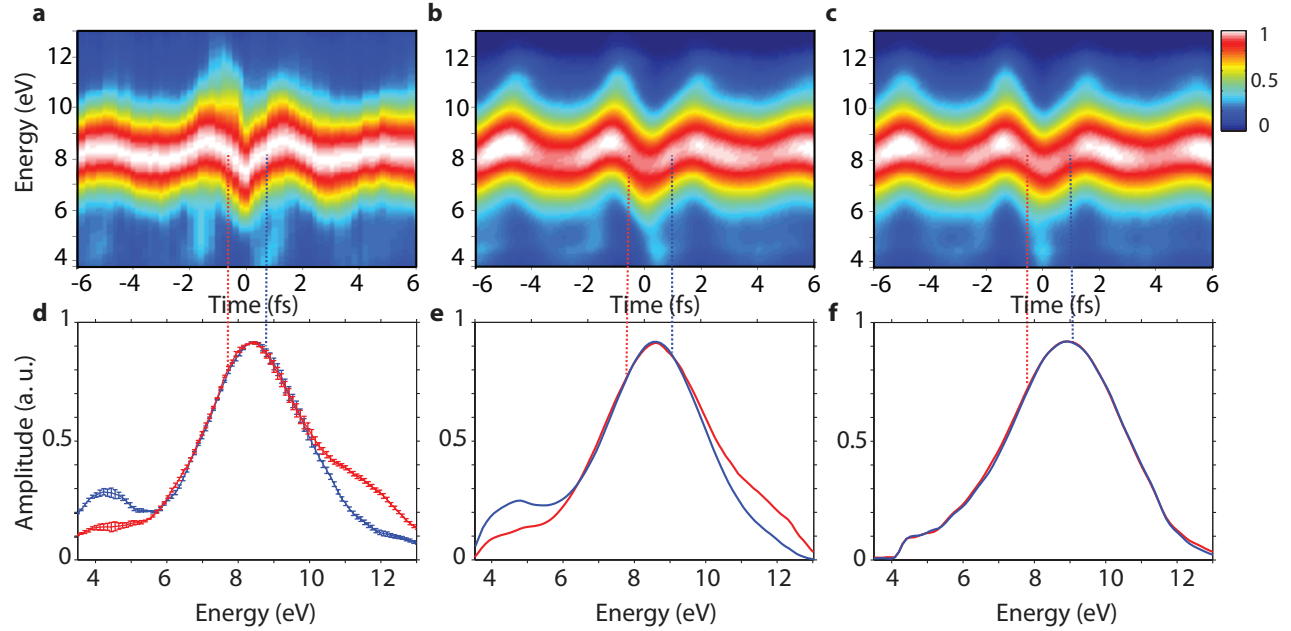


Figure 4.7: **a**, Attosecond streaking spectrogram measured with EUV pulses from  $\text{SiO}_2$ . **b**, Reconstructed spectrogram of measurement shown in **a** with PCGPA. **c**, Simulated streaking spectrogram using driving laser pulse as reconstructed by PCGPA and a perfectly symmetric EUV pulse obtained by numerical removal of the chirp from reconstructed EUV pulse in **b**. Comparison of photoelectron spectra at zero-crossings of the vector potential in measured **d**, reconstructed **e** and simulated **f** streaking spectrograms. Error bars on experimental spectra are the standard error derived from consecutive measurements under identical conditions.

## 4.4 Absolute calibration of delay unit

Ex situ characterization of EUV emission suffers from lacking the information of relative timing of EUV emission with respect to driving optical pulse which can be overcome by absolute calibration of the delay unit that is by precisely knowing the delay introduced by the inner-outer mirror in the measurement set-up in Figure 4.1. To enable this possibility, we perform a high order autocorrelation of the driving optical pulses reflected off from both inner Au and external Al mirror of the delay unit and record the yield of low energy ( $< 5$  eV) photoelectrons generated in Ar as a function of the delay between them. The delay-unit is interferometrically stabilized by observing spatial fringes arising from He-Ne laser falling on two mirrors to avoid the onset of drifts that could deteriorate the accuracy of measurements. Experimental set-up used for performing the above described measurement is shown in Figure 4.8.

The peak in the photoelectron counts determine the absolute time zero between the two mirrors, green line in Figure 4.9a. A comparison of the photoelectron yield as function

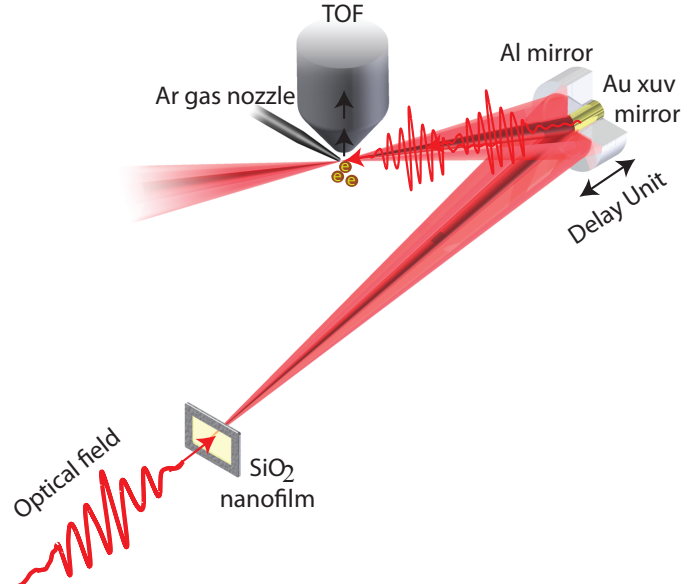


Figure 4.8: **Delay synchronization experimental set-up.** Optical driving laser pulses are reflected-off the dual mirror assembly and focused on an Ar gas jet, low energy electrons generated by highly nonlinear processes (e.g. direct or rescattered electrons in above threshold ionization) are detected in TOF.

of delay between the mirrors with the retrieved electric field intensity (blue line, Figure 4.9b) from a subsequent streaking measurement (Figure 4.9b), shows that peak of the photoelectron counts is synchronized to the peak of the electric field intensity, demonstrating the synchrony of EUV emission and peak of the electric field. Red error bar over the vertex in the photoelectron count measurement in Figure 4.9a shows the accumulated error ( $\sim 80$  as) along the time axis during the measurement.

To further verify the validity of our procedure we turn to gas phase measurements in Ar and we attempt to retrieve the relative timing of an isolated attosecond pulse generated in this system with respect to its driving field (Figure 4.10). As intuitively expected from short trajectory dominated emission [32], the EUV pulse is generated shortly before peak of the optical pulse, i.e. excitation in the previous half-field cycle and subsequent recollision close to the field minimum. This leads to the temporal offset between measured photoelectron counts as a function of delay and the retrieved field intensity, as is presented in Figure 4.10.

The arbitrariness in the time axis of the EUV pulse retrieved after convergence of PCGPA can now be firmly eliminated and the precise synchrony of optical and EUV pulse as established through above measurement is shown in Figure 4.2c.

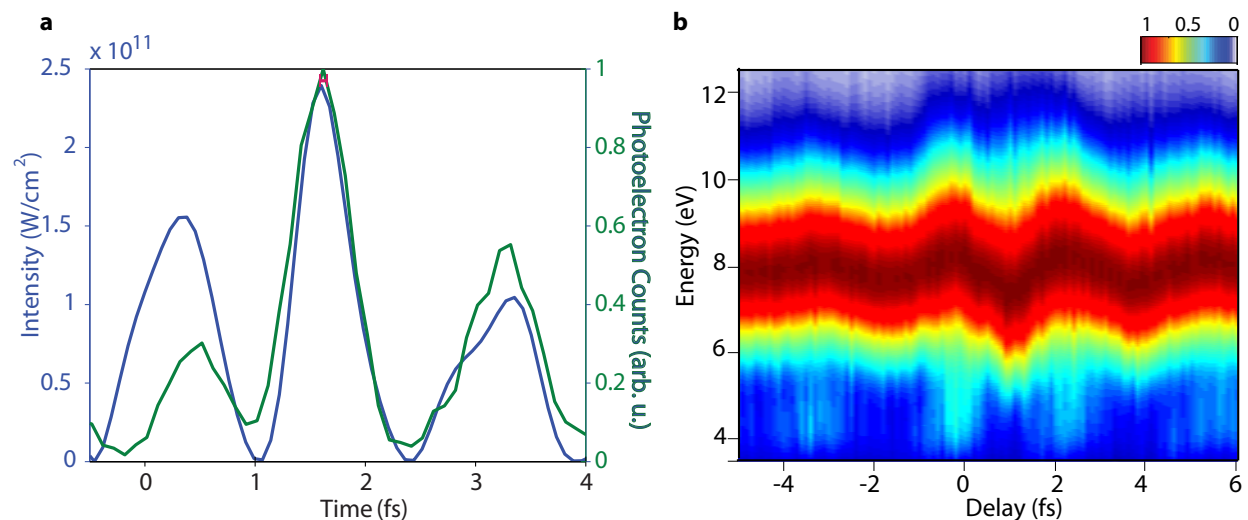


Figure 4.9: **a**, Photoelectron counts (green line) measured as a function of delay between two optical beams as shown in Figure 4.8. **b**, Attosecond streaking spectrogram measured with EUV emission from  $\text{SiO}_2$ . Optical driver field intensity (blue line, Figure 4.9a) as retrieved after convergence of PCGPA reconstruction of the experimental spectrogram.

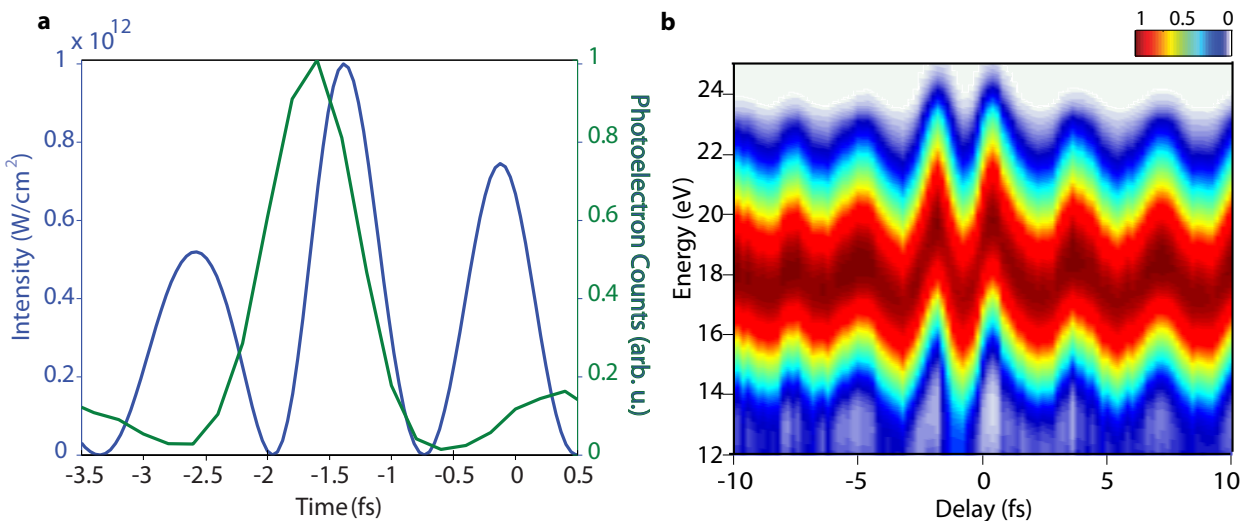


Figure 4.10: **a**, Photoelectron counts (green line) measured as a function of delay between two optical beams as shown in Figure 4.8. **b**, Attosecond streaking spectrogram measured with EUV emission from Ar. Optical driver field intensity (blue line, Figure 4.10a) as retrieved after convergence of PCGPA reconstruction of the experimental spectrogram.

## 4.5 Quantum mechanical modelling of EUV emission in SiO<sub>2</sub>

In this section we review the quantum mechanical model used extensively to describe interaction between light-fields and semiconductors. Interaction of wideband bandgap dielectric materials like SiO<sub>2</sub> with ultrashort laser pulses create electrons and holes in the conduction and valence band respectively. Interaction of these electron-hole, hole-hole and electron-electron pairs is mediated by the laser field induced dipole coupling, this coherent dipole coupling between the carriers generate an interband polarization. Simultaneous to this dipole coupling is the motion of these carriers along the contours of different electronic bands driven by laser pulses which gives rises to intraband current. Figure 4.11 depicts the electron-hole dynamics ensuing SiO<sub>2</sub> interaction with and ultrashort laser pulse. Interband and intraband contributions to HHG in SiO<sub>2</sub> can be numerically evaluated by solving multiband semi-conductor Bloch equations [58][47][60][59] (SBEs) for the retrieved driving laser pulses from attosecond streaking measurements. Electronic band structure calculations were performed by an *ab initio* density functional program package Quantumwise [79]. Three valence ( h = h<sub>1</sub>, h<sub>2</sub>, h<sub>3</sub>) and nine conduction ( e = e<sub>1</sub>, e<sub>2</sub>... e<sub>9</sub>) bands along the  $\Gamma - M$  direction of SiO<sub>2</sub> were considered while numerically solving SBEs, the complex dipole coupling matrix elements ( $\mu_k^{\lambda\lambda'}$ ) between the bands were also calculated by Quantumwise [79].

The temporal evolution of interband polarization ( $[p_k^{he}, p_k^{ee'}, p_k^{hh'}]$ ) is described by the SBE in the following way;

$$i\hbar \frac{\partial}{\partial t} p_k^{he} = (\varepsilon_k^h + \varepsilon_k^e - i\frac{\hbar}{T_2})p_k^{he} - \Omega_k^{eh}(t)(1 - f_k^h - f_k^e) + i|e|\mathcal{E}(t)\nabla_k p_k^{he} + \sum_{\lambda} \left( \Omega_k^{\lambda h} p_k^{\lambda e} - \Omega_k^{e\lambda} p_k^{h\lambda} \right) \quad , \quad (4.1)$$

$$i\hbar \frac{\partial}{\partial t} p_k^{ee'} = (\varepsilon_k^{e'} - \varepsilon_k^e - i\frac{\hbar}{T_2})p_k^{ee'} + \Omega_k^{e'e}(t)(f_k^{e'} - f_k^e) + i|e|\mathcal{E}(t)\nabla_k p_k^{ee'} + \sum_{\lambda} \left( \Omega_k^{\lambda e} p_k^{\lambda e'} - \Omega_k^{e'\lambda} p_k^{e\lambda} \right) \quad , \quad (4.2)$$

$$i\hbar \frac{\partial}{\partial t} p_k^{hh'} = (\varepsilon_k^h - \varepsilon_k^{h'} - i\frac{\hbar}{T_2})p_k^{hh'} + \Omega_k^{h'h}(t)(f_k^h - f_k^{h'}) + i|e|\mathcal{E}(t)\nabla_k p_k^{hh'} + \sum_{\lambda} \left( \Omega_k^{\lambda h} p_k^{\lambda h'} - \Omega_k^{h'\lambda} p_k^{h\lambda} \right) \quad , \quad (4.3)$$

The band occupation ( $f_k^\lambda$ ) is governed by:

$$\hbar \frac{\partial}{\partial t} f_k^h = -2\text{Im} \left[ \sum_{\lambda} \Omega_k^{\lambda h} \left( p_k^{h\lambda} \right)^* \right] + |e|\mathcal{E}(t)\nabla_k f_k^h - \frac{1}{T_1} f_k^h \quad (4.4)$$

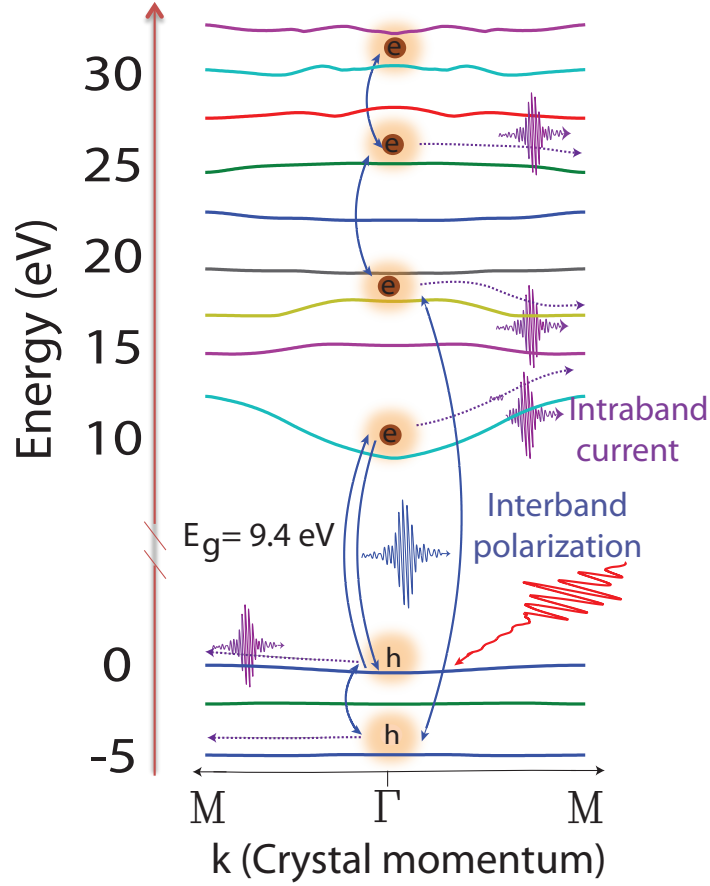


Figure 4.11: Interband Vs Intraband dynamics behind EUV emission from SiO<sub>2</sub>. Multi-level Quantum mechanical model for simulating EUV emission, optical driver pulses couple electrons and holes in the valence and conduction bands which are then driven in opposite directions. Electron-hole motion along the bands gives rise to intraband current whereas the dipole arising out of dynamic excitation-relaxation between the bands during interaction with the field gives rise to interband polarization.

$$\hbar \frac{\partial}{\partial t} f_k^e = -2\text{Im} \left[ \sum_{\lambda} \Omega_k^{e\lambda} (p_k^{\lambda e})^* \right] + |e|\mathcal{E}(t)\nabla_k f_k^e - \frac{1}{T_1} f_k^e \quad (4.5)$$

Here  $\varepsilon_k^e = E_k^e - \sum_{k' \neq k} V_{|k'-k|} f_{k'}^e$ ,  $\varepsilon_k^h = -E_k^h + \sum_{k \neq 0} V_k - \sum_{k' \neq k} V_{|k'-k|} f_{k'}^h$  represents the renormalized dispersion profile of the bands along the k-axis, ( $E_k^{h(e)}$  being the bands as computed by Quantumwise)  $f_k^{h(e)}$  is the time-dependent hole and electron population along

the bands and  $\Omega_k^{\lambda\lambda'}(t) = \mu_k^{\lambda\lambda'} \mathcal{E}(t) + \sum_{k' \neq k} V_{|k'-k|} p_k^{\lambda\lambda'}$  is the renormalized Rabi energy.  $V_q$  is the Fourier transform of the 1D real-space Coulomb potential [80], normalized to match the exciton binding energy [81] in SiO<sub>2</sub> which is close to 1.3 eV. The band index  $\lambda$  references electron and hole bands alike and  $\Omega_k^{\lambda\lambda} = 0 = p_k^{\lambda\lambda}$ . All simulations were performed along the  $\Gamma$ -M direction of the crystal, neglecting the dynamics along other orientations in k-space due to the dominance of this direction in the total emission.

The SBEs as stated above ignore higher order particle correlations such as biexcitons etc. In our model the scattering resulting from such higher order Coulomb interactions and carrier-lattice interaction is approximated by constant dephasing times  $T_2 = 400$  as for the polarization and  $T_1 = 8$  fs for the band occupation numbers. The chosen values are compatible with scattering rates identified in previous studies [82] of SiO<sub>2</sub>. Dephasing times comparable to or shorter than the driver-field period have been previously considered also for semiconductors [83][56]. The accumulated interband polarization is given by;

$$P(t) = \sum_{\lambda, \lambda', k} \mu_k^{\lambda\lambda'} p_k^{\lambda\lambda'}(t) \quad (4.6)$$

the accumulated intraband current from all electronic bands is given by,

$$J(t) = \sum_{h,k} \frac{|e|}{\hbar} (\nabla_k E_k^h) f_k^h(t) + \sum_{e,k} \frac{|e|}{\hbar} (\nabla_k E_k^e) f_k^e(t) \quad (4.7)$$

The total EUV emission spectrum in the near field[84] is given by modulus squared of sum of the Fourier transforms of  $\partial_t P(t)$  and  $J(t)$  ;

$$I_{HHG}(\omega) \propto |i\omega P(\omega) + J(\omega)|^2 \quad (4.8)$$

Time-frequency analysis of inter and intraband currents from SBEs and the semiclassical model were performed with a Gaussian window function of full width half maximum of 0.6 fs, detailed time-frequency analysis of the interband polarization and intraband current are presented later.

#### 4.5.1 Semiclassical model of HHG in SiO<sub>2</sub>

Intraband dynamics of a pre-existing Gaussian electronic wavepacket in the first conduction band of SiO<sub>2</sub> driven by the laser field is considered in the semiclassical model which is governed by the Boltzmann equation [85][61][24];

$$\frac{\partial}{\partial t} f^{\alpha_1}(k, t) = -\frac{e}{\hbar} E(t) \frac{\partial}{\partial k} f^{\alpha_1}(k, t) \quad (4.9)$$

Here scattering process leading to dephasing of intraband current are not taken into account. Intraband electron current accumulated over first Brilluoin zone (BZ) is given by;

$$J(t) = e \int_{BZ} dk (\nabla_k \varepsilon_k^{\alpha_1}) f_k^{\alpha_1} \quad (4.10)$$

Intensity of emission produced by the intraband current is proportional to  $|J(\omega)|^2$ . Intraband current augments with  $\nabla \varepsilon_k^{\alpha 1}(k(t))$ , which implies crests in the intraband current to be synchronized to the maximal change of the curvature of the bands which happens at the peak of the electric field in the laser half-cycles. Maximal EUV emission in both inter and intraband current happens at the peak of the electric field as discussed in the following section.

### 4.5.2 Time resolved simulation of EUV emission

Temporal characteristics of EUV emission can be theoretically studied by performing a time-frequency analysis of the generated interband polarization and intraband currents. Time-frequency analysis of inter and intraband contributions from SBEs and the semiclassical model were performed with a Gaussian window function of full width half maximum of 0.6 fs. Such an analysis helps us to seek additional insights into generation mechanism of EUV emission [86]. Time-frequency analysis of interband polarization evaluated from a multiband SBE simulation predicts a positively chirped emission profile in contrast to virtually chirp free emission from intraband current as is shown in Figure 4.12. The emission from interband polarization in close analogy to the three step model for HH in gases comes from tunnelling of the carriers (electrons and holes), followed by their acceleration and eventually their recombination at the same k-point from where they tunnel ionized [87][52]. So, in the rising edge of a half-cycle, the emission from interband polarization will be positively chirped owing to the fact that if tunnelling to different bands is mediated by the induced dipole,  $\mu \cdot E(t)$  coupling will always maximize at the peak of the rising edge also implying to increase in the cut-off energy. The ultrafast dephasing times used in the SBE equations does not allow the interband polarization to build up during the trailing edge of the half-cycle and we dont observe a dual chirp behaviour in a half-cycle in the emission profile but only a positively chirped behaviour. On the other hand, intraband current is proportional to  $v_c(k)$  which implies that the emission will maximize around the  $\Gamma$  point in the BZ where change in the curvature of the band is maximal. From the Boltzmann transport equation the carriers wavepacket crosses the  $\Gamma$  point at peak of the field, hence the emission from intraband current will maximize with the peak of the field around the  $\Gamma$  point i.e. the emission profile will be symmetric around peak of the field with its vertex synchronized to peak of the half-cycle as presented in Figure 4.12. Also, the positively chirped emission from interband dynamics will be asynchronous to the peak of the half-cycle.

## 4.6 Interband Vs. Intraband dominated dynamics in $\text{SiO}_2$

In the previous sections we have set the stage for a meticulous modelling of EUV emission and at the same time have performed a systematic analysis of effects of measurement set-up which can counterfeit experimental results (see Appendix C). Considering all such effects

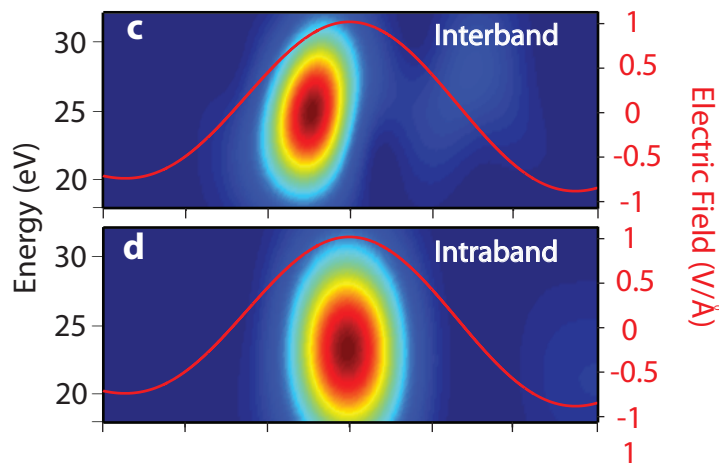


Figure 4.12: Time-frequency analysis spectrograms for the **a**, interband polarization and **b**, intraband currents obtained from a multiband SBE calculation.

we have now confidence in looking into physical signatures present in our measurement which can help us decipher the mechanism of EUV emission in SiO<sub>2</sub>.

Spectrum produced by interband and intraband contributions in SBE simulation [59][60] with optical driver used in the experiment (Figure 4.2c) is displayed in Figure 4.13. The strength of Coulomb interaction[80] among the carriers in the SBEs was set to match the exciton binding energy[80] ( $\sim 1.5$  eV) in SiO<sub>2</sub>. Intraband contribution dominates over that of interband contribution in the overall emission by more than three orders of magnitude as shown in Figure 4.13. Spectral dominance of one mechanism over the other in simulations doesn't necessarily give a transparent answer to which of the physical mechanisms really dominate the HH emission. Hence we look into time-domain analysis to resolve this physical mechanism as is also suggested in the work by Wu et al. [86]. Emission time or the group delay of the main attosecond burst evaluated by filtering the satellites in Figure 4.2 is shown in Figure 4.14 for experimental EUV field from SiO<sub>2</sub>. Similar treatment is done for the dipoles in the inter, intraband and total emission in the numerical solution of SBE evaluated for electric field driving the SiO<sub>2</sub> sample as is shown in Figure 4.2c. Gradual increase in the emission time as a function of photon energy is apparent for interband contribution implies positively chirped EUV emission, which is alike the emission time behaviour measured for EUV generated by Ar in the similar energy region Figure 4.3. The positively chirped emission is known to come from short trajectories in gases [32]. Spectrally flat response of the experimental EUV field and the dipole from intraband contribution as well as the one from semiclassical model resemble closely. Considering that emission from intraband contribution dominates over interband by nearly three orders of magnitude (Figure 4.13), the emission time in the total emission will indeed resemble that of intraband contribution. EUV photons generated by intraband electron-hole motion lead to spectrally flat emission time, which implies to their concurrent generation. Directly

58

contrasting the emission time (group delay) response of inter and intraband dynamics with emission time of experimental attosecond pulse transparently corroborates to EUV emission being dominated by intraband dynamics as is presented in Figure 4.14.

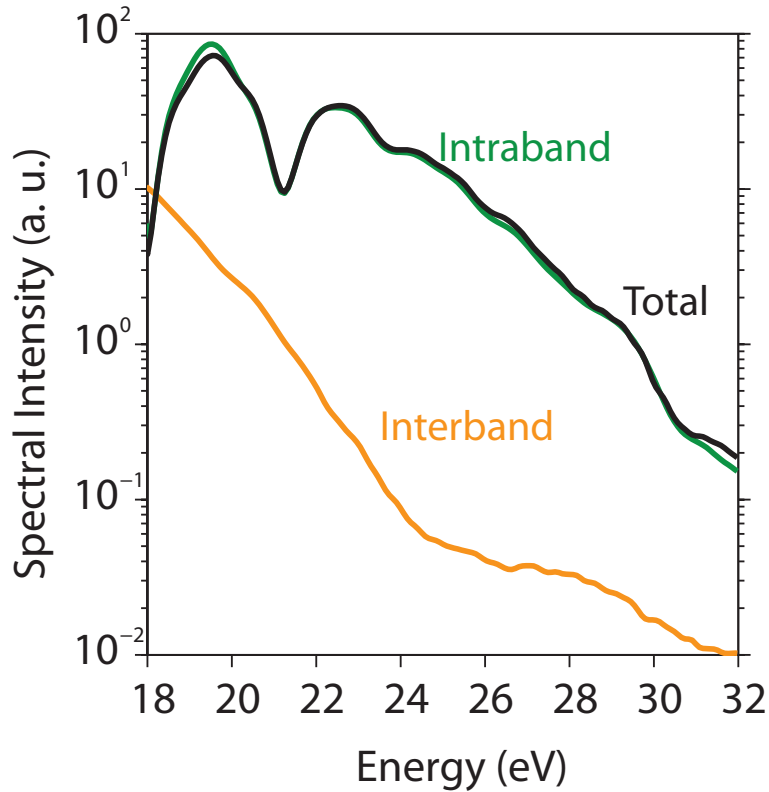


Figure 4.13: EUV spectra simulated for the interband polarization and intraband current for the optical field represented in Figure 4.2.

The group delay of an attosecond pulse from SiO<sub>2</sub> as shown in Figure 4.14 is obtained by taking into account the spectral phase from measurement set-up (150nm Al foil and Au mirror) on the experimentally measured attosecond pulse. Comparison of group delay of EUV emission from SiO<sub>2</sub> with and without considering spectral phase from measurement set-up is shown in Figure C.3 in Appendix C.

Error analysis of experimentally retrieved group delay of isolated attosecond pulses from SiO<sub>2</sub> and Ar was possible from PCGPA; the reconstructed spectrogram after convergence of PCGPA contains as many EUV pulses ( $P(t)$ , see Appendix D) as the number of delay points [10] in the spectrogram. A detailed discussion on working of PCGPA is presented in Appendix D. The group delay is retrieved from each such pulse and it allows us to put an error bar on the experimentally retrieved group delays.

Time frequency analysis of experimentally measured attosecond pulse and the dipoles obtained from inter and intraband contributions to numerical solution of SBEs with electric field of optical pulse shown in Figure 4.2c was performed and is presented in Figure

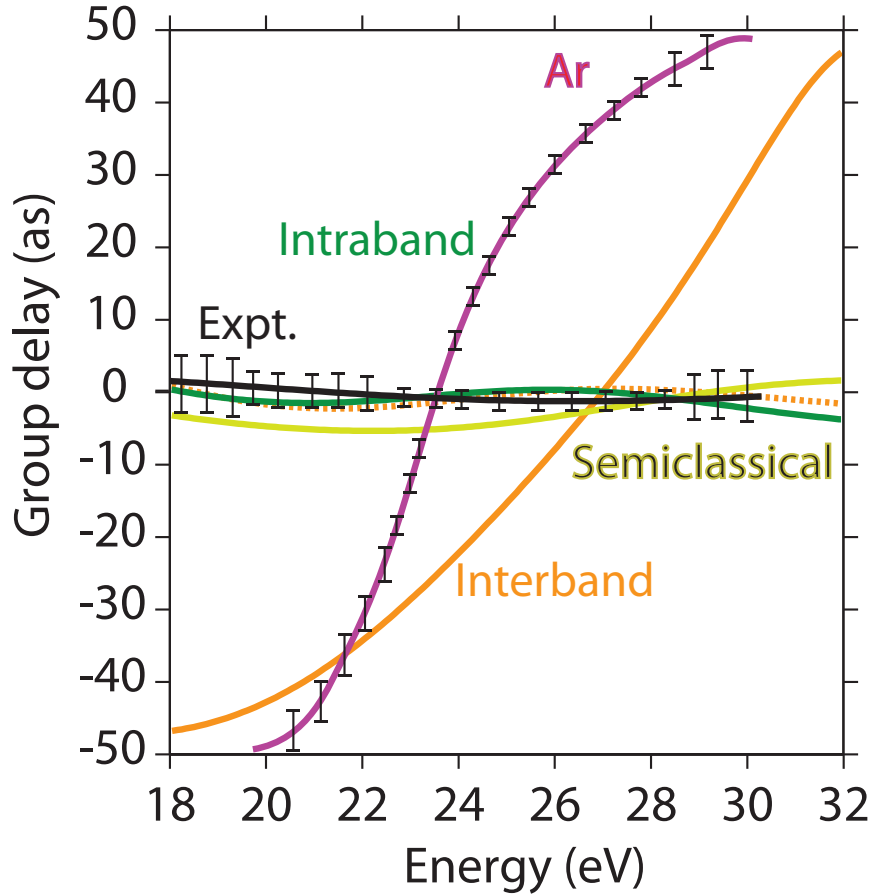


Figure 4.14: Experimentally retrieved group delays (emission times) of a single attosecond burst from SiO<sub>2</sub> (black line) and a single attosecond burst from Ar gas (violet line) in addition to the theoretical values for the interband polarization (orange line), the intraband current (green line), total polarization (orange dashed curve) and the semiclassical model (yellow line).

4.15. Time-frequency spectrogram of experimentally measured EUV field is shown in Figure 4.15a, the EUV emission is both synchronised to peak of the driving electric field as well as is chirp free. Positively chirped EUV emission can be seen from time-frequency spectrogram of interband contribution in Figure 4.15b. Chirp free EUV emission can be envisaged from practically vertical nature of the spectrogram along the time axis from intraband contribution and the total emission in Figure 4.15c and Figure 4.15d respectively. Figure 4.15e shows the spectrogram as evaluated from semiclassical model which considers intraband motion of electrons in the conduction band to give rise to EUV emission. Chirp free emission measured in the experiments is in compliance with the intraband motion of electrons. Also shown in each time-frequency spectrogram is the half-cycle of the driving electric field generating EUV emission on top of it. As can be seen, maximal emission in the

4. Real-time tracing and attosecond control of multi-PHz electric currents in solids

experimental EUV pulse and the ones obtained from intraband contribution in SBEs and semiclassical model are synchronous to the vertex of the driving field which is in contrast to simulated asynchronous emission in case of interband dynamics.

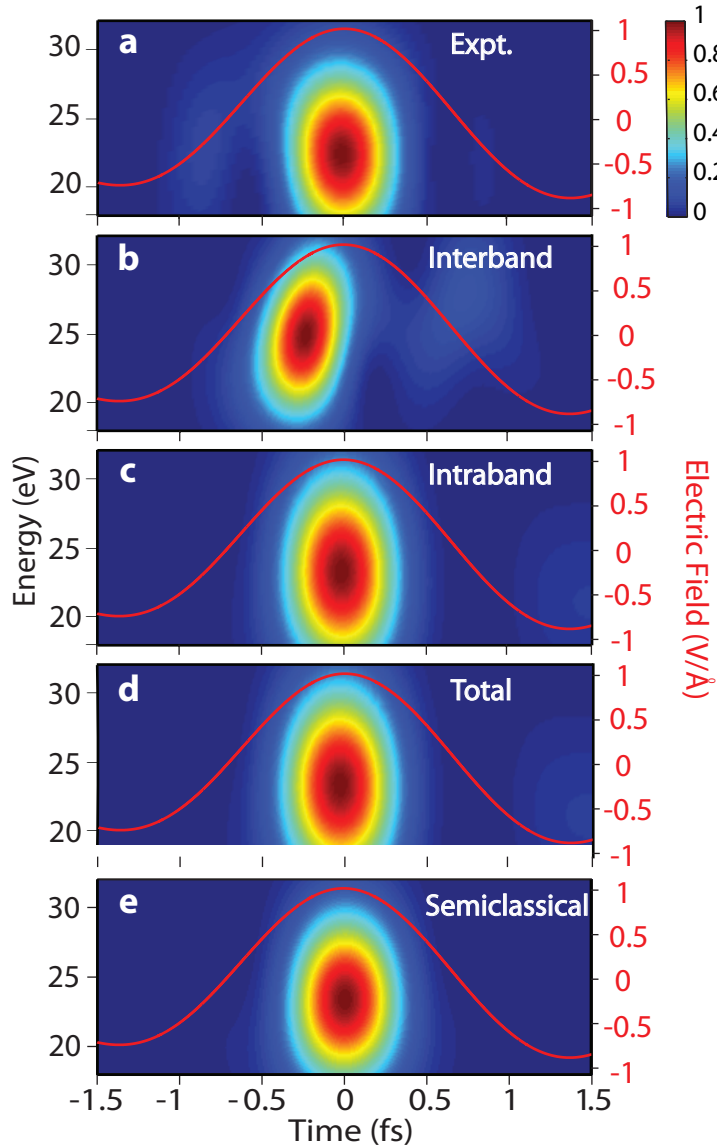


Figure 4.15: Time-frequency spectrograms obtained by the experimentally measured EUV attosecond pulse **a**, interband polarization **b**, intraband current **c**, and total emission **d** respectively as simulated by SBEs. **e**, Time frequency spectrogram of intraband current obtained in the semiclassical model, red curve over the spectrograms is the driving electric field. Positively chirped emission from interband contribution can be envisaged by the tilt along the time axis, emission from intraband motion of electrons is chirp free. EUV attosecond bursts clocks in every half-cycle of the driver laser waveform.

### 4.6.1 Effect of driving laser intensity on chirp of EUV emission

Temporal characteristics of EUV emission were also studied for different field strengths of optical driver pulse. Interband dominated EUV emission arising from re-collision of electron-hole pair trajectories is expected to be sensitive to field strength, as the trajectories and their corresponding re-collision times (field-induced tunnelling times will change) will change with field strength of driver field. Whereas intraband dominated emission arising from scattering of electrons in the electronic bands is expected to be less sensitive to strength of optical driver. Experiments and corresponding simulations performed at different field strengths of the optical driver pulse further verify the above conclusions. Figure 4.16 shows group delay (emission times) calculated for three different intensities of the single-cycle driving laser pulse. The chirp associated with interband (Figure 4.16a) contribution exhibits a well discernible intensity dependence on the field strength. By contrast the chirp associated with the intraband current contribution (Figure 4.16b) undergoes minimal changes. Experiments performed with the same driving field waveforms as those in our calculation and at the same intensity settings show a remarkable agreement with the chirp dynamics and their intensity dependence with those of the intraband current.

### 4.6.2 Effect of strength of Coulomb interaction on emission strength of the two mechanisms and their temporal characteristics

Coulomb interaction among the carriers renormalizes the energy bands as well as Rabi frequencies of interband transitions in SBE simulations and can significantly affect the response of the system. Increasing strength of Coulomb interaction (marked via the increasing ground state energy of the exciton) yields an ever increasing ratio of the spectral intensities between intra and interband contribution (Figure 4.17a-c). For an exciton binding energy [81] that matches with that in SiO<sub>2</sub> ( $E_{exciton} \sim 1.3$  eV) the ratio between intra and interband contribution is more than two orders of magnitude. As a result the total emission practically coincides with that of the intraband contribution. An equally important outcome of this study is that despite these significant changes in the spectral response of the system, inter and intraband dynamics maintain their chirp signatures as shown in Figure 4.17d-f. Interband chirp is nevertheless slightly affected as the Coulomb interaction renormalizes the Rabi frequency and the interband polarization is sensitive to this variation. Owing to the dominance of intraband current over interband polarization by several orders of magnitude, its temporal emission characteristics (chirp) dominate the overall response of the system.

### 4.6.3 Effect of sample crystallinity on mechanism of EUV generation

In order to overcome the ambiguity of a plausible different mechanism in purely crystalline sample compared to a polycrystalline nanofilm as presented above, we have performed attosecond streaking measurements with a purely crystalline SiO<sub>2</sub> samples i.e. Quartz

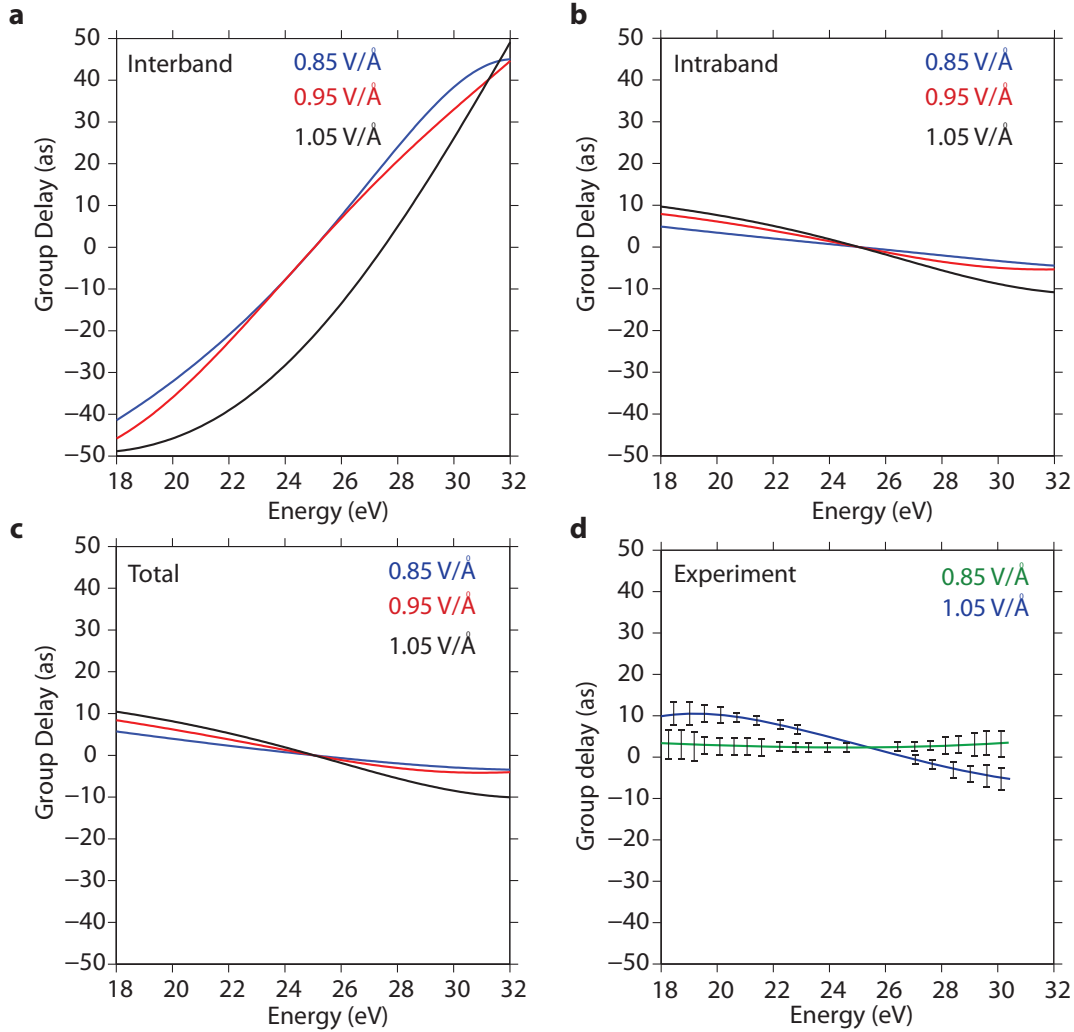


Figure 4.16: Computed group delay variation for three different field strengths of a single-cycle driver for interband contribution **a**, intraband current contribution **b** and total polarization **c**. **d**, experimentally measured group delay variation for two different intensities of a single-cycle driving pulse.

which were cut along the z-axis and for the thinnest samples commercially available  $\sim 5 \mu\text{m}$  compared to only  $\sim 125 \text{ nm}$  thickness of polycrystalline  $\text{SiO}_2$  used in all the experiments. A z-cut Quartz sample has the hexagonal plane of  $\Gamma$ -M and  $\Gamma$ -K directions of the Brillouin zone along the lateral direction of the sample, so in our experiment the Quartz sample was mounted on a rotating stage for aligning the direction of the polarization of electric field of laser pulse with the  $\Gamma$ -M direction of the dispersion profile of the sample so as to maximise the EUV emission from sample. EUV emission from Quartz profoundly depends on its orientation with respect to the laser polarization axis, significant emission in the EUV spectral range comes only from the  $\Gamma$ -M direction of the crystal compared to  $\Gamma$ -

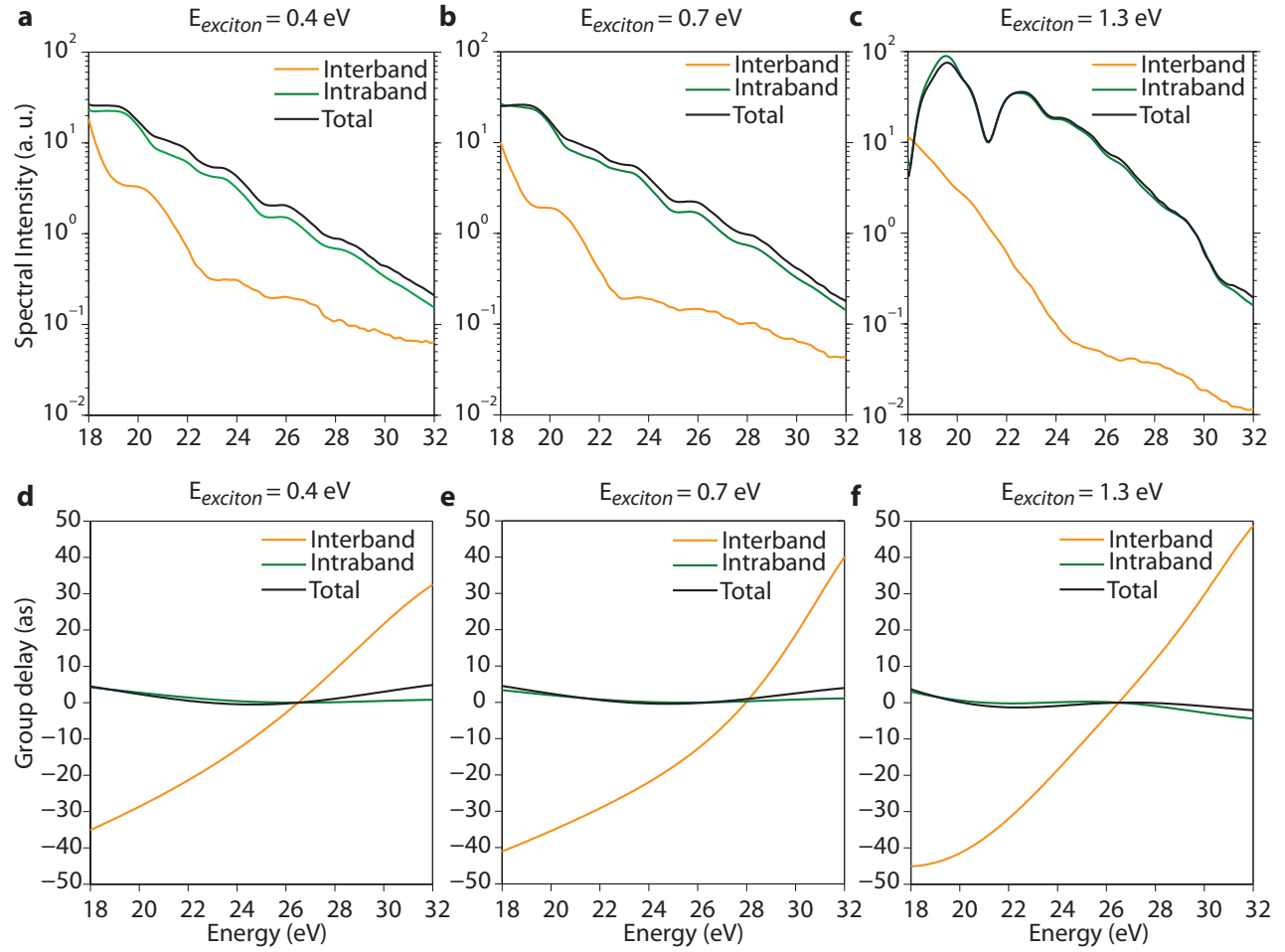


Figure 4.17: **a-c**, Influence of strength of Coulomb interaction among the carriers in SiO<sub>2</sub> on spectral intensity of emission from inter and intraband dynamics for three different exciton binding energies. **d-f**, Computed group delay variation for three different exciton binding energies for inter, intraband and total polarization.

K direction where the emission is marginal (less than an order of magnitude compared to  $\Gamma$ -M direction) as presented in Figure 4.18, semiclassical simulations comparing EUV emission from different directions of the Brillouin zone is shown in Figure 3.4 which is in conformity with measurements. Measurements with the crystalline samples chartered support in favour of intraband dynamics of carriers driven by optical fields as being the sole mechanism behind EUV generation mechanism in SiO<sub>2</sub> irrespective of the crystallinity of the sample. Figure 4.19 shows the attosecond streaking measurement performed with EUV emission from crystalline quartz sample. Spectrally flat response of group delay of the experimental EUV field in Figure 4.19c clearly shows that the dynamics underlying EUV generation even in crystalline samples is still dominated by intraband dynamics.

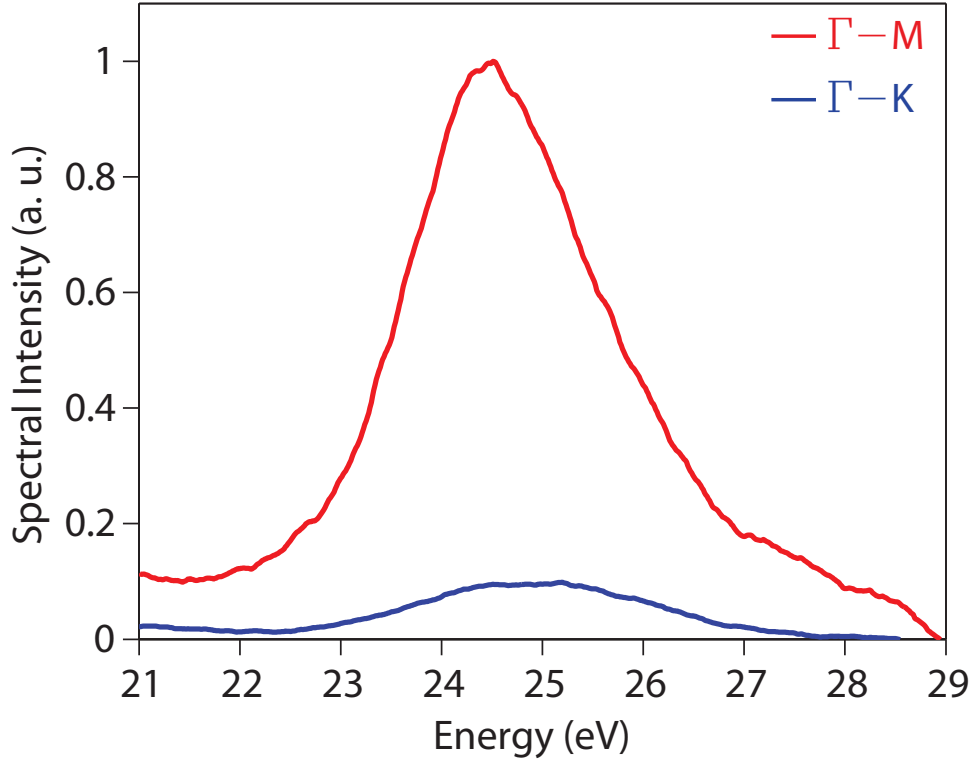


Figure 4.18: Measured EUV spectra arising from two different orientations of Quartz ( $\Gamma$ -M and  $\Gamma$ -K) with their axes being aligned to polarization axis of the driving laser pulse.

## 4.7 Probing nonlinearity in EUV emission, steering intraband currents in SiO<sub>2</sub>

Field control over temporal structure of EUV emission has remained a benchmark in gas phase attosecond physics [64], where a few cycle driver pulse with carrier envelope phase (CEP) of 0 rad gives an isolated attosecond pulse and a driver pulse with  $\Phi_{CEP} = \frac{\pi}{2}$  rad gives a dual burst of attosecond pulses. EUV emission from SiO<sub>2</sub> has been shown to be less nonlinear and the spectral changes on change of CEP for few cycle and one and half cycle driver pulses are negligible [23]. Spectral changes with change in CEP are significant only for single cycle and an optical attosecond pulse driver. In this work seeking further evidence on mechanism dominating EUV emission, we have performed temporal characterization of multi PHz currents inside SiO<sub>2</sub> driven by two different CEPs of a single cycle pulse as shown in Figure 4.20a ( $\Phi_{CEP} = 0$  rad) and Figure 4.20b ( $\Phi_{CEP} = \frac{\pi}{2}$  rad), electric field of the driver waveform as retrieved by PCGPA is plotted on top of the spectrograms. The retrieved EUV field from the spectrograms is shown in Figure 4.21a and Figure 4.21b. The prominent differences in the features of EUV fields generated by  $\Phi_{CEP} = 0$  rad waveforms are shown with black arrows which are absent for the  $\Phi_{CEP} = \frac{\pi}{2}$  rad driver waveform (Figure 4.21b). A  $\Phi_{CEP} = \frac{\pi}{2}$  rad driver waveform generates a more continuum structure

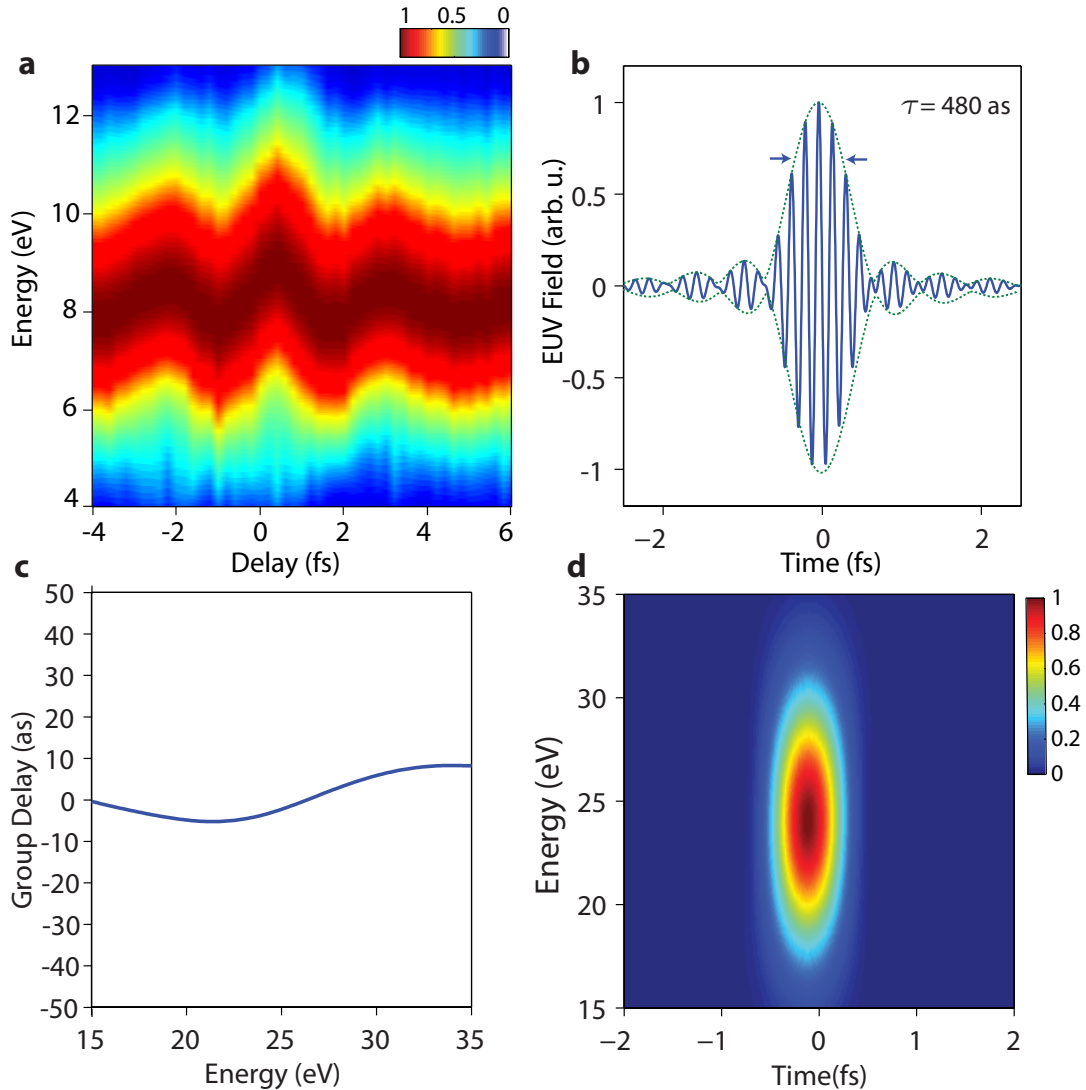


Figure 4.19: **a**, Attosecond streaking measurement with EUV pulses generated in Quartz (thickness  $\sim 5 \mu\text{m}$ ) **b**, Retrieved isolated attosecond pulse after the convergence of PCGPA. **c**, Retrieved group delay (emission time) of the single EUV attosecond burst. **d**, Time-frequency spectrogram of the retrieved attosecond pulse.

in the EUV emission than a  $\Phi_{CEP} = 0$  rad driver waveform hence resulting into a shorter EUV pulse as well.

Interband contribution to the total polarization predicts dual attosecond pulse generation for  $\Phi_{CEP} = \frac{\pi}{2}$  rad driver waveform compared to a  $\Phi_{CEP} = 0$  rad waveform as shown in the intensity profiles of the interband dipoles in Figure 4.21c and Figure 4.21d. In contrast to interband contribution, intraband contribution is predicted to give isolated attosecond pulses (Figure 4.21c and Figure 4.21d) for both the driver waveforms, in conformity with

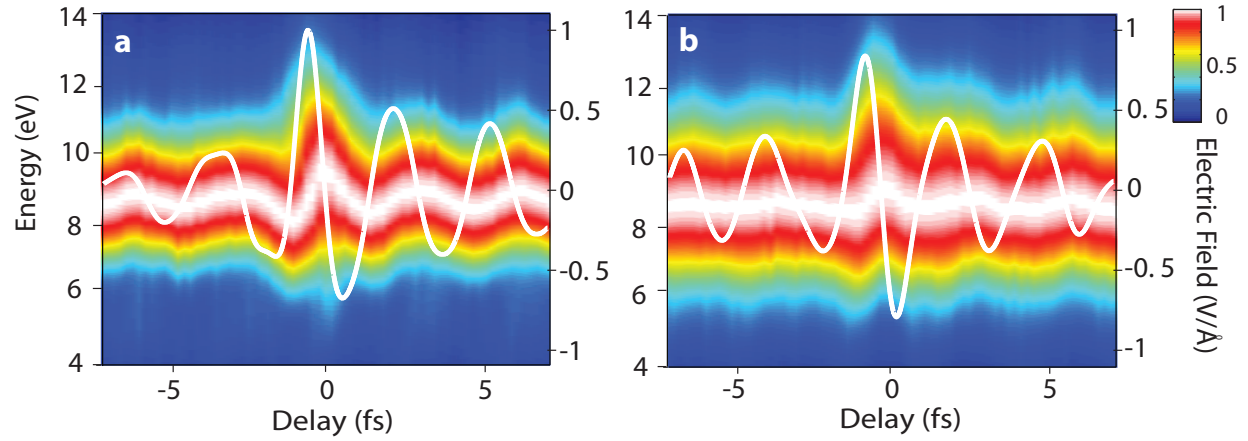


Figure 4.20: **a, b**, Attosecond streaking spectrograms recorded for two CEP settings of the single-cycle driver waveform (white lines on top of spectrograms), differing by  $\pi/2$  rad.

our experimentally measured EUV fields. Dual attosecond bursts are also predicted for a single cycle driver with  $\frac{\pi}{2}$  rad  $\Phi_{CEP}$  when EUV emission is simulated by interstate transitions among Wannier-Stark states (equivalent to interband transitions) formed by quasi static electric fields during the course of interaction of driver waveform with a dielectric [49]. The results presented from this experiment further strengthen our claim over intraband dominated dynamics behind EUV emission in  $\text{SiO}_2$ . Features emphasized with black arrows on EUV field measured with  $\Phi_{CEP} = 0$  rad waveform are captured well with the intraband contribution to the dipole. A comparison of the experimental intensity profiles of EUV bursts for both CEPs with the ones simulated for inter and intraband contributions in SBEs clearly demonstrate the close agreement between experiment and intraband dominated dynamics in  $\text{SiO}_2$ .

This significant difference in EUV emission dipoles from inter and intraband contributions is attributed to vastly different nonlinearity pertinent to their generation mechanism. The interband polarization, as in the case of gas-phase HH dynamics, draws its nonlinearity both from the exponential dependence of the excitation step occurring near the peak of the field crest and from the ensuing waveform-sensitive electron trajectories [87], which successfully lead to the recombination of electrons and holes giving emission at discrete times [52][87]. Emerging from the scattering of electrons on the periodic potential of the medium and giving rise to wideband radiation at each moment of time, the intraband current is associated with a distinctly different nonlinearity to the field waveform, which is described by a Bessel-type field scaling of the emitted intensity versus the applied field strength and is sensitive to the HH order and the spatial frequencies of the periodic potential [65][23].

Selection of optical driver to perform such a measurement where we seek to identify non-linearity in the generation process plays an important role. None of the two driver waveforms shown in Figure 4.20a and Figure 4.20b is 'purely cosine' or 'purely sine' respec-

## 4.7 Probing nonlinearity in EUV emission, steering intraband currents in SiO<sub>2</sub>

tively. The contrast of the field strength in two consecutive half-cycles in Figure 4.20a is 1.6 to 1, sufficiently high but not a 'cosine pulse'. Similarly the contrast in field strengths (for two dominant half-cycles) in Figure 4.20b is close to 1.16 to 1, sufficiently low but not a 'near sine' waveform. A perfect 'sine pulse' would give dual burst of EUV pulse both for inter and intraband contribution which is indeed no surprise and is also confirmed by previous time-integrated studies [23]. Previous studies have demonstrated  $\sim E^{18}$  scaling of the EUV emission intensity with field strength for EUV photon energy close to 23 eV which is the central energy of the EUV bursts in our experiment. This suggests that in our measurements the intensity ratio between the main and the satellite pulse must be approximately three orders of magnitude for the near-cosine waveform and more than an order of magnitude for the near-sine waveform. Thus a satellite pulse shall be virtually absent in our experiment for both the CEP settings of the driver waveform, which is indeed the case.

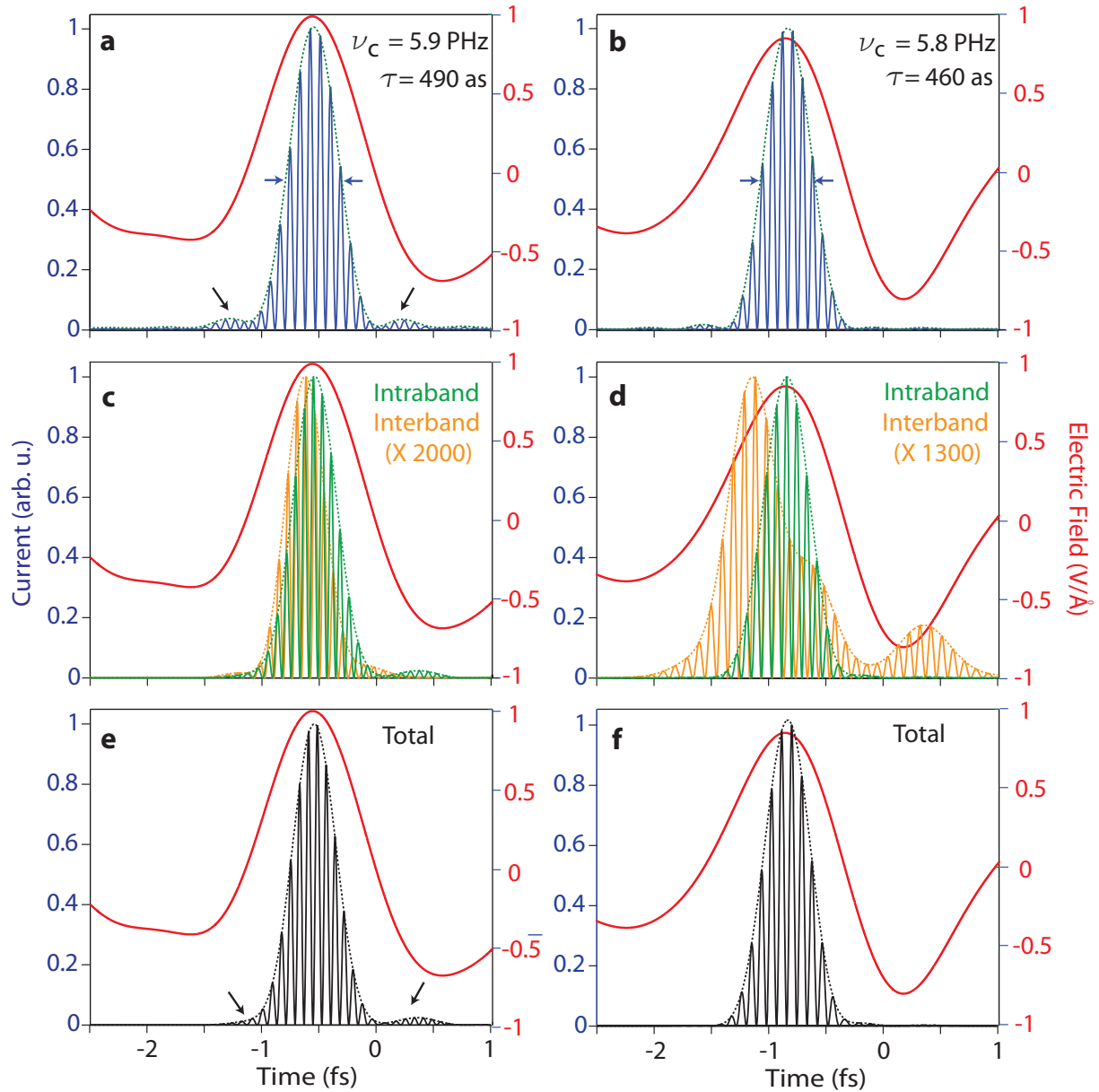


Figure 4.21: **a, b**, EUV transients retrieved from the spectrograms shown in Figure 4.21a and Figure 4.21b respectively. **c, d**, Intensity profiles of EUV bursts calculated from the intraband contribution (green curve) in the quantum mechanical SBEs using the experimentally traced waveforms of the driving optical field (red lines). The generation of isolated current bursts synchronized to the peak of optical driving pulse (red line) due to the intraband motion of electrons is predicted for both CEP settings of the synthesized single-cycle driver waveforms, in agreement with our experiments **a, b**. Interband simulations (orange curve) predict that varying the CEP will result in a transition from an isolated to a twin attosecond burst and a temporal offset with respect to the field crests. **e, f**, Total polarization dynamics simulated for the two different waveforms. Discrete temporal features present in EUV transients in case of  $\Phi_{CEP} = 0$  rad driving waveform are highlighted with black arrows in **a** and **e**.

## 4.7 Probing nonlinearity in EUV emission, steering intraband currents in Si

The formation of pedestal features (marked with black arrows) present in the near-cosine waveform (Figure 4.21a) but not in the near-sine (Figure 4.21a) one are compatible with the CEP-induced spectral shaping of the EUV pulses. EUV spectra generated for the two driver waveforms ('near cosine' and 'near sine') in presence of high-pass spectral filter of our experiments are shown in Figure 4.22a. The spectral shaping of the EUV spectra in Figure 4.22a has prominent differences. This spectral shaping allows the control of the both duration and frequency of the intraband currents bursts (Figure 4.21a, Figure 4.21b). EUV spectra simulated for intra, interband and total emission in SBEs with high-pass spectral filter of experiments being applied on them is shown in Figure 4.22b-c respectively. Theoretical modelling of only intraband dominated dynamics predict spectral shaping on EUV bursts by the two different CEPs as experimentally observed. On the other hand interband dynamics predicts formation of much more a structured spectrum when the driver waveform is changed by  $\Phi_{CEP} = \pi/2$  rad.

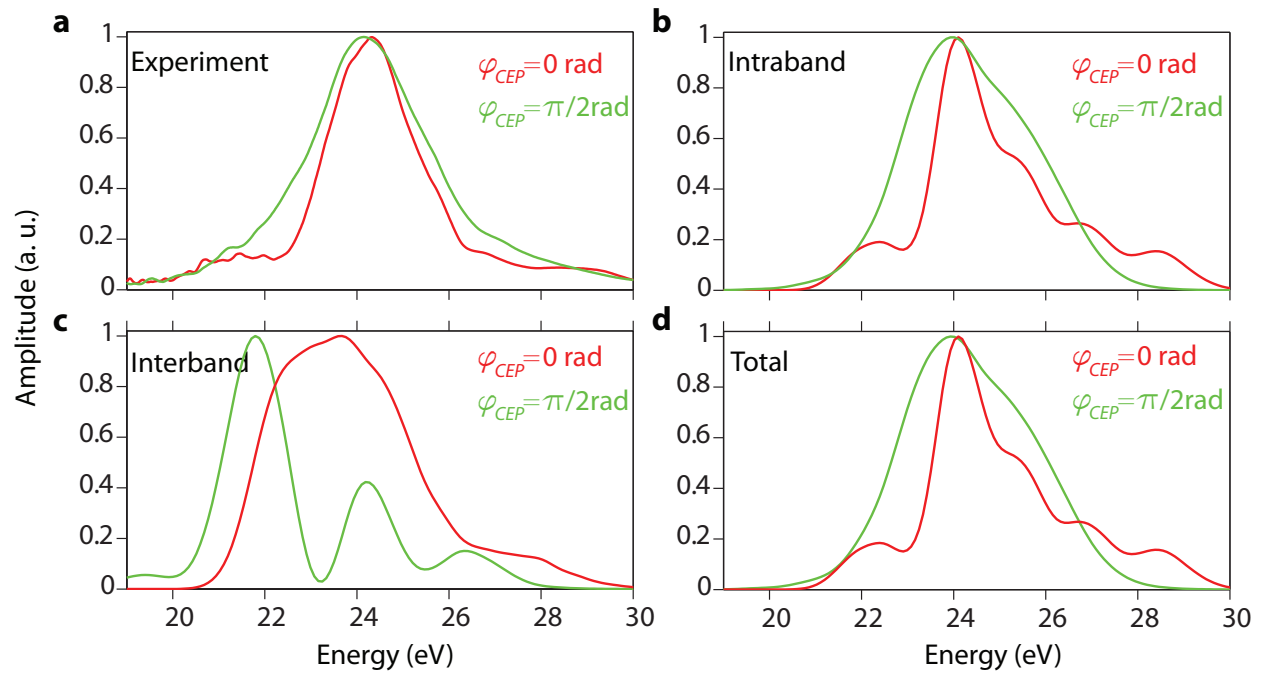


Figure 4.22: **a**, Measured EUV spectra generated by the near-cosine and a near-sine single-cycle driving laser pulses of our experiments (see Figure 4.20). **b**, **c** and **d** simulated EUV spectra from the same driving field waveforms for intraband current, interband polarization and total polarization respectively.

## 4.8 Controlling the frequency, duration, and structure of intraband currents and attosecond EUV bursts in SiO<sub>2</sub>

Curtailling the bandwidth of the optical driver simply by blocking one of the constituent bands in the light-field-synthesizer [36][57] used to generate the single-cycle driver of Figure 4.2, we generate a  $\sim 1.5$  cycle driver pulse at slightly lower ( $\sim 0.7V/\text{\AA}$ ) peak field. The attosecond streaking spectrogram measured with the EUV burst generated in SiO<sub>2</sub> with these pulses is shown in Figure 4.23, Figure 4.23b shows the retrieved EUV burst in this case. The lower cut-off energy which is a consequence of the weaker driving field, gives rise to an EUV burst with a carrier frequency of approximately  $\sim 1$  PHz lower than compared to that presented in the experiments in the above sections. A comparison of the spectra produced by single-cycle and 1.5 cycles optical driver is made in Figure 4.24. Increase of the EUV pulse duration to nearly 750 as and the formation of weak but discernible satellites synchronized with the peak of half cycles of the driver (black arrows, Figure 4.23b) is observed. Once again, the precise synchrony of the weak satellites of emitted EUV burst with half-cycle of the 1.5 cycle driver further corroborates our argument of intraband dominated dynamics in SiO<sub>2</sub>. All of these measurements demonstrate the capability of manipulating the time-dynamics of electric currents in solids with an unprecedented resolution. For a nonlinear medium thinner than the wavelength of the driving field, the induced intraband current  $J(t)$  and emitted field  $E_{EUV}(t)$  are related as:  $E_{EUV}(t) \sim J(t)$ . As a result the reconstructed EUV transients presented in Figures 4.23, 4.21 as well as those recorded using a 1.5-cycle driver created in the light-field synthesizer directly represent current dynamics in the medium and serve here as the first demonstration of the use of light fields to generate, measure, confine (at the attosecond level) and tune the waveforms of multi-PHz currents in solids.

## 4.9 Spatial dynamics of electrons

Gratifying agreement between time-domain analysis of experimental EUV fields with those simulated for intraband currents from semiclassical and quantum-mechanical SBE modelling allows us to discreetly model the spatial excursion of electrons in reciprocal space. Unfortunately as discussed above in section 4.6 all emission of EUV from intraband model happens concurrently and at  $\Gamma$  point of the dispersion profile of the bands, so in order to learn more about the spatial dynamics of electrons we have performed simulations in the real space using Boltzmann equations considering motion of electrons only in the first conduction band of SiO<sub>2</sub> as being the sole source of EUV emission. For a co-sinusoidal band,

$$E(k) = \frac{\Delta}{2} - \frac{\Delta}{2} \cos(kd) \quad (4.11)$$

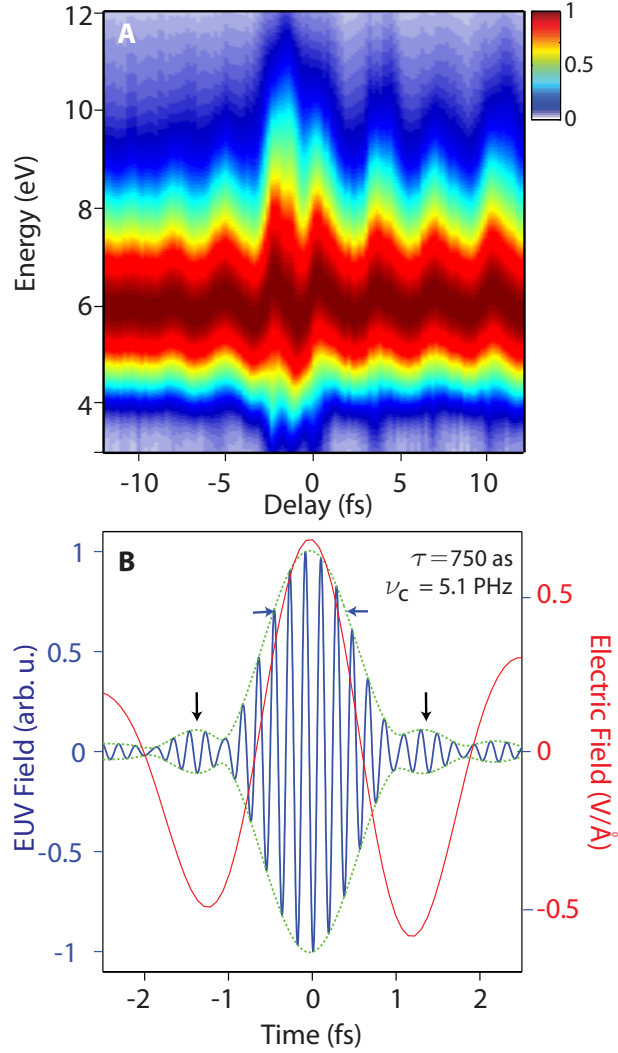


Figure 4.23: **a**, Attosecond streaking spectrogram measured with EUV pulses generated by a  $\sim 1.5$  cycle long optical driver waveform. **b**, Retrieved attosecond pulse after the convergence of PCGPA. Black arrows mark the formation of weak satellite bursts.

group velocity is given by,

$$v_R = \frac{1}{\hbar} \frac{\partial E}{\partial k} = \frac{d\Delta}{2\hbar} \sin(kd) \quad (4.12)$$

Real space motion of electron in this kind of band is given by,

$$z(t) = \int v_R dt \quad (4.13)$$

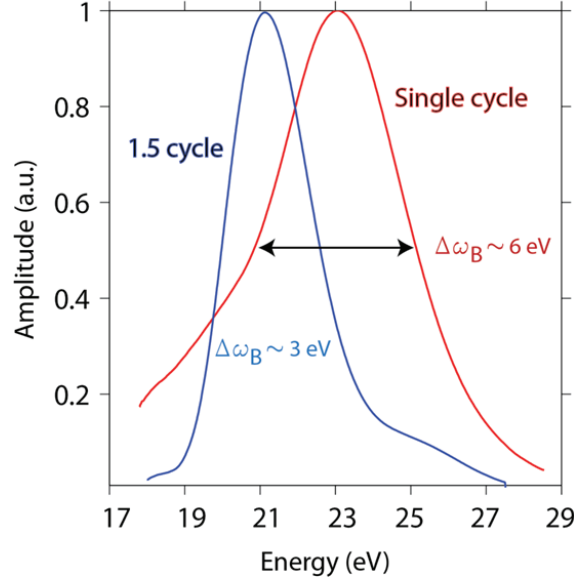


Figure 4.24: Retrieved EUV spectrum from attosecond streaking measurements performed with a single cycle driver (red curve) and a one and half cycle driver pulses in SiO<sub>2</sub>.

Assuming a DC field acting on the system,

$$z(t) = \frac{\Delta}{2} \frac{1}{eE} \cos\left(\frac{eEt d}{\hbar}\right) \quad (4.14)$$

Defining the Bloch frequency [88] as  $\omega_B = \frac{eEd}{\hbar}$ . Its clear that in presence of static electric field electrons perform Bloch oscillations with a frequency proportional to strength of the field [88]. Maximal spatial excursion of the electrons or the localization length of electrons is  $\frac{\Delta}{eE}$  which connotes to strong localization of electrons at stronger electric fields, also the localization length is proportional to width of the band which is the same as magnitude of overlap of Wannier functions between two neighbouring sites. Now we turn to experimental situation of a non-cosinusoidal first conduction band of SiO<sub>2</sub> and dynamic electric field as in Figure 4.2. Decomposition of first conduction band of SiO<sub>2</sub> into partial co-sinusoidal bands is give by;

$$E_c(k) = 5.15 + 0.3239\cos(kd) - 0.0049\cos(2kd) + 0.0019\cos(3ktd) + 0.0031\cos(4kd) \\ + 0.0051\cos(5kd) - 0.0010\cos(6kd) \quad (4.15)$$

Figure 4.25 shows evolution of  $z(t)$  under the electric field profile of the laser pulse, electron follows the electric field of optical driver during its rising and trailing edges; however for the stronger part of the electric field,  $z(t)$  tends to localise. Second derivative of  $z(t)$  with respect to time gives acceleration of the charges whose Fourier transform produces the EUV spectrum. Maximal excursion of electrons is  $2.5\text{\AA}$  as estimated by

$\frac{\Delta}{eE_{\max}}$  where width of the band  $\Delta$  is  $\sim 2.5\text{eV}$  and peak field strength is  $1\text{V}/\text{\AA}$ . Fourier filtering  $z(t)$  in the part of the bandwidth experimentally measured for EUV pulses (18 - 30 eV) shows that at the moment of EUV emission the electrons make ultrafast oscillations on a very small spatial dimension as shown in Figure 4.25. The extremely small spatial excursion of electrons ( $< 0.1 \text{\AA}$ ) while emitting EUV radiation promptly reminds us of spatial resolution offered by EUV spectroscopy in solids as discussed in chapter 3. Spatial excursion of electrons can also be meticulously modelled by solving real space TDSE (time dependent Schroedinger equation) and the phenomenon of Bloch oscillations and localization are extensively studied in the literature [89]. Experimental efforts towards observing electron motion in real time along the dispersion profile of  $\text{SiO}_2$  while it is leading to EUV emission are currently underway.

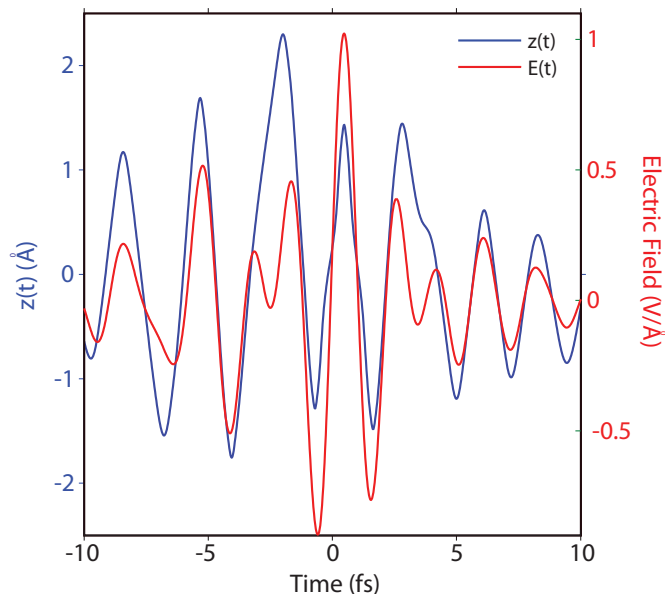


Figure 4.25: **Spatial excursion of electrons.** One dimensional trajectory of electrons,  $z(t)$  in presence of a pulsed electric field (red line) assuming intraband motion of electrons in the first conduction band of  $\text{SiO}_2$ .

## 4.10 Nonlinear current density and dynamic conductivity

EUV emission at PHz frequencies from  $\text{SiO}_2$  undeniably implies to electron oscillations inside the bulk of  $\text{SiO}_2$  at such high frequencies. Having established that EUV emission in  $\text{SiO}_2$  comes from intraband dynamics of optically excited carriers in the electronic bands of  $\text{SiO}_2$  which is of the same nature as electronic motion in the conduction bands of Si

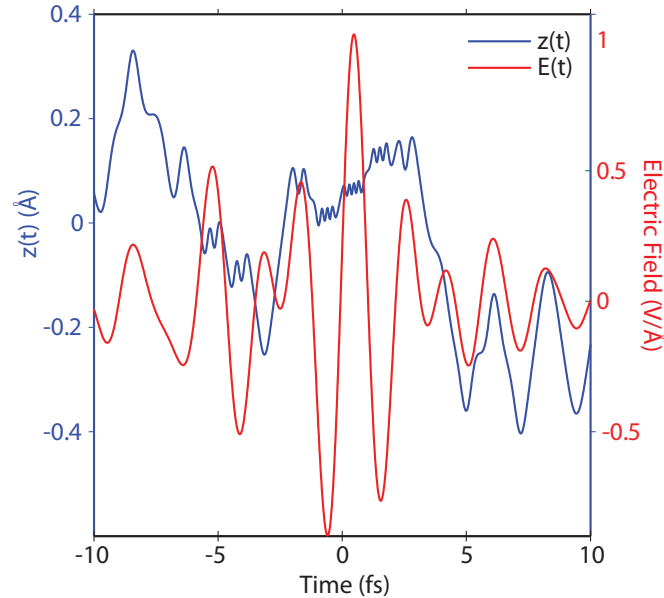


Figure 4.26: Trajectory of electrons,  $z(t)$  which contribute to EUV emission in 18-30 eV spectral-range in presence of a pulsed electric field (red line) assuming intraband motion of electrons in the first conduction band of  $\text{SiO}_2$ .

in modern electronics [90], one can easily foresee this to be associated with future light-based electronics operating at multi PHz frequencies. Speed of electronics is adjudged by the capability of how fast we can turn on and off electric currents in diodes [91], unfortunately ever increasing speed is restricted by scattering of electrons with the lattice which eventually leads to thermal effects of over-heating thereby restricting the speed of electronics which can be achieved. It is also to be duly noted that conventional electronics uses incoherent electrons to drive currents in the circuits as the dephasing time of electrons in the lattice cannot be defeated by switching time of the voltage driving them. However, driving electrons with ultrafast Laser fields as demonstrated in this work easily overcomes this barrier and the electronic motion remains coherent till the duration of the pulse. So advancement of electronic metrology presented in this thesis into the multi-PHz of measuring multi-PHz currents inside a dielectric medium opens up new avenues of realising coherent-electronics (light-driven) operating at multi PHz frequencies in the future.

Herein we attempt to quantitatively estimate electronic properties of  $\text{SiO}_2$  which help us to make a comparison of its efficacy with modern electronics. We have first measured photon yield of the emitted EUV radiation from  $\text{SiO}_2$  sample which in turn allowed us to evaluate the amplitude of  $E_{EUV}(t)$  in the bulk of  $\text{SiO}_2$  as well as the nonlinear current density inside our sample. The energy of EUV pulses generated in  $\text{SiO}_2$  was measured by an yield-calibrated back-illuminated EUV camera (Roper Scientific, Princeton Research). Transmission of EUV pulses through Al foils was taken into account in this measurement. The EUV beam profile as detected in the EUV camera placed 2.2 m downstream from  $\text{SiO}_2$

sample is shown in Figure 4.27 . The generated energy of EUV pulses is  $\sim 40$  fJ/pulse. The emission of EUV pulses comes from a known volume inside SiO<sub>2</sub> nanofilm which is dictated by the dimension of the focal spot of the optical beam (beam waist,  $w_0 \sim 110\mu\text{m}$ ) and the effective thickness  $d$  of SiO<sub>2</sub> film ( $\sim 20\text{nm}$ ) which contributes to EUV emission. Energy density,  $u$  of EUV pulses inside the effective generation volume in SiO<sub>2</sub> can be evaluated,  $u$  can be comfortably assumed to be spatially uniform in the effective generation volume as the effective thickness  $d$  is significantly smaller than the smallest generated wavelength ( $\sim 44$  nm i.e. 30 eV).  $u$  is related to the field amplitude of EUV pulses by the Maxwells equation as;

$$u = \frac{1}{2}\epsilon_m|E_{EUV}|^2, \quad (4.16)$$

where  $\epsilon_m$  is the permittivity at the centroid energy of the measured EUV spectrum for SiO<sub>2</sub>.

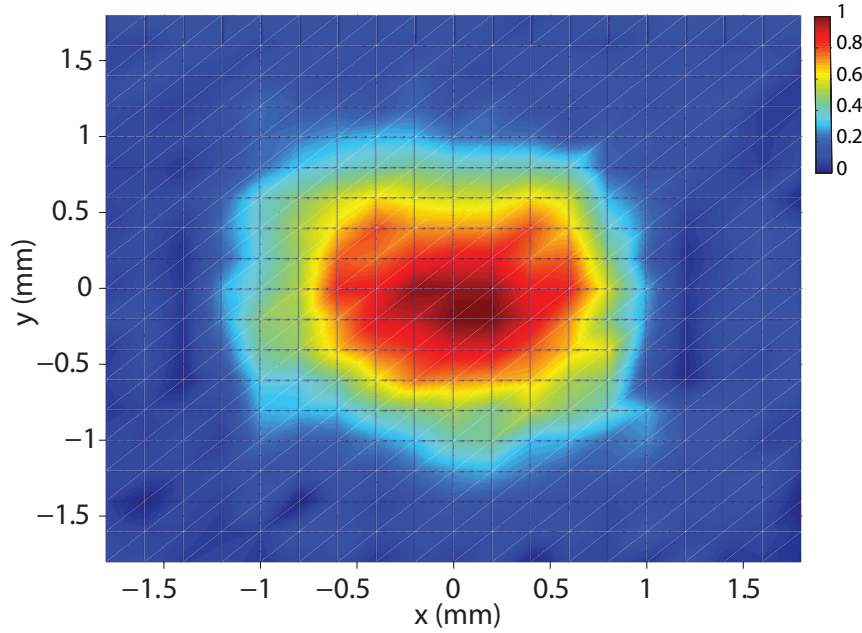


Figure 4.27: Measured EUV beam profile emanating from SiO<sub>2</sub>, recorded 2.2 m downstream from the sample as in experimental set-up shown in Figure 4.1.

A rectangular dielectric slab with an applied electric field along the lateral direction will generate motion of the carriers, hence a current density will be induced. The electric field generated by the motion of the carriers outside the bulk dielectric will be proportional to the induced current density of the carriers inside the dielectric as elaborately discussed in [84][92]. Consequently generated nonlinear current density  $j(t)$  which gives rise to EUV emission is related to the EUV field by the following relation;

$$j(t) = \frac{-e * E_{EUV}(t)}{Z_0 d}, \quad (4.17)$$

where  $Z_0$  is the impedance of vacuum ( $\sim 377\Omega$ ) and  $d$  is the effective thickness of sample generating EUV[92]. The current density reaches values of  $\sim 10^{11}A/m^2$  which is approximately an order of magnitude higher compared to earlier efforts in sub-PHz ranges [91]. The dynamic nonlinear conductivity  $\sigma(t)$  shown in Figure 4.28 evaluated from the precise knowledge of driving optical field  $F(t)$  and current density  $j(t)$  profile and their relative timing as [93]  $\sigma(t) = \frac{j(t)}{F(t)}$  builds up within approximately  $\sim 0.7fs$  and switches periodically at the frequency of the generated EUV field, that is, it turns-on and off within approximately  $\sim 30$  attoseconds (inset in Figure 4.28) implying an extreme nonlinearity which is essential in electronic circuitry. Negative values of the dynamic conductivity imply that electrons move in opposite directions with respect to the applied field force every second half cycle of their oscillation (Figure 4.28); a regime earlier recognized in intraband coherent electron motions in semiconductors superlattices and is here extended into the multi-PHz range. Further study seeking correlation between real and imaginary part of the dynamic nonlinear conductivity ( $\sigma(\omega)$ ) can provide evidence if amplification of a EUV radiation impinging on SiO<sub>2</sub> nanofilm concurrently with the ultrafast electron motion of electrons driven by optical pulses is possible? This effect is also referred to as Bloch oscillator gain in THz driven superlattices.

As it currently stands, measured current density and dynamic conductivity in Figure 4.28 are not shown to be reproducible in every laser shot of the experiment i.e. microscopic intraband currents are not shown to be field reproducible, field profiles of  $\sigma(t)$  and  $j(t)$  may be the ones for a single shot of the laser pulse. In the next chapter we present experiments which demonstrate reproducibility of intraband currents in every shot of the laser pulse which is essential to substantiate multi-PHz metrology presented in this work.

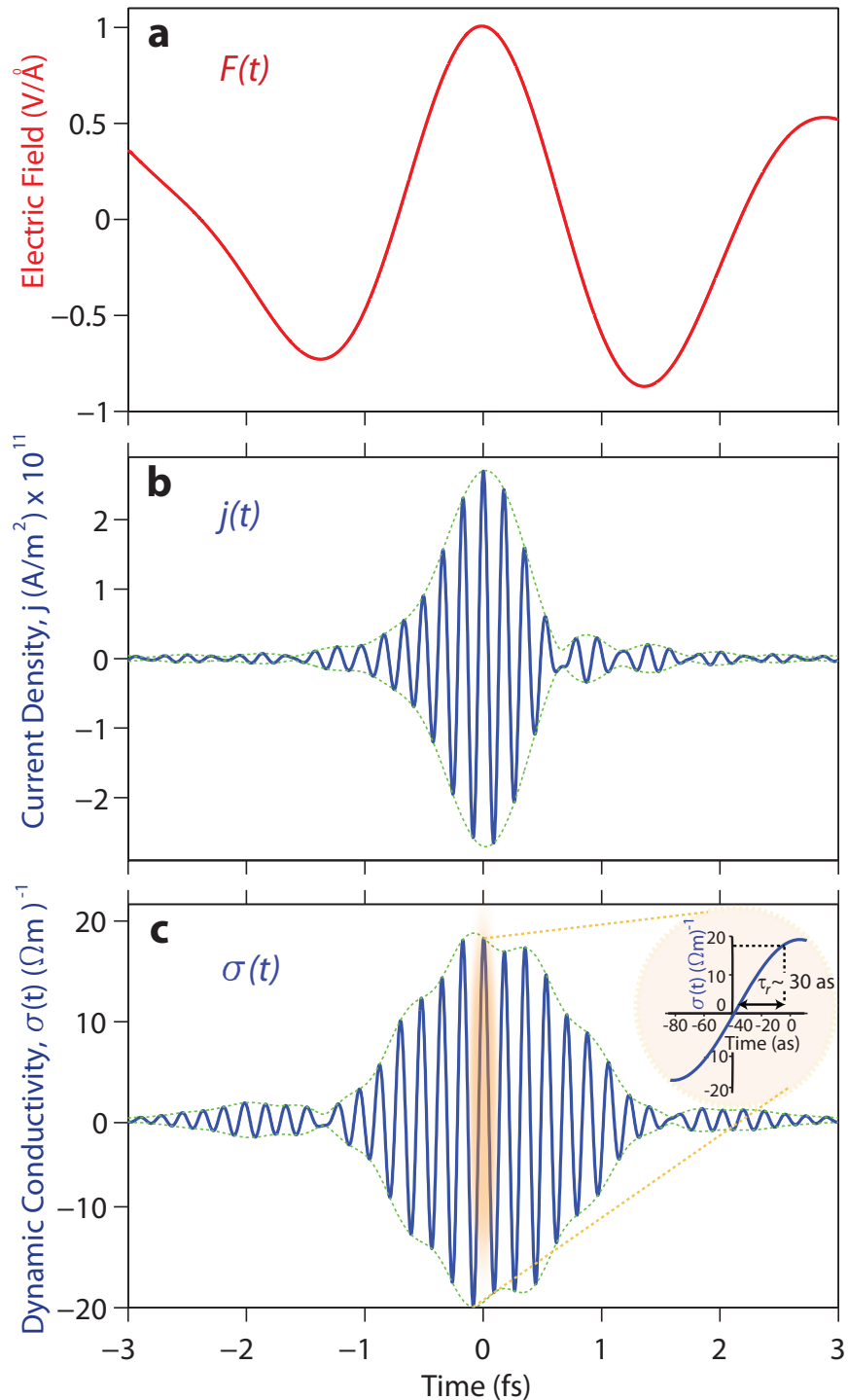


Figure 4.28: **Nonlinear multi-PHz current density and dynamic conductivity of  $\text{SiO}_2$ .** **a**, Temporal profile of the optical field generating nonlinear intraband electric current in  $\text{SiO}_2$ . **b**, **c**, Evaluated nonlinear current density  $j(t)$  and dynamic conductivity  $\sigma(t)$  in  $\text{SiO}_2$  respectively. Inset in Figure 4.28c highlights the rapid switching of the conductivity within approximately  $\sim 30$  as.



# Chapter 5

## Phase coherence of Multi-PHz currents in SiO<sub>2</sub>

In the previous chapter we have demonstrated access into envelope and frequency sweep of field induced intraband current in SiO<sub>2</sub> via probing the dynamics encoded in the time-structure of the emitted EUV radiation but the technique is inherently insensitive to the instantaneous EUV field waveform (carrier envelope phase, CEP). Here we demonstrate CEP stability of EUV fields generated from SiO<sub>2</sub> which eventually connote to waveform reproducibility of microscopic intraband currents; emitted EUV fields from SiO<sub>2</sub>  $E_{EUV}(t)$  has been shown in the previous chapter to have a linear relation with intraband current  $J(t)$ , that is  $J(t) \propto E_{EUV}(t)$ . We establish the capability to vary the CEP of EUV fields with a precision of  $\sim \pi/20$  rad. Long term reproducibility of the EUV waveform (intraband current) and its immunity to CEP fluctuations of the driver field is an important ingredient for the extension of electronics from the time scale of the envelope of the EUV pulse which is compatible to a frequency of  $\sim 2.2$  PHz to its carrier frequency which is  $\sim 6$  PHz.

### 5.1 CEP of isolated attosecond pulses generated in SiO<sub>2</sub>

Carrier envelope phase (CEP) stability of few cycle laser pulses at mid-infrared frequencies has a pivotal importance in attosecond physics wherein highly nonlinear process of high harmonic generation (HHG) in gases is administered by CEP of driving laser, variation of CEP of driving laser is manifested as birth of an isolated attosecond pulse or a twin burst of attosecond pulses in HHG process [64]. Even though nearly 15 years have passed since the demonstration of first isolated attosecond pulses in 2001 [31], the information pertaining to CEP stability of attosecond pulses is yet to be demonstrated. Metrology of attosecond pulses rely on projection algorithms which retrieves information of such pulses from an experimentally measured attosecond streaking spectrogram, these reconstruction algorithms provide substantial information about attosecond pulses such as their spectral chirp and pulse duration but they fail to furnish any clue about their CEP and its stability

over time.

In this work, we demonstrate stability of CEP of isolated EUV attosecond pulses (intra-band current) generated from SiO<sub>2</sub>. We build on a theoretical work from Liu et. al [94] where authors have shown that interference arising from photoelectrons generated by EUV pulses and the ones generated by above threshold ionization (ATI) is sensitive to CEP of EUV pulses. In our experiment, EUV pulses generated from SiO<sub>2</sub> and their driving laser pulses are reflected-off and focused by an Au coated mirror onto an Ar gas jet, Figure 5.1. This arrangement warrants ultimate interferometric stability for the two pulses. Here EUV pulses are not spectrally filtered by Al foil in contrast to expt. set-up shown in Figure 4.1 (chapter 4). At the same time reflection from Au mirror suppresses the high-energy bandwidth of our single-cycle driving pulses giving rise to a few cycle pulse centred around 830 nm. EUV pulses generate photoelectrons via the single photon ionization of Ar atoms and the generated photoelectrons are detected in a time of flight (TOF) mass spectrometer. Photoelectron spectra of measured by EUV photoionization, ATI and their interference is shown in Figure 5.2. The few-cycle laser pulse generates ATI photoelectrons which have earlier been demonstrated to preserve the phase of their driving laser pulse [95]. Furthermore, the photoelectrons generated by EUV pulses undergo streaking by the driving laser pulse. The photoelectrons generated from these two processes interfere in the energy region where streaked EUV photoelectrons spectrally overlap with the ATI electrons, which grossly spans from 1 to 7 eV. An intrinsic time delay between ATI and EUV generated electrons is arising from their distinct generation mechanisms. ATI electrons are generated by tunnel ionization at peak of the driving pulse [96] ensued by acceleration by field and re-scattering from the atomic core which typically lasts longer than a half-cycle of the driving laser pulses, whereas EUV pulses are synchronized to the peak of driving optical pulses as is demonstrated by measurements described in chapter 4, hence EUV generated photoelectrons are also synchronized to the peak of the driving laser pulse.

## 5.2 Dispersion control of CEP of EUV pulses

Material-dispersion induced variation of CEP is a well established paradigm in ultrafast-physics, here we have varied CEP of EUV pulses by letting the pulses propagate thorough a Xe filled gas tube (see Figure 5.1), whose pressure was delicately controlled. CEP variation on EUV pulses by Xe can be evaluated by the following relation;

$$\Phi_{CEP} = -\frac{\omega^2}{c} \frac{d\eta}{d\omega} \Big|_{\omega_{EUV}} \Delta L \quad (5.1)$$

where  $\eta$  is the refractive index of Xe gas in the studied spectral width,  $\omega_{EUV}$  is the frequency of the EUV pulses and  $\Delta L$  is the length of the tube containing Xe. Information of refractive indices in the EUV spectral domain can be obtained from atomic scattering factors (Ref. CXRO database [69]) and thereby using the following relation;

$$\eta = 1 - \frac{r_e}{2\pi} \lambda^2 n_{Xe} (f_1 + i f_2) \quad (5.2)$$

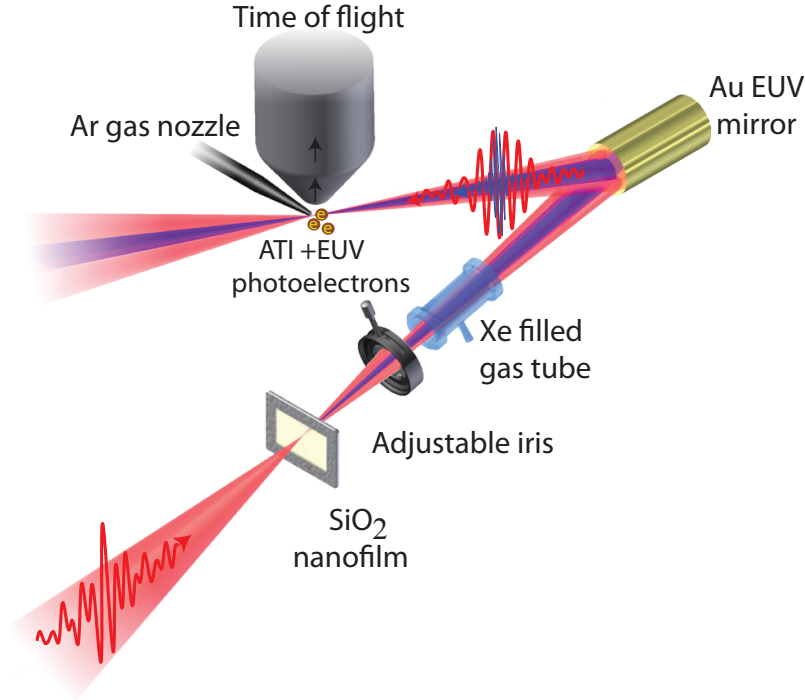


Figure 5.1: Experimental set-up: EUV pulses generated from a SiO<sub>2</sub> nanofilm and the optical driver are reflected-off an Au coated mirror and focused onto an Ar gas jet. Photoelectrons generated by ATI and direct photoionization by EUV pulses are recorded in TOF spectrometer. Variation of Xe gas pressure in a gas tube along the beam path of EUV pulse introduces a definite amount of CEP variation on EUV pulse.

where  $n_{Xe}$  is the number density of Xe atoms,  $r_e$  is the classical electron radius,  $f_1$  and  $f_2$  being atomic form factors. Ignoring absorption of EUV photons by Xe atoms, variation of CEP with Xe gas pressure can be estimated. We estimate that the variation of the pressure from  $1 \times 10^{-3}$  to  $1 \times 10^{-2}$  mbars in our experiments can introduce a  $\Delta\phi_{CEP}$  variation of the EUV pulse on the order of  $\sim 1.6\pi$  rad. Modulation of interference fringe pattern on variation of CEP of EUV pulses is shown in Figure 5.3

The maximum group delay and group delay dispersion (GDD) introduced by Xe on EUV pulse is 150 as and  $100 \text{ as}^2$  respectively for the highest pressure of Xe used in this study implying that the EUV pulse is virtually unaffected by the Xe gas pressures used in this experiment. Variation of group delay of EUV pulses on increase of Xe gas pressure is shown in Figure 5.4. Group delay is calculated by

$$\tau_g = -\frac{d\phi(\omega)}{d\omega} \quad (5.3)$$

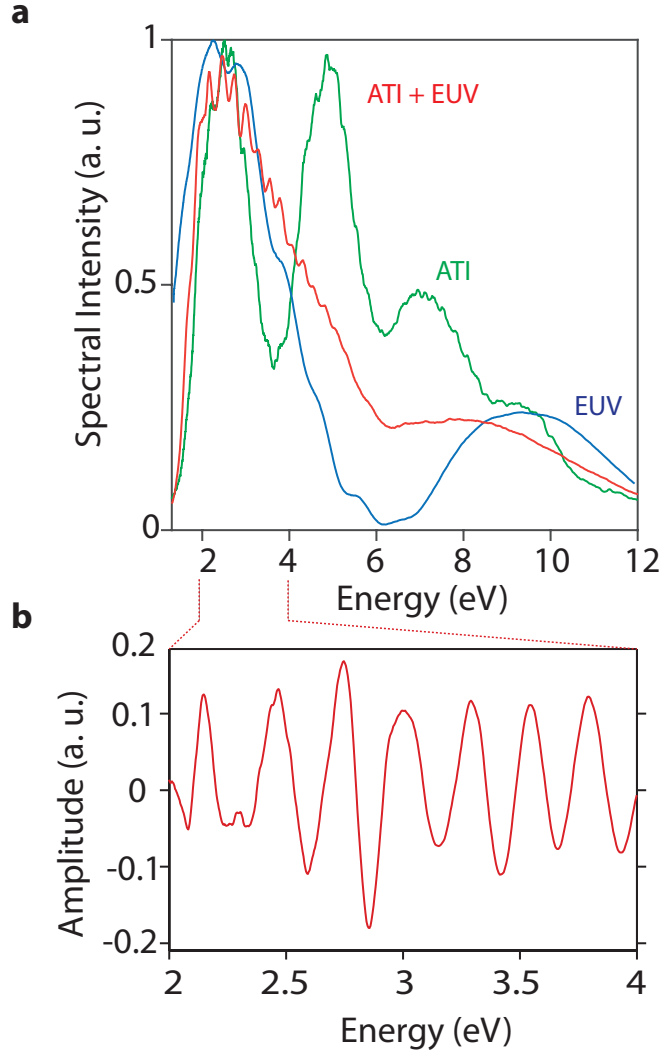


Figure 5.2: **a**, Measured photoelectron spectra of ATI, EUV photoionization and their interference. **b**, Interference fringes of EUV and ATI photoelectrons can be better visualised by removing the DC component in the interference spectrum as presented in **a**.

$$\tau_g = -\frac{d(\omega\eta(\omega))}{d\omega} \frac{\Delta L}{c} \quad (5.4)$$

The CEP shift introduced by Xe gas on EUV pulse can also be extracted by Fourier transforming (FT) the spectral fringe pattern. FT of one of the spectrum in Figure 5.3 is shown in Figure 5.5, which clearly shows that there is one frequency with a period  $\sim 16$  fs present in the interference spectra. The variation in temporal phase for the peak with a period of  $\sim 16$  fs in the FT spectra measured for different Xe gas pressures corresponds to the net CEP change experienced by isolated EUV pulses. Figure 5.5 shows variation of

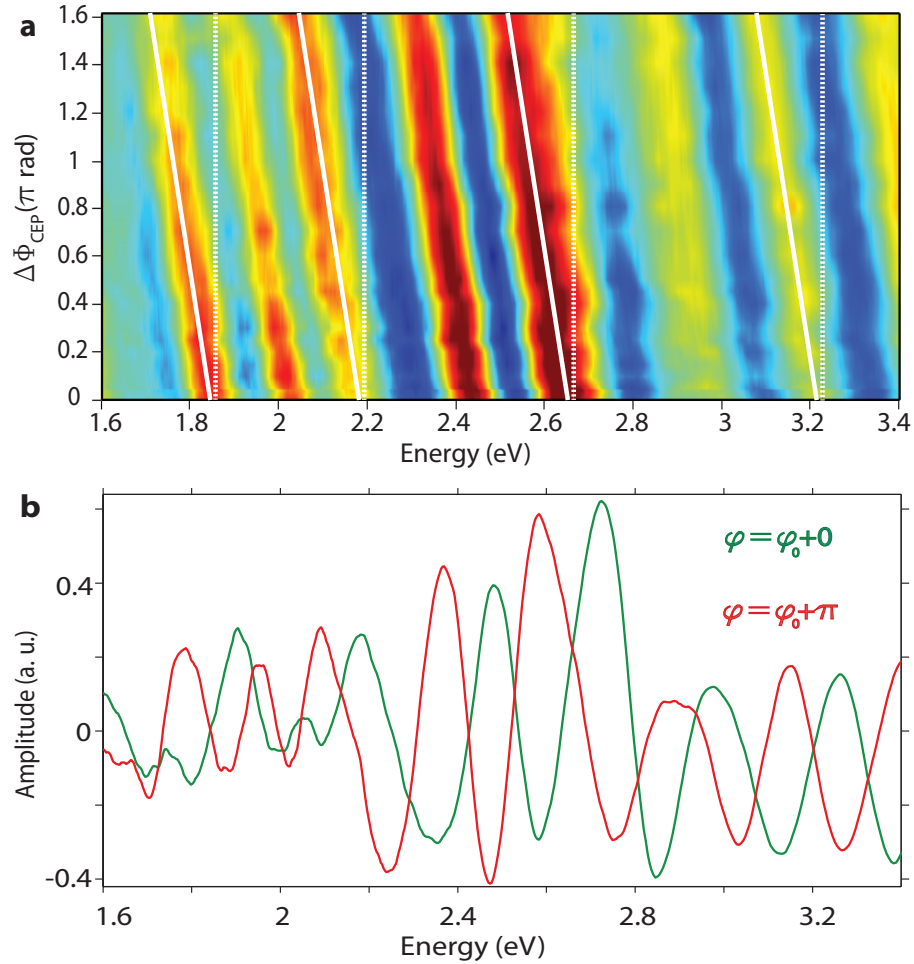


Figure 5.3: **a**, ATI-EUV photoelectron interference spectra as a function of the CEP variation of EUV pulse, solid white (tilted) and white dashed (vertical) lines are to guide the eyes to the linear variation of interference pattern on linear variation of CEP of EUV pulses. **b**, Comparison of spectral interference pattern for two different CEPs of EUV pulse differing by  $\Delta\phi_{CEP} \approx \pi$  rad.

CEP measured from FT spectra at different gas pressures which is in close agreement with estimated CEP variation as shown in Figure 5.3. The fringe visibility (contrast) in the interference of EUV-ATI photoelectrons depend dramatically on the CEP stability of the laser pulses, spectral fringes tend to disappear and broaden in case of bad CEP stability of driving laser pulses, good CEP stability of laser pulses imply  $\Delta\Phi_{CEP} < 0.1 \pi$  rad.

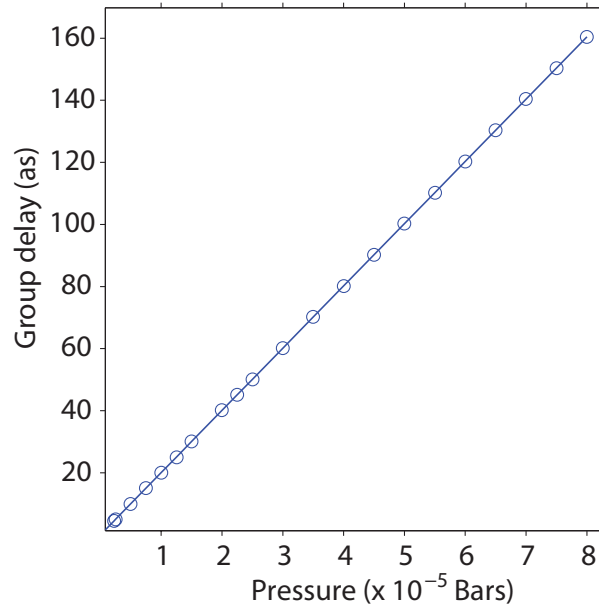


Figure 5.4: Variation of group delay of EUV pulse by Xe gas pressure.

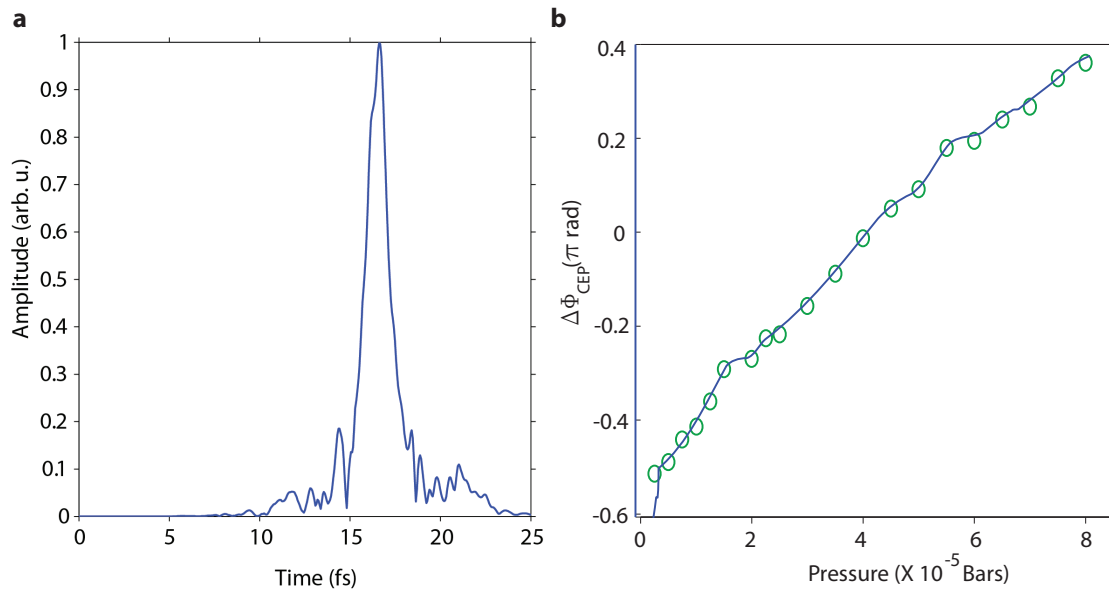


Figure 5.5: **a**, Fourier transform of one of the interference spectra in Figure 5.3a. **b**, CEP of EUV pulses as extracted by FT of the interference spectra for different pressures of Xe gas.

### 5.3 Origin of fine spectral fringes ( $\sim 0.35$ eV) in ATI-EUV interference

Spectral interference between ATI and EUV photoelectrons with a spectral fringe spacing of  $\sim 0.35$  eV arises from interference between a train of ATI photoelectron bursts generated by few-cycle laser pulse and a continuum photoelectron spectrum generated by EUV pulse from SiO<sub>2</sub>. A single cycle laser pulse (which generates EUV pulse from SiO<sub>2</sub>) after reflection off an Au coated mirror will have its centroid wavelength moving from visible to infrared part of the spectrum and correspondingly the pulse getting significantly stretched (towards few-cycles). Although EUV and laser pulses have zero delay between them (see expt. set-up in Figure 5.1), ATI photoelectrons will have a delay offset compared to electrons generated by photoionization from EUV pulses as they are first tunnel-ionized at time  $t=0$  fs (peak of the half-cycle) released with zero kinetic energy, are accelerated by laser field and later re-scatter from the atomic core which introduces a delay of  $\sim 2$  fs between ATI and EUV photoelectrons. Figure 5.6 shows an ATI electron bursts (pulse train) generated by a few-cycle laser pulse, an isolated EUV pulse and their spectral interference pattern arising from their interference at a delay of  $\sim 2$  fs. Further simulations by simulating ATI pulse train with a TDSE code are required to validate the above hand-waving argument of origin of spectral fringes of spacing  $\sim 0.35$  eV in the measurements.

### 5.4 Dependence of CEP of EUV pulses on CEP of driving laser pulses

A CEP stable laser pulse has an underlying stable frequency comb which has a long term stability with a small jitter  $f_0$  in the comb lines which translates to  $\Delta\phi_{CEP}$  in the time domain. Nonlinear frequency conversion of driving frequency comb (driving laser pulse) generates high-harmonics of comb lines present in the fundamental frequency comb with a spacing of  $2f_r + 2f_0$ , thus controlling  $f_0$  primarily enables control over CEP jitter of EUV pulses as well. To theoretically investigate the effects of the laser CEP stability ( $f_0$  fluctuation) on that of the generated EUV pulses we employed the semiclassical model (see chapter 4). Figure 5.7 shows that for a variation of CEP of driving laser pulses from  $-0.06$  to  $0.06$   $\pi$  rad (which is the typical stability obtained in our Laser system) the CEP of the EUV pulse changes marginally by  $\Delta\phi_{CEP} \sim \pi/20$  rad and therefore it is in excellent agreement with our experiment as will be shown below.

Long term stability of CEP of EUV pulses can be monitored by registering several interference spectra over a long time. Since the CEP of driving laser pulses is locked, demonstrating such a measurement connotes to reproducibility of the EUV waveform (intra-band current) and its immunity to CEP fluctuations of the driver field. Interference spectra recorded for more than 15 minutes are shown in Figure 5.8. The CEP stability evaluated from the dynamic shift of the interference fringes in Figure 5.8a was less than  $\sim \pi/10$  as displayed in Figure 5.8c implying that the EUV waveform and its source intra-

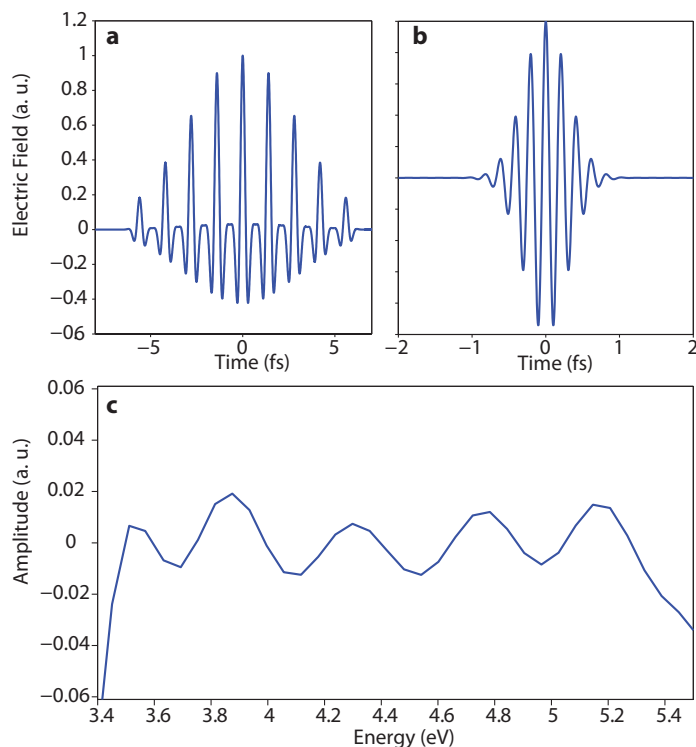


Figure 5.6: **a**, ATI pulse train (centred at 4 eV) arising from a few cycle driving laser pulse. **b**, Isolated attosecond pulse arising from SiO<sub>2</sub>. **c**, Spectral interference between the two pulses at a delay of  $\sim 2$  fs.

band current are reproducible with an accuracy better than  $1/20^{th}$  of their carrier period. Thus the above measurement and the semiclassical simulations support the generation of a field-reproducible (phase-coherent) intraband current with currently accessible laser systems with typical CEP stability of less than  $0.1\pi$  rad.

Interference between ATI and EUV photoelectrons can also be modulated by varying the CEP of driving laser pulses, CEP of driving laser pulse will change both the CEP of ATI pulse train as well as CEP of EUV pulse. Effect of CEP of single-cycle driving laser pulses on the CEP of generated EUV attosecond pulses from SiO<sub>2</sub> as calculated from the semiclassical model is shown in Figure 5.9. Absolute CE phase of EUV pulses plunges by nearly  $\pi$  rad after every  $\pi$  rad CEP variation of the driving laser pulse. Accordingly, we expect modulation pattern of interference between ATI and EUV to dramatically change direction of fringe movement every  $\pi$  rad CEP change of driving laser pulse, as is the case as shown in Figure 5.10a. The change of direction in variation of spectral fringe pattern with CEP of driving laser pulse in the spectrogram is marked with dashed black lines. Figure 5.10c shows variation of CEP as evaluated from spectral interference pattern which corresponds to a fringe spacing of  $\sim 0.35$  eV.

Unfortunately, the evaluation of CEP from this interference pattern includes the in-

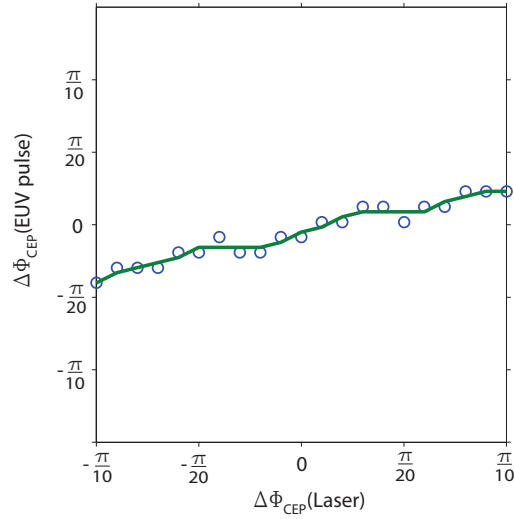


Figure 5.7: Calculated dependence of CEP of isolated EUV attosecond pulse on CEP variation of driving laser pulse, the CEP variation of driving laser pulse shown here in the bottom axis is twice as big as the actual CEP jitter of driving laser pulses in the experiment.

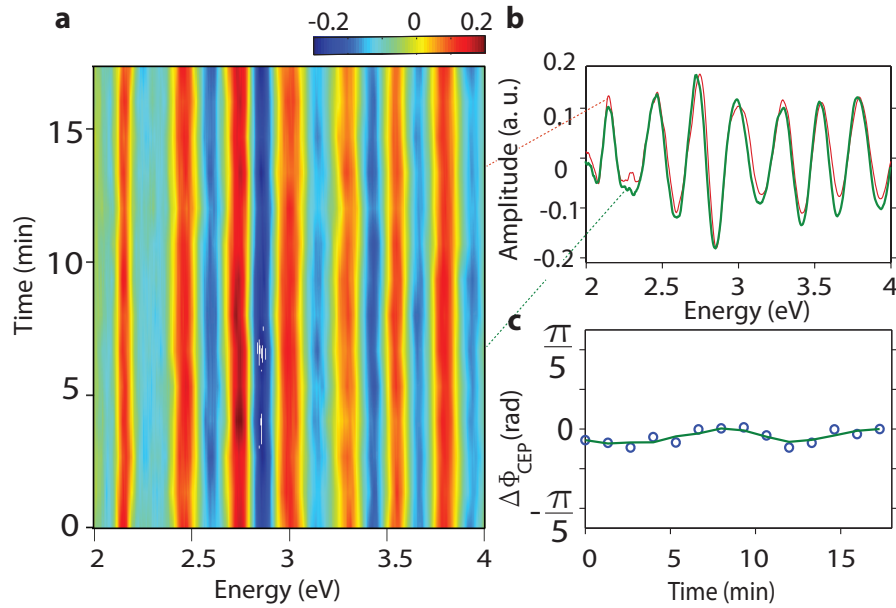


Figure 5.8: **a**, Spectral interference between ATI and EUV photoelectrons in Ar recorded for more than 15 minutes. **b**, comparison of spectral interference pattern recorded at two different moments of time. **c**, Evaluated CEP of EUV pulses (intraband current) as retrieved from spectra in **a**.

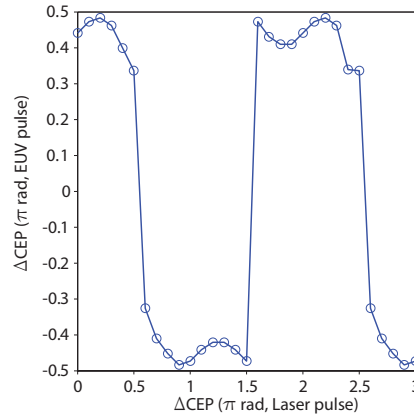


Figure 5.9: Dependence of CEP of EUV pulse on CEP of driving laser pulses as simulated by semiclassical model (see chapter 4).

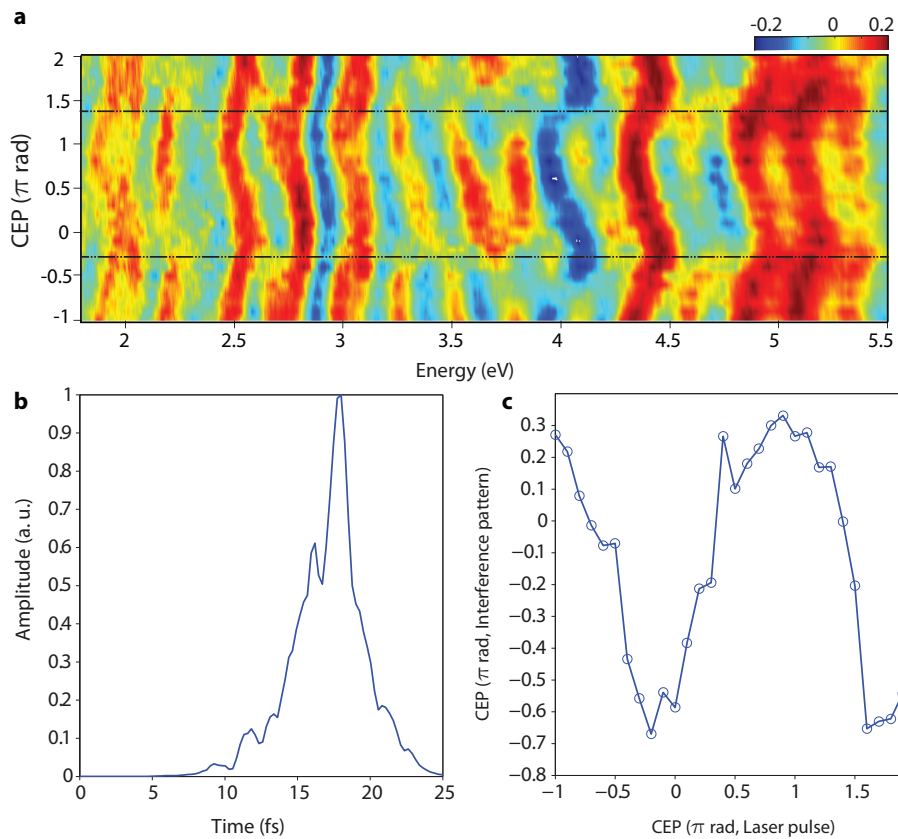


Figure 5.10: **a**, ATI-EUV interference spectra recorded as function of varying CEP of driving laser pulse. **b**, FT of one of the measured interference spectra. **c**, CEP variation of the interference spectra as a function of the varying CEP of driving laser pulse.

terplay of CEP variation of ATI pulse train as well as CEP variation of EUV pulses. Evaluation of modulation of CEP of EUV attosecond pulses on variation of CEP of driving laser pulse can be made by removing the CEP variation of ATI from the CEP variation as measured from ATI-EUV interference. ATI spectra were recorded a function of CEP of driving laser pulse to this end as shown in 5.11. ATI spectrum undergoes very similar modulation in its spectral pattern on variation of driving laser CEP but the fine spectral fringes ( $\sim 0.35$  eV) which are signature of interference between ATI and EUV photoelectrons are not present. The most dominant frequency in the spectrum corresponds to a period of  $\sim 2.3$  fs, the temporal phase extracted at this frequency for all the spectra is presented in Figure 5.11c.

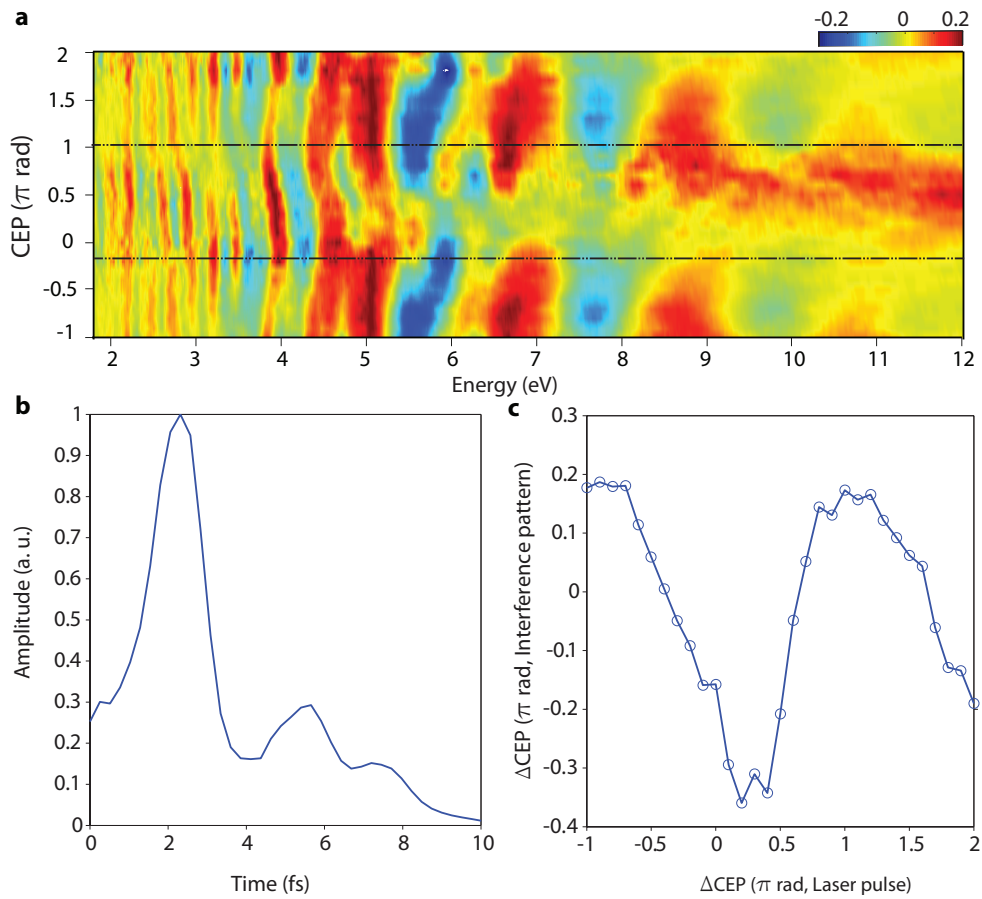


Figure 5.11: **a**, ATI spectra recorded as function of varying CEP of driving laser pulse. **b**, FT of one of the measured spectra. **c**, CEP variation of the ATI pulse train as a function of the varying CEP of driving laser pulse.

Evaluated variation of CEP of EUV pulses on variation of CEP of single cycle driving laser pulse from the measurements shown in Figure 5.10 and Figure 5.11 is shown in Figure 5.12a. Figure 5.12b shows the variation as calculated by semiclassical model. CEP of EUV

pulses undergo marginal change when the CEP of driving pulse is varied from  $-1$  to  $-0.6 \pi$  rad but swiftly plunge around  $-0.5 \pi$  rad and thereafter again have marginal change from  $-0.4$  to  $0 \pi$  rad which is precisely reproduced by the semiclassical model. This effect owes its origin from the fact that EUV pulses (intraband current) are temporally locked to field maxima of driving laser pulse and the change of CEP of driving pulse by more than  $\pi/2$  rad leads to an instant of switch between the half-cycles generating EUV radiation, EUV emission switches from an earlier dominant half-cycle to the one less intense.

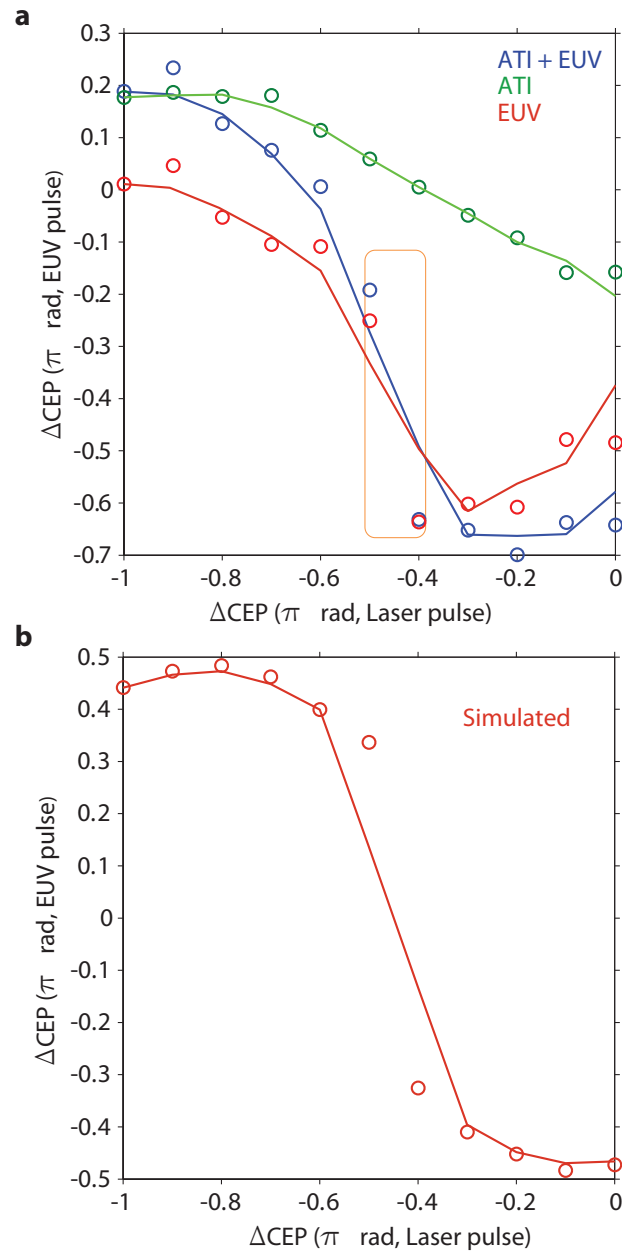


Figure 5.12: **a**, Alteration of CEP of ATI pulse train, EUV attosecond pulse and ATI-EUV interference pattern on CEP variation of the driving laser pulse, displayed orange rectangular box shows the swift jump of CEP of EUV pulse around  $0.5 \pi$  rad CEP of driving pulse. **b**, CEP variation of isolated EUV attosecond pulse as calculated by semiclassical model.



# Chapter 6

## Ultrafast dephasing of field-induced polarization in SiO<sub>2</sub>

Electron dynamics brought on by light waveforms in SiO<sub>2</sub> undergoes complex interplay between interband and intraband effects which have spectral signatures in the polarization spectra measured from SiO<sub>2</sub> [23]. Time-resolved experiments on EUV generation from SiO<sub>2</sub> as presented in chapter 4 revealed important role of intraband dynamics i.e coherent transport (motion) of electrons in its conduction band but it obstructed us to get information on the interband dynamics of electrons. To this end, we have performed an experiment in the spectral region where polarization induced by interband and intraband dynamics both contribute but interband contribution is dominant, i.e. the spectral region around the band gap of SiO<sub>2</sub>(6-18 eV,  $E_g$  of SiO<sub>2</sub> is  $\sim 9.5$  eV ). Its important to note that in the EUV spectral range contribution from intraband contribution is superior to interband by 2-3 orders of magnitude (see chapter 4). Electron-hole pairs generated ensuing laser pulse interaction with SiO<sub>2</sub> generate interband polarization. Electron-hole pairs loose the relative phases among each other due to strong Coulomb correlations among them and scattering processes. This rapid loss of coherence among the electron-hole pairs in interband polarization is accounted for in simulations presented in chapter 4 by an empirical value of  $\sim 400$  as. This value is chosen as it gives clean spectra in the interband contribution. Here in this chapter we present experiments to justify this value of dephasing time for interband polarization.

The time it takes for the electron-hole pairs to go out of phase with respect to each other leading to dephasing of the microscopic interband polarization can be conveniently studied by pump-probe techniques, wherein the coherence among the electron-hole pairs is generated by an ultrashort pulse and the dephasing is probed by another pulse. The shortest de-coherence (dephasing) times that can be measured with confidence by this technique is unfortunately limited by the time step in the pump-probe measurement and the pulse duration of the driving laser pulse. In order to access ultrashort dephasing times of interband polarization, which may be around several hundreds of attoseconds, we have utilised a novel polarization interference technique. An optical attosecond pulse which has more than 50 % of its energy in one half-cycle whose FWHM (of the field profile) is  $\sim 400$

as are used, the carrier envelope phase (CEP) of this waveform is varied such that polarization is induced in SiO<sub>2</sub> by two different half-cycles. Interference generated by these two half-cycles is variable with CEP of the optical attosecond pulses. Measuring polarization spectra as function of CEP of optical attosecond pulses generate a spectrogram. The extent of interference of the polarization induced by the two half-cycles depends strongly on dephasing times, the modulation depth along the CEP axis in the CEP spectrogram depends on temporal overlap between the induced polarization from the two half-cycles. Strong temporal overlap i.e. long dephasing times for the polarization leads to lesser modulation along the CEP axis whereas weaker temporal overlap (short dephasing times) generates CEP spectrograms with strong modulation. We have followed this approach in this work, in the following we present experimental results and simulations from SBEs, further work is underway for a concrete interpretation of the experimental results.

## 6.1 Results and Discussion

Optical attosecond pulses were first synthesized by a 2<sup>nd</sup> generation light field synthesizer [37] and characterised by the technique of attosecond streaking and were then focused onto a 125 nm thick free standing polycrystalline SiO<sub>2</sub> sample. Vacuum ultra-violet (VUV) (6-18 eV) spectra emanating from ultrathin SiO<sub>2</sub> were measured as a function of CEP of optical attosecond pulses. Experimentally measured CEP spectrogram for two different intensities of the driver pulses are shown in Figure 6.1. The experimental spectrograms were also normalised along the energy axis as in Figure 6.1c, d in order for the spectral intensity modulation as function of CEP of driver can be transparently seen. In the CEP spectrograms we transparently see a  $\pi$  periodicity of measured spectra along the CEP axis which arises due to presence of inversion symmetry in polycrystalline SiO<sub>2</sub>. Crystalline SiO<sub>2</sub> (quartz) is known to be piezoelectric implying absence of inversion symmetry in its crystal structure, hence polarization induced by field waveforms differing in CEP by  $2\pi$  will only be identical. However, in polycrystalline sample, random orientations of polycrystals make the sample effectively inversion symmetric, which is manifested by the observation of  $\pi$  periodicity of spectra along the CEP axis in the measured spectrograms.

An intuitive estimate of the temporal resolution in the measurement can be made from the step size used in CEP variation which was  $0.1\pi$  rad. A  $2\pi$  rad variation in CEP corresponds to movement of one complete wavecycle of optical attosecond pulses which is  $\sim 2$  fs for central energy of 1.9 eV of optical attosecond pulses, thus a step size of  $0.1\pi$  rad in the measurement corresponds to a temporal resolution of  $\sim 100$  as.

A two band SBE simulation whose details were presented in chapter 4 was performed for various dephasing times of the interband polarization. Briefly, first conduction and the highest valence band of SiO<sub>2</sub> as extracted from an *ab initio* program package Quantumwise [79] were used in the SBE simulation with the laser driver being the optical attosecond pulse as measured experimentally; dipole matrix elements describing coupling strength between valence and conduction band were also extracted by Quantumwise. The phenomenological interband polarization dephasing time (T2) as in [47] was varied in our simulations. In

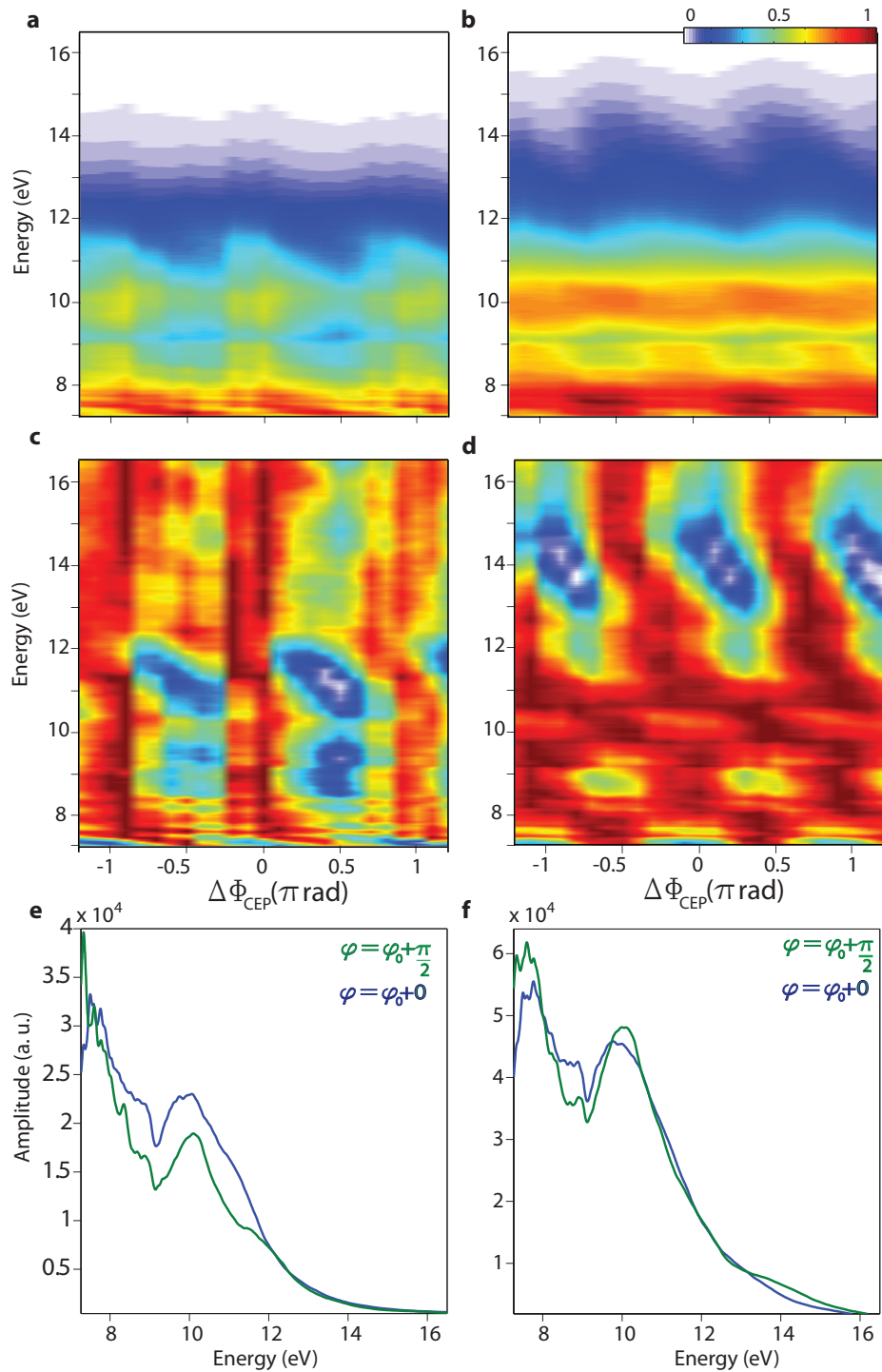


Figure 6.1: **a, b**, Experimentally measured VUV spectra from polycrystalline  $\text{SiO}_2$  as a function of CEP of optical attosecond pulses for two different peak intensities of  $4 \times 10^{13} \text{ W/cm}^2$  and  $7 \times 10^{13} \text{ W/cm}^2$  respectively. **c, d**, Normalised CEP spectrograms along the energy axis of spectrograms shown in **a** and **b** respectively, spectrograms are normalised in order for the interference modulation along the CEP axis at different spectral regions to be more obvious. **e, f** VUV spectra for two different CEPs differing by  $\pi/2$  rad for the two CEP spectrograms in **a** and **b** respectively.

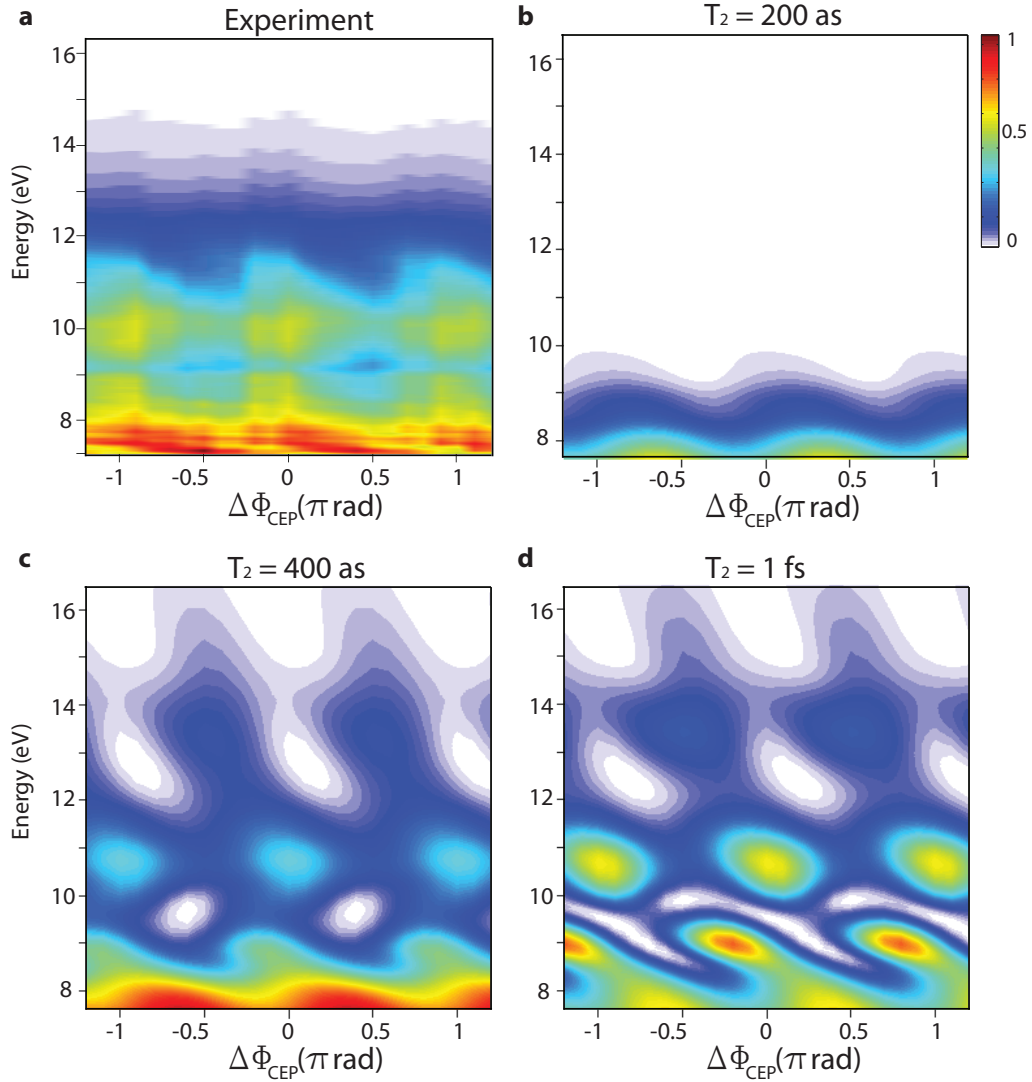


Figure 6.2: Comparison of experimentally recorded CEP spectrogram (a) measured with optical attosecond pulses of peak intensity  $4 \times 10^{13} \text{ W/cm}^2$  with the ones simulated by SBEs for three different dephasing times (b, c, d) of the interband polarization.

Figure 6.2 we show the comparison of experimental spectrogram with the simulated spectrograms for three different interband dephasing times. Calculation of difference (error) between the experimental and simulated spectrograms for different interband dephasing times is presented in Figure 6.3. Minima in this error comes nearly at 400 as providing a first experimental evidence of dephasing times being closer to this value.

Even though plots in Figure 6.2 and 6.3 deem to connote to presence of dephasing time of  $\sim 400$  as in the interband polarization, the physical mechanism behind it is still out of reach, the hand waving argument as to the better agreement between experiential and simulated spectrograms at dephasing time of  $\sim 400$  as is primitive. Scattering terms accounting for Coulomb and scattering of electron-hole pairs with the lattice have to be considered for a meticulous modelling of dephasing. Introduction of the scattering terms into SBEs and their absolute strength is required, efforts towards this direction are currently underway.

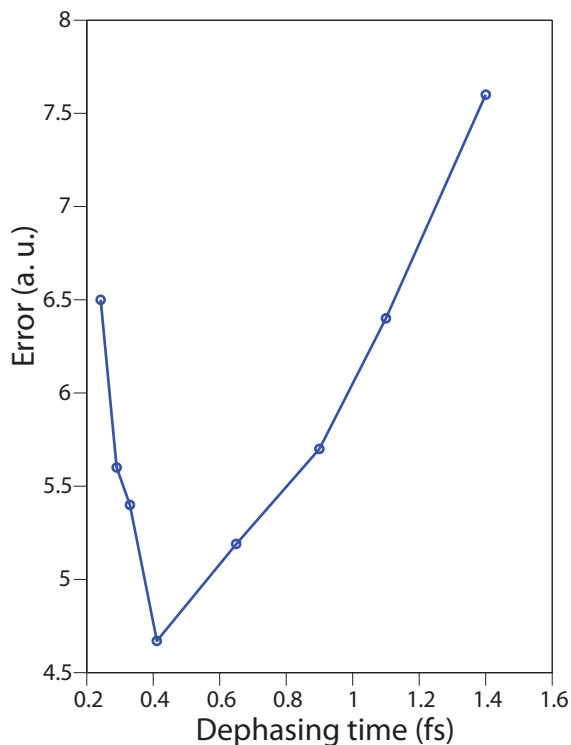


Figure 6.3: Variation of difference (error) between experimentally recorded spectrogram (Figure 6.1a) and the spectrograms simulated by SBEs for different dephasing times, a minima in the error at  $\sim 400$  as dephasing time for interband polarization connote to best agreement between the simulation and the experiment.



# Chapter 7

## Optical attosecond pump-probe spectroscopy: Quantum coherences in Xe

### 7.1 Introduction

Coherence describes all properties of correlation in a quantum system. An external perturbation to a quantum system prepares a wavepacket which evolves over a superposition of several stationary states. The correlation between these states describe the dynamics ensuing the external perturbation i.e. how the coherent evolution of the system unfolds. Coherence in a system is best studied by interferometric techniques, for instance temporal coherence of a wavepacket can be studied by interfering the wavepacket with its replica in a Michelson like interferometer. Coherence of a system is transferable by appropriate coupling to another system, illustratively temporal coherence of an ultrashort laser pulse can prepare a coherent Quantum system by dipole coupling. Investigation of this emerging coherence in the system requires interference by the same kind of coherence excited by another ultrashort laser pulse. Quantum coherence in a system unfolds by an evolution of the wavepacket over several stationary states of the system. If two quantum states ( $\Psi_1$  and  $\Psi_2$ ) with energies  $E_1$  and  $E_2$  are simultaneously excited by an ultrashort laser pulse, the evolution of the formed wavepacket is given by;

$$\Psi(t) = c_1\Psi_1(0)e^{-i(E_1/\hbar+\alpha/2)t} + c_2\Psi_2(0)e^{-i(E_2/\hbar+\alpha/2)t} \quad (7.1)$$

where  $\alpha$  is the phenomenological decay time of the two quantum states due to vacuum fluctuations. Decay of this wavepacket produces an experimentally detectable emission, Fluorescence, which is an exponential decay (dictated by a pre-exponential factor  $\alpha$ ) of induced polarization in the system with underlying periodic modulations whose frequency corresponds to difference in energy between two states. The emission intensity of this Fluorescence is proportional to the square of the transition dipole moment matrix element;

$$I(t) = |\langle\Psi(t)|e.d|\Psi(t)\rangle|^2 \quad (7.2)$$

$$I(t) = Ce^{-\alpha t}(A + B \cos \omega_{12}t) \quad (7.3)$$

where A, B and C are constants and  $\omega_{12}$  is the frequency corresponding to transition between ( $\Psi_1$  and  $\Psi_2$ ) as  $(E_1 - E_2)/\hbar$ . Thus the fluorescence signal is temporally modulated like a sinusoidal function with frequency corresponding to energy separation between the two states. The frequency of this modulation is known as quantum beat. Unfortunately, unavailability of fast detectors in the experiments prevent us from observing these modulations in real time; detectors in the experiments usually record time-integrated signals. So in order to study coherent evolution of a quantum system an interferometric technique has to be used which implies to excitation of the system by two laser pulses and hence recording time integrated signals from both of them. This interferometric technique of studying quantum beats in coherently excited systems is known as "Quantum beat spectroscopy" and is widely used in Femtochemistry [4][5][97]. Theoretical and experimental efforts in the past three decades have led to well established methodologies towards observation of quantum coherence in molecules undergoing a chemical change; amplitude and phase of quantum beats between vibrational levels in molecules reveals bond formation and dissociation dynamics [4][5]. Complex algorithms which shape the field and envelope profile of laser pulses so as to have molecular entities ending up with a pre desired product have been developed.

We present here investigation of quantum coherences in Xe atoms excited by optical attosecond pulses and demonstrate control over their temporal evolution by tuning field strength of the pulses. Quantum excited states in Xe are populated by nonresonant excitation by the optical attosecond pulses. Owing to the broad bandwidth of optical attosecond pulses ( $\Delta\omega \approx 1 - 4.6eV$ ), the excited coherences evolve on time scales close to  $\sim 1$  fs. The temporal coherence of optical attosecond pulse once transferred to atoms of Xe by dipole coupling will have fastest evolving coherences which will be inversely proportional to the bandwidth of driving laser pulses. Availability of attosecond pulses in the extreme ultraviolet domain with a bandwidth  $\sim 30eV$  in principle can prepare coherent quantum systems with extremely fast temporal evolution, but unfortunately bandwidth of ultrafast probe pulses were heretofore limited and such ultrafast coherences could not be studied. The fastest coherences studied in this work are as fast as  $\sim 1fs$ , which are fastest coherences studied in any quantum system to the best of our knowledge. Experiments presented in this chapter of thesis are proof-of-concept experiments for future pump-probe experiments studying coherences in more complex systems with optical attosecond pulses.

## 7.2 Experimental Details

Optical attosecond pulses were synthesized by a  $2^{nd}$  generation light field synthesizer and characterised by the technique of attosecond streaking. Performing an interferometric experiment to resolve quantum coherences in Xe requires a set-up where two identical pulses are used to perturb the system. Herein we have exploited a co-linear set-up to perform such a measurement. In a state-of-art attosecond streaking set-up (see chapter 2), optical and EUV pulses are reflected by mirrors which are of significantly different dimensions owing to

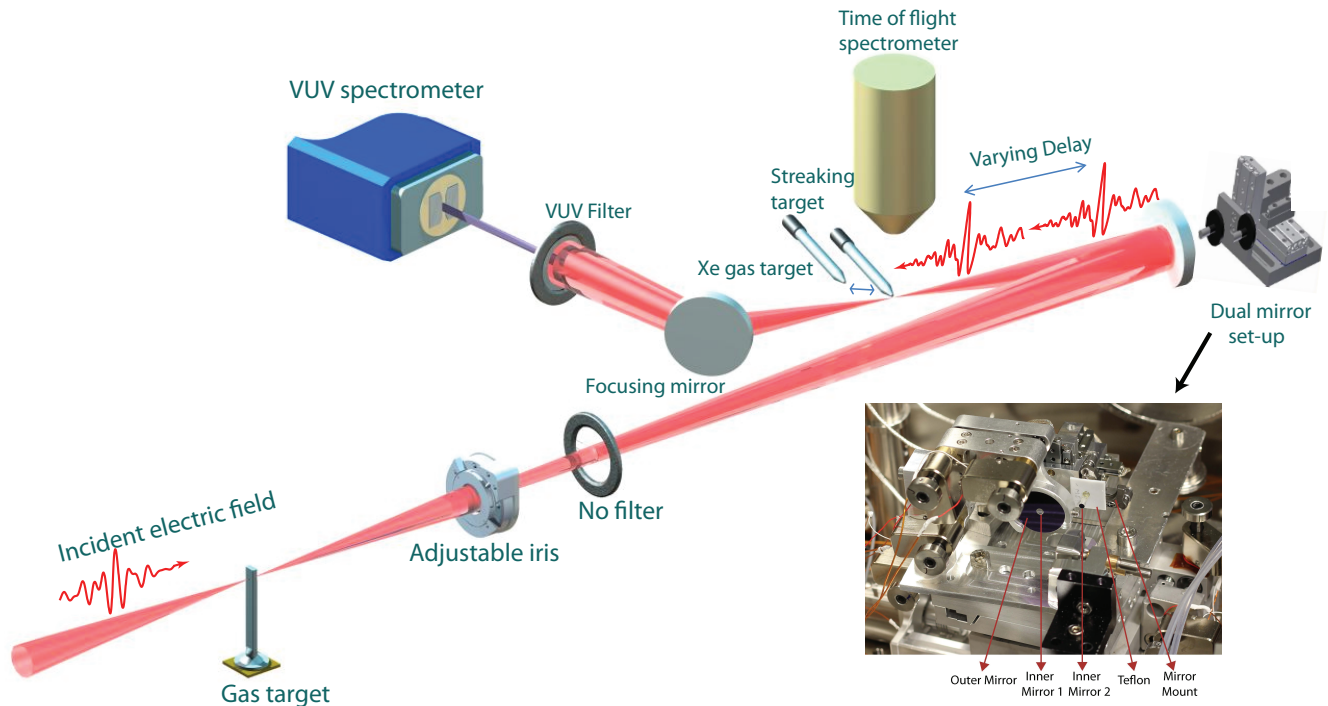


Figure 7.1: Experimental setup: Optical attosecond pulses are first synthesized and characterised by the technique of attosecond streaking, after successful synthesis of optical attosecond pulses, mirror designed to reflect EUV pulses (inner mirror) is replaced by a mirror with identical reflection as the mirror reflecting optical pulses with a 3D piezo stage (shown in inset). The two optical attosecond pulses are then focused on a gas target filled with Xe atoms at  $\sim 10$  mbars with the delay between the two pulses being varied by another piezo stage. VUV emission emanating from this ensemble of Xe atoms is detected by a VUV spectrometer.

smaller divergence of EUV pulses compared to optical pulses. The two mirrors are prepared from the same core mirror and metallic filters in front of smaller (inner) mirror forestall optical pulses from being reflected from it otherwise disrupting the attosecond streaking experiment. Once, synthesis and characterization of optical attosecond pulses has been performed the smaller (inner) mirror reflecting the EUV pulses is replaced by a mirror which has identical reflectivity as mirror reflecting the optical pulses. A 3D piezo stage has been developed to this end. Figure 7.1 shows the set-up developed to switch between two smaller (inner) mirrors utilizing a 3D piezo stage. The collinear set-up as discussed above is used to perform the interferometric measurement of coherences in Xe. Optical attosecond pulses were focused on a gas nozzle filled with Xe, the pulses were delayed with respect to each other by an in-loop piezo stage on which the smaller (inner) mirror is mounted on. The pressure in gas nozzle was maintained as low as  $\sim 10$  mbar preventing Xe atoms

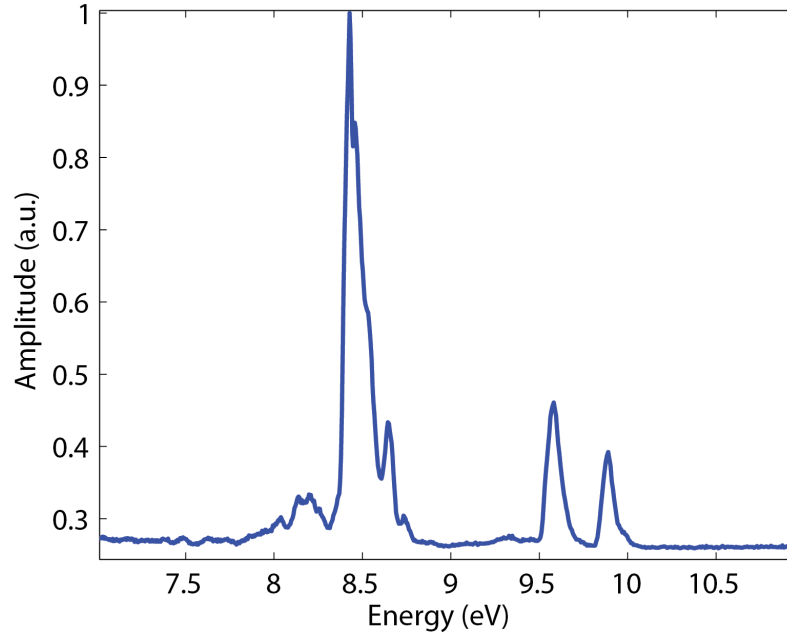


Figure 7.2: Vacuum ultraviolet spectrum arising from interaction of an optical attosecond pulse with Xe atoms.

to form cluster inside the nozzle. The two mirrors reflecting the optical attosecond pulses were interferometrically stabilized to prevent thermal drifts between them which could deter the measurements. Vacuum ultraviolet (VUV) spectrum ( $\sim 6$  to  $11$  eV) emanating from Xe atoms was filtered by a custom designed VUV filter blocking optical spectrum to be detected by a commercial monochromator from Mcpherson. VUV spectra was recorded as a function of delay between the two pulses with their delay being varied from  $-70$  fs to  $70$  fs with a step size of  $200$  as. Figure 7.2 shows a measured VUV spectrum from Xe, three resonant lines have been observed in the measurement. Calibration of the energy axis of VUV spectrometer is described in Appendix E.

### 7.3 Observed Quantum coherences in Xe

Three resonant emission lines in Xe are observed experimentally at  $8.43$  ( $J=1$ ),  $9.58$  ( $J=1$ ) and  $9.91$  ( $J=1$ ) eV; angular momentum quantum number corresponding to each resonant state is mentioned in the parenthesis. Experimentally measured pump-probe spectrogram is shown in Figure 7.3. Temporal modulation for the resonant line at  $8.43$  eV in the measured spectrogram is shown in Figure 7.4, this modulation contains the frequencies (quantum beats) corresponding to interference of resonant emission at this energy ( $8.43$  eV state) with other excited states. Fourier transform of the temporal modulation is shown in Figure 7.5, the time period of observed quantum beats is mentioned with parenthesis in

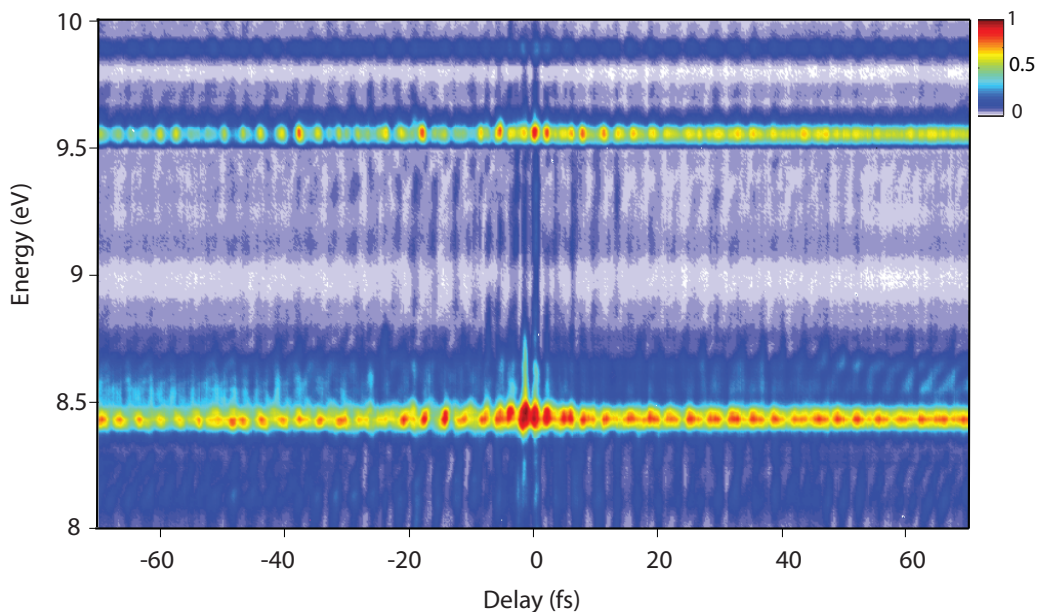


Figure 7.3: Measured VUV spectrogram recorded as a function of delay between two optical attosecond pulses (pump and probe) on their interaction with Xe atoms. Quantum interferences are better time resolved along the positive delay axis which corresponds to probing of interferences by a weaker pulse ( $I \sim 5 \times 10^{12} \text{W/cm}^2$ ) after being initially triggered by a more intense pulse ( $I \sim 5 \times 10^{13} \text{W/cm}^2$ ).

the plot. In the experiments, intensity of one optical attosecond pulse is kept an order of magnitude higher than the other pulse; quantum beats are better time resolved when the quantum coherence is first created by the intense pulse ( $4 \times 10^{13} \text{W/cm}^2$ ) and is probed by the weaker pulse ( $5 \times 10^{12} \text{W/cm}^2$ ). The Fourier transform of the temporal modulation in Figure 7.5 is for such a case. A 2D Fourier transform map which shows the quantum beats appearing for all the electronic states observed in the experiment is displayed in Figure 7.6. Discrete frequencies which correspond to quantum interferences between electronic levels in Xe appear only at the resonant levels in the Fourier spectrogram not at the non-resonant region in the spectrum which corroborates to the fact that we don't see non-linear interference arising from interaction of two optical attosecond pulses with Xe but the real quantum interferences between electronic levels.

Quantum beats appearing in the temporal modulation at the first excited state suggest that quantum interference in our case is explainable by a V-type of atom, where two excited states ( $|a\rangle$  and  $|b\rangle$ ) interfere while decaying to a common ground state ( $|c\rangle$ ). A V-type system can be conveniently modelled by *Liouville- Von Neumann* equation, considering only three electronic states in the description ( $|a\rangle$ ,  $|b\rangle$  and  $|c\rangle$ ) density matrix of the system

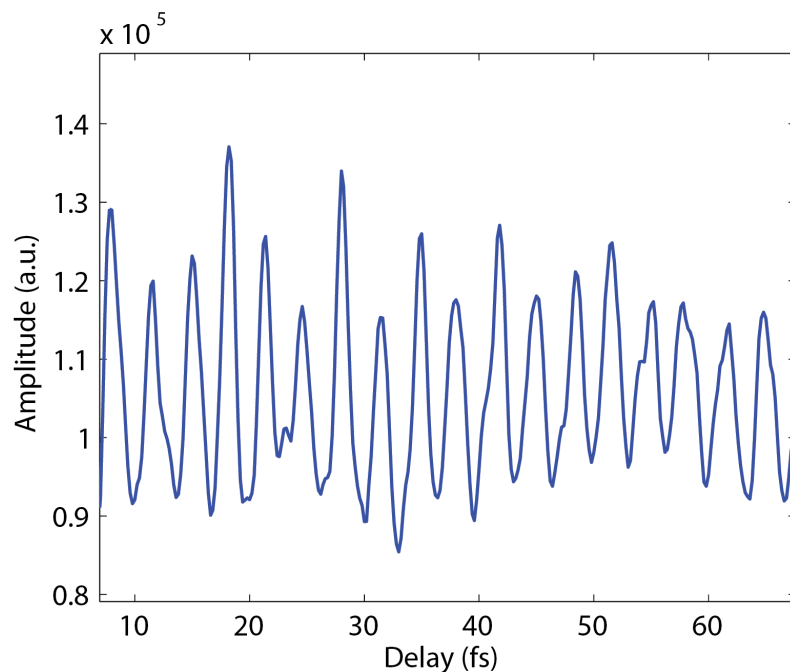


Figure 7.4: Temporal modulation of spectral intensity of resonant line at 8.43 eV as a function of delay between pump and probe optical attosecond pulses.

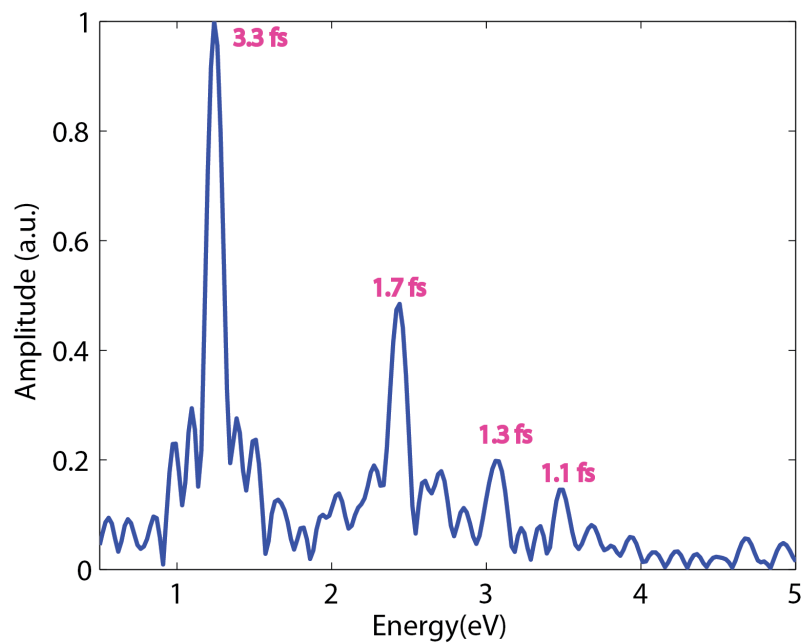


Figure 7.5: Observed frequencies of quantum interferences arising from coherent coupling of state at 8.43 eV with other excited states.

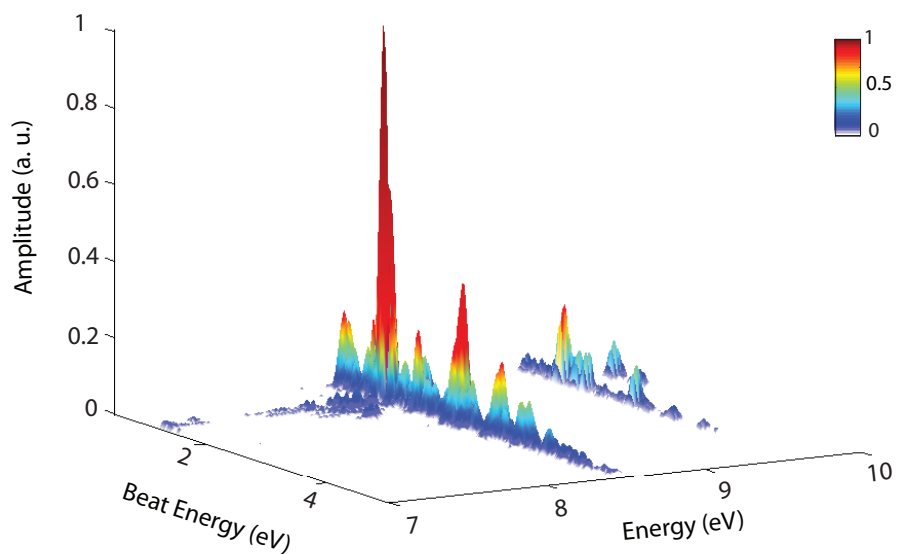


Figure 7.6: Frequencies of quantum interferences present in the three electronic states as measured experimentally. The quantum beat spectrogram is obtained by Fourier transforming the temporal modulation of spectral intensity as function of delay between pump and probe pulses for all the energy range measured in the experiment. Discrete frequencies are present only in the resonant region of the spectrum.

is given as;

$$\rho = \sum_{a,b,c} c_a c_b^* |a\rangle\langle b| \quad (7.4)$$

and their temporal evolution follows,

$$\frac{d}{dt}\rho = -\frac{i}{\hbar}[H, \rho] \quad (7.5)$$

where  $H = H_0 + H_{int}$  is the Hamiltonian describing the system, interaction between the electronic levels is given by dipole coupling  $(-\mu.E)$ . Loss of coherence between the electronic levels can be incorporated by including a term which causes exponential decay of non-diagonal terms in Equation (7) in each level on a time scale of  $\sim ns$ , the modified *Liouville- Von Neumann* equation with de-phasing included is given as;

$$\frac{d}{dt}\rho = -\frac{i}{\hbar}[H, \rho] - \Gamma\rho \quad (7.6)$$

$$\frac{d}{dt}\rho = -\frac{i}{\hbar}[H_0, \rho] + \frac{i}{\hbar}\mu.E\rho - \Gamma\rho \quad (7.7)$$

The above equation can be casted into a matrix equation with the relevant matrices being;

$$H_0 = \begin{pmatrix} \varepsilon_a & 0 & 0 \\ 0 & \varepsilon_b & 0 \\ 0 & 0 & \varepsilon_c \end{pmatrix} \quad (7.8)$$

$$\mu.E = \begin{pmatrix} 0 & -\mu_{ab}E & -\mu_{ac}E \\ -\mu_{ab}^*E & 0 & -\mu_{bc}E \\ -\mu_{ac}^*E & \mu_{bc}^*E & 0 \end{pmatrix} \quad (7.9)$$

$$\Gamma = \begin{pmatrix} 0 & \gamma_{ab} & \gamma_{ac} \\ \gamma_{ab}^* & 0 & \gamma_{bc} \\ \gamma_{ac}^* & \gamma_{bc}^* & 0 \end{pmatrix} \quad (7.10)$$

The dipole matrix elements between different electronic levels is related to oscillator strength ( $f$ ) which can be retrieved experimentally by measuring the absorption spectrum of Xe or electron scattering rates[98].

$$f_{ab} = \frac{2m_e}{3\hbar^2}(E_b - E_a)|\mu_{ab}|^2 \quad (7.11)$$

The dipole matrix elements for the states interfering with the resonant emission from the three electronic levels can be found from the above relation. The following tables list the observed quantum beats and their corresponding excited states for the three electronic levels, the angular momentum quantum number of each state is mentioned in the parenthesis. Theoretical modelling following the above formulation in a V-like seven level atom where all the states decay to a common ground state and are coupled to each other by dipole matrix elements reproduce well the experimental results. All the observed quantum interferences for the three electronic states can be reproduced theoretically.

Beat Frequency	Corresponding excited state
1.241 eV	9.685 eV (J=2)
2.44 eV	10.90 eV (J=2)
3.081 eV	11.49 eV (J=2)
3.515 eV	11.94 eV (J=2)

Table 7.1: Frequency of quantum interferences (column I) between electronic level at 8.43 eV with the corresponding excited states mentioned in column II.

Beat Frequency	Corresponding excited state
1.22 eV	10.90 eV (J=2)
1.468 eV	11.037 eV (J=2)
1.654 eV	11.258 eV (J=2)
2.419 eV	11.992 eV (J=2)

Table 7.2: Frequency of quantum interferences (column I) between electronic level at 9.58 eV with the corresponding excited states mentioned in column II.

Beat Frequency	Corresponding excited state
1.282 eV	11.14 eV (J=0)
1.654 eV	11.575 eV (J=2)

Table 7.3: Frequency of quantum interferences (column I) between electronic level at 9.91 eV with the corresponding excited states mentioned in column II.

## 7.4 Attosecond control over Quantum coherences

Coherent control over an outcome of light-matter interaction has remained a holy grail in modern ultrafast physics [99][100][101][102]. This control can be exercised by controlling the interference between coherently coupled quantum states by varying one of the parameters of the laser pulse. Intensity of one of the optical attosecond pulse which excites the coherence is varied whereas the weaker pulse which probes the coherence is fixed in intensity. The phase evolution of a wavepacket prepared by quantum interference between two states ( $|a\rangle$ ) and ( $|b\rangle$ ) is given by;

$$\Phi(t) = \Phi_0 + \frac{(E_b - E_a)t}{\hbar} \quad (7.12)$$

where  $\Phi_0$  being the initial phase of the coherent wavepacket (at the moment of its generation) which is superposition of states ( $|a\rangle$ ) and ( $|b\rangle$ ). The initial phase  $\Phi_0$  is varied by changing the intensity of the pulse as the moments of creation of the coherent wavepacket are different, per se for a stronger pulse coherence may be excited earlier in time compared to a weaker pulse. Discretely, phase  $\Phi(t)$  for two different intensities of pumping laser pulse will have different initial phases of the wavepacket ( $\Phi_0$ ) and additionally a different

temporal evolution of  $\frac{(E_b - E_a)t}{\hbar}$  on top of that. The amplitude of coefficients of different states in a coherent wavepacket formed by superposition of the states are also variable on change of intensity of the driving pulse. Thus, on changing the intensity of pulse exciting the quantum coherence both amplitude and phase of quantum interferences (beats) are controllable. Figure 7.7 shows the temporal modulation of spectral intensity for the excited state at 9.58 eV ( $J=1$ ) in the pump-probe spectrograms for three different pump-pulse intensities used in the experiment.

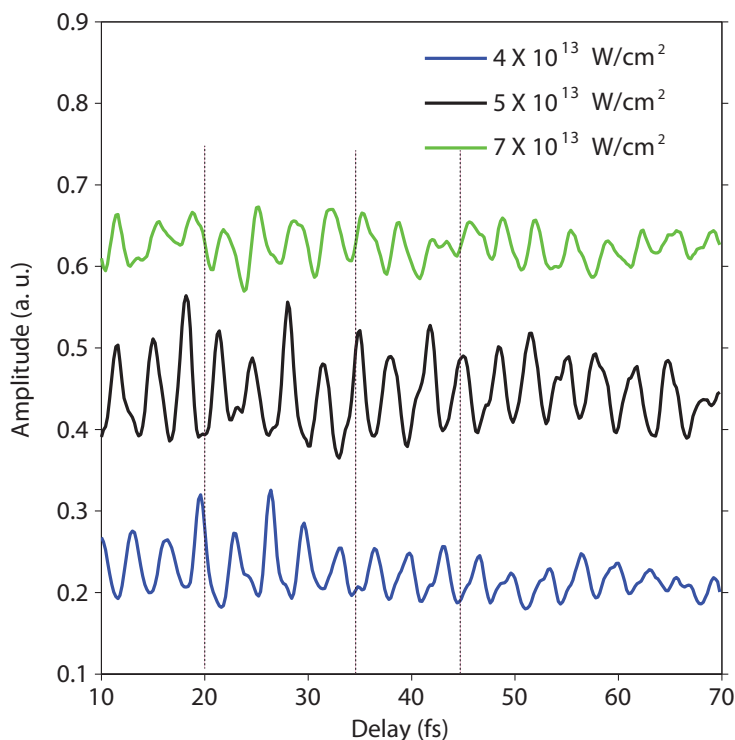


Figure 7.7: **Coherent control of Quantum interference.** Measured temporal modulation of spectral intensity for electronic state at 9.58 eV as function of delay between pump and probe pulses, three different intensities of pump-pulse (mentioned in the legend) were used in the experiment whereas the probe pulse intensity was kept constant in the measurement at  $5 \times 10^{12} \text{ W/cm}^2$ .

Temporal evolution for a particular quantum interference (between two electronic levels) can be evaluated by Fourier filtering the over all experimentally measured temporal modulation with the beat frequency corresponding to the two levels. Initial phase of the coherent wavepacket which is its phase at the moment of its generation by the optical attosecond pulse can be evaluated by fitting the filtered temporal evolution of quantum interference of two states with a cosine function of the following form;

$$\chi(t) = A \cos(\omega t + \Phi_0) \quad (7.13)$$

Initial phases extracted for interference between states at 9.58 eV and 11.2 eV which correspond to a quantum beat of 2.5 eV observed in the Quantum beat spectrogram (Figure 7.6) is shown in the following table for three different pump pulse intensities exciting the coherence.

Pump-pulse Intensity ( $W/cm^2$ )	Initial Phase (rad)
$4 \times 10^{13}$	$0.4\pi$
$5 \times 10^{13}$	$1.7\pi$
$7 \times 10^{13}$	$2.3\pi$

Table 7.4: Initial phases of quantum interference between electronic states at 9.58 eV and 11.2 eV for three different intensities of pump-pulse exciting the coherence.

## 7.5 Conclusions

In conclusion, we have demonstrated first application of a recent capability of generating optical attosecond pulses to perform time-resolved measurements of quantum interferences in a model system of Xe atoms. Also, we have shown the capability of controlling amplitude and phase of complex interference between electronic states. These experiments present first proof-of-principle experiments for time-resolved studies being triggered and probed by optical attosecond pulses in more complex quantum systems.



# Chapter 8

## Conclusions and Outlook

Emission of coherent radiation extending in frequency up to extreme ultraviolet spectral range ( $> 40$  eV) on interaction of ultrashort optical pulses with free standing polycrystalline  $\text{SiO}_2$  nanofilms has been recently demonstrated [23]. Seeking comprehension into mechanism of EUV emission from  $\text{SiO}_2$  we have performed time resolved experiments with attosecond streaking technique, one of the most accurate optical techniques. The experiments have revealed lateral motion of electrons along the energy bands of  $\text{SiO}_2$  playing the dominant role in EUV emission compared to vertical transitions of electron-hole pairs in the energy hierarchy of  $\text{SiO}_2$ . The experiments have revealed that generation mechanism of EUV emission in solids and gases are significantly different, one difference being the chirped nature of EUV emission in gases compared to concurrent (chirp free) emission in  $\text{SiO}_2$ , the other difference being the absolute temporal synchronization of EUV emission to the peak of electric field of the driving laser pulses in  $\text{SiO}_2$  in contrast to gases where they are known to be lacking synchrony with the driving laser field. Generation of first isolated attosecond pulses from solids has been demonstrated as an outcome of this work. We anticipate that it should be possible in near future to identify materials with appropriate structure or even to engineer such structures in order to maximize the nonlinearity of laser-driven coherent electron scattering in their periodic potentials and thus to enable the extension of solid-state electronics and photonics to X-ray frequencies.

Motion of electrons while it emits EUV radiation can be (probably) accessed via a time resolved photo-ionization experiment where simultaneous to the driving laser field there will be a EUV beam incident on the sample photionizing the electrons, the final kinetic energy of the electrons is dependent on its position in the dispersion profile of the energy band at the moment of ionization i.e. kinetic energy of electrons will be higher when they are at  $\Gamma$  point compared to M point in the Brillouin zone. Efforts are also currently underway to resolve real-time electron motion by a pump-probe measurement with an EUV and optical attosecond pulse, where carriers (electrons) are excited from valence to conduction bands by an EUV pulse which are then driven by an optical driver.

Emission of coherent radiation of more than 40 eV implies underlying ultrafast charge oscillations inside  $\text{SiO}_2$  of frequency as high as 10 PHz. Lateral motion of electrons leading to EUV emission is of the same nature as inside semiconductors in conventional electronics.

Establishing the fact that lateral motion of electrons in the energy bands of  $\text{SiO}_2$  results into EUV emission and helps us relate the amplitude of emitted EUV field with current density inside  $\text{SiO}_2$ . Current density inside  $\text{SiO}_2$  at central frequency of 6 PHz has been measured to be an order of magnitude higher than the previously reported value in the sub-PHz range. Also, we have shown the rise time in the dynamic conductivity to be  $\sim 30$  as. Phase coherence (field reproducibility) of isolated attosecond pulses which is inherently linked to current density inside  $\text{SiO}_2$  is demonstrated here for the first time. This is a first measurement of its kind demonstrating carrier envelope phase stability of isolated attosecond pulses. Efforts towards the characterization of absolute phase (CEP) of attosecond pulses is currently underway. These efforts have opened the avenue for studying zeptosecond resolved time dynamics of electrons in solids which is linked to the capability to induce change in CEP of EUV pulses on the order of  $\pi/20$  rad. Work is currently underway to demonstrate CEP stability and complete characterization of CEP of attosecond pulses from noble gases as well.

Dynamics of dipole coupled optically excited electron-hole pairs which essentially undergo lateral motion along the energy bands of  $\text{SiO}_2$  (emitting EUV radiation) are currently being studied by a novel nonlinear polarization based interference technique, first results from the experiments and simulations suggest presence of an ultrafast dephasing time of  $\sim 400$  as for the polarization generated by electron-hole pairs.

In this thesis I have also presented first application of intense, broadband optical attosecond pulses to study ultrafast quantum coherences in a model system of Xe atoms and demonstrated control over the initial phase of the coherent wavepacket formed after dipole coupling with laser pulses. These experiments form a firm base for future experiments seeking to resolve and control dynamics in more complex quantum systems with the unique tool of optical attosecond pulses.

# Appendix A

## Reflectivity of Au mirror and transmission curve of 150nm Al

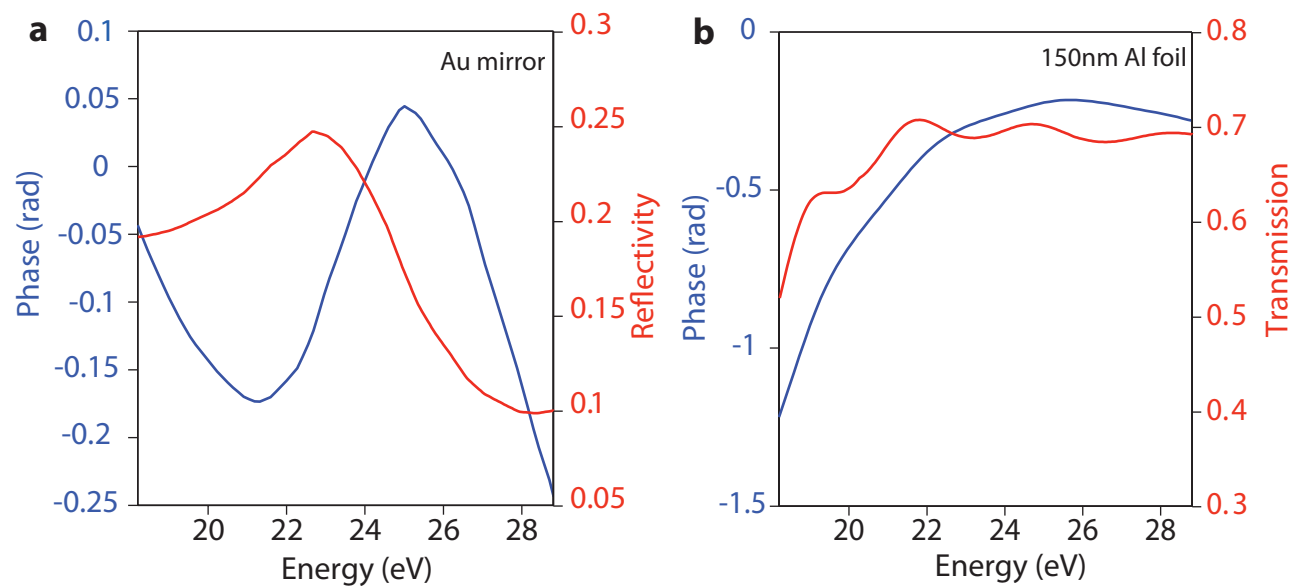


Figure A.1: **a**, Reflectivity (red line) and spectral phase (blue line) of Au coated EUV mirror. **b**, Transmission (red line) and spectral phase (blue line) of 150 nm thick Al foil.

# Appendix B

## Calibration of energy axis of TOF spectrometer

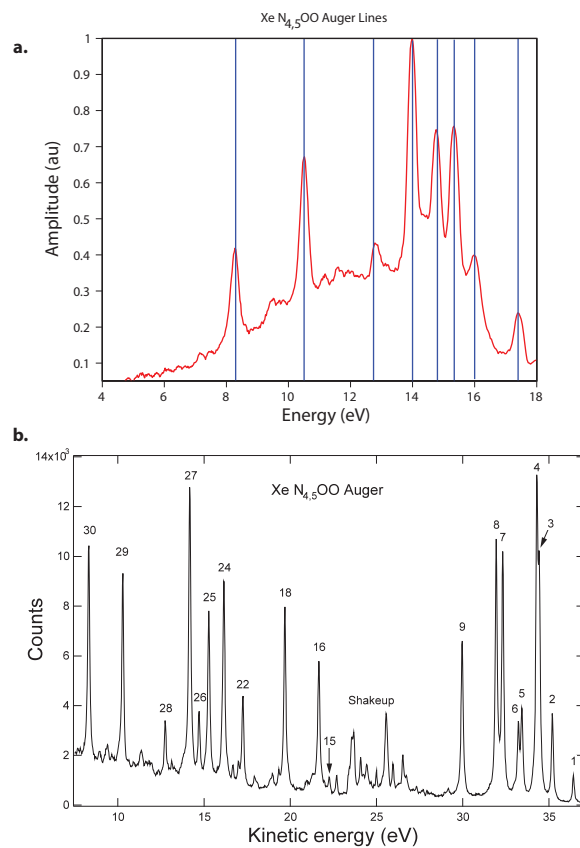


Figure B.1: **a**, Measured photoelectron spectra of Auger electrons excited by EUV photons centred at  $\sim 95$  eV in an ensemble of Xe atoms. **b**, Photoelectron spectra of Auger electrons  $N_{4,5}OO$  of Xe as measured at a synchrotron.

# Appendix C

## Methodical comparison of spectral phase from simulation and measurement set-up

Dispersion free imaging of temporal dynamics inside the SiO<sub>2</sub> nanofilms was ascertained by using less dispersive components in the measurement set-up. The spectral phases (linear part removed) of 150nm Al foil and Au coated EUV mirror[69] are shown in FigureC.1. Significant contribution to overall nonlinear spectral phase introduced in the measurement set-up comes from Al foil, the phase introduced by Au coated EUV mirror is meager. In order to determine the effect of negative group delay dispersion (GDD) introduced in the measurement by combined effect of 150nm Al foil and Au coated EUV mirror on the conclusions reached in this work, comparison of the magnitudes of GDD introduced by the measurement set-up with the expected GDD arising from two different mechanisms of EUV generation is performed. Au mirror along with Al foil introduces a negative GDD of  $\sim -2 \times 10^3 \text{as}^2$  in the measurement set-up as shown in FigureC.1. Metallic foils are known to impart negative GDD close to the absorption edge[69] ( $\sim 15$  eV for Al), this property has been extensively used to compress positively chirped attosecond pulses from noble gases. Interband contribution to EUV generation will be positively chirped as shown in Figure 4.12, calculated positive GDD coming from interband dynamics is estimated to be  $\sim 2 \times 10^4 \text{as}^2$  as shown in FigureC.1, whereas the contribution to GDD from intraband dynamics is almost negligible owing to the concurrent emission of EUV photons as explained in section. Distinctly, chirp arising from interband dynamics is an order of magnitude higher than the chirp introduced by the measurement device, which connotes if EUV generation in SiO<sub>2</sub> is dominated by interband dynamics it will not be concealed in the measurement, as is indeed the case for positively chirped EUV emission measured from Ar measured in the identical energy region shown in Figure4.3.

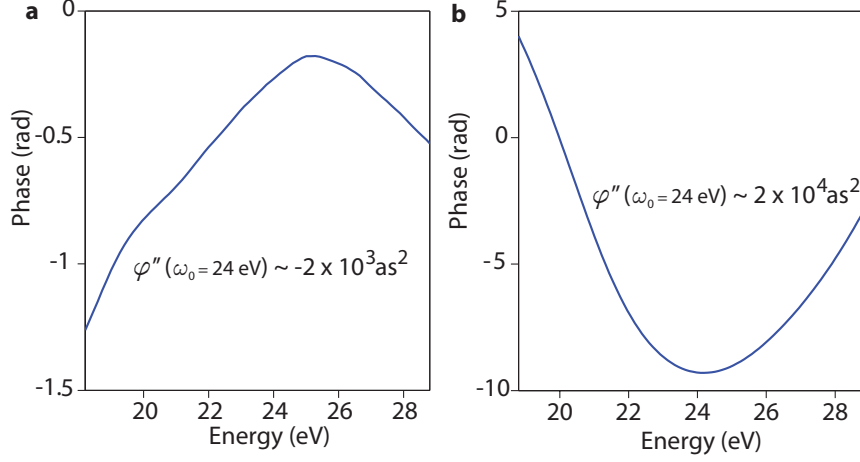


Figure C.1: **a**, Combined spectral phase of a 150nm Al foil and an Au coated EUV mirror. **b**, Calculated spectral phase of the interband contribution to EUV generation from our SBE quantum mechanical simulations.

### C.0.1 Dispersion properties of SiO<sub>2</sub>

Because SiO<sub>2</sub> exhibits a strong absorption in the EUV energy range studied in these experiments, high harmonic photons emitted from SiO<sub>2</sub> are only generated near the exit surface of the thin film and within an effective medium length commensurable with the attenuation length of EUV (18 - 29 eV) energies in SiO<sub>2</sub>. The attenuation lengths[69] for EUV radiation within the above range varies from  $\sim 8$  nm at 18 eV to 18 nm at 29 eV. Therefore, we estimate the dispersion experienced by our EUV pulses assuming a sample having a thickness of  $\sim 20$  nm. We can also neglect the criterion of phase matching in these estimations as the coherence length of the EUV radiation in the experimental region of interest is  $> 30$  nm. The GDD introduced by this 20 nm thick SiO<sub>2</sub> is approximately  $\sim 250as^2$  as shown in Figure C.2 and therefore can be neglected. Experiments in SiO<sub>2</sub> samples nearly an order of magnitude thicker experimentally verify the conclusions that indeed absorption of EUV in the solids gives rise to an effective generation length at the exit of the sample which is in principle independent of the sample thickness. Al foil and Au mirror used in our measurement set-up spectrally shape the EUV emission arising from SiO<sub>2</sub>, also they impart an additional spectral phase on the measured EUV pulses which nevertheless is marginal as shown in FigureC.3, where comparison of group delay (emission times) of EUV pulses with and without spectral phase correction from measurement set-up is shown.

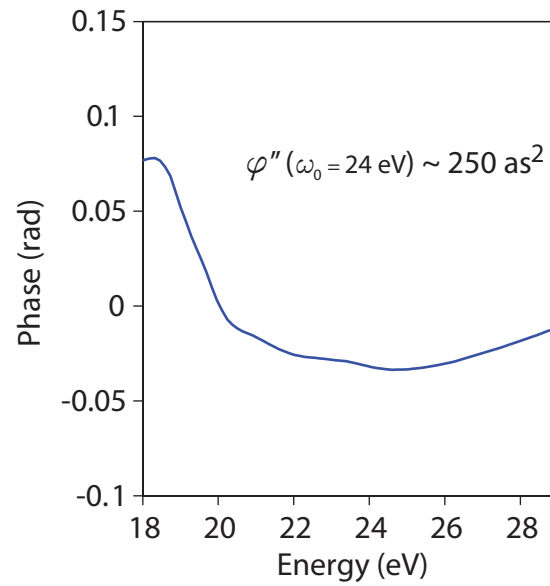


Figure C.2: Spectral phase introduced to EUV pulses in the range 18 - 29 eV by a 20 nm thick SiO<sub>2</sub> nanofilm.

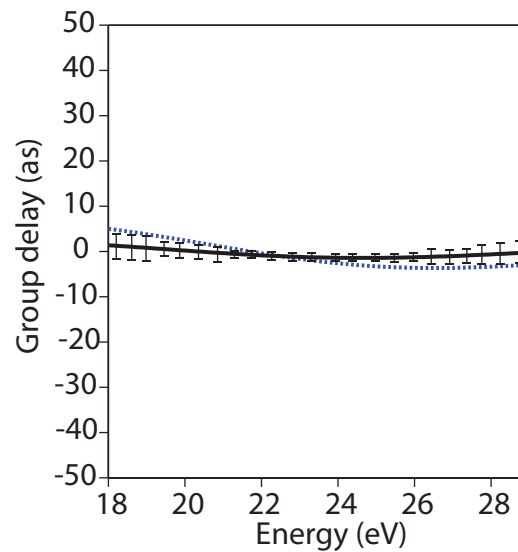


Figure C.3: Group delay of EUV pulses generated from SiO<sub>2</sub> as retrieved from experiments (blue dashed curve) and the group delay after accounting for spectral phase correction from the measurement set-up (solid black curve).

# Appendix D

## Principal Component Generalised Projections Algorithm (PCGPA)

A two dimensional spectrogram generated by letting a pulse  $E(t)$  interact with a medium concurrently with temporally sliced pieces of a gate  $G(t)$  is mathematically written as;

$$S(\omega, \tau) = \left| \int_{-\infty}^{\infty} G(t - \tau) E(t) e^{i\omega t} dt \right|^2 \quad (\text{D.1})$$

the experimental technique used to generate such spectrograms is known by Frequency Resolved Optical Gating (FROG). An iterative phase retrieval (reconstruction) algorithm can then be used extract both  $E(t)$  and  $G(t)$  from  $S(\omega, \tau)$ . The reconstruction algorithm works both for amplitude gating (nonlinear auto correlation) and phase gating as in attosecond streaking. Attosecond streaking is a phase gating technique  $G(t) = e^{i\phi(t)}$ , where  $\phi(t)$  is altered by laser fields.

### Attosecond streaking: Phase gated analogue of FROG technique

Characterization of EUV attosecond pulses require their conversion to continuum electron wavepacket by photoionization of atoms, and then driving the electronic wavepacket by laser fields to gain insights into the temporal structure of EUV fields. The aforementioned approach results into a two dimensional (2D) spectrogram of photoelectron spectra scrambled by laser fields. Within a single active electron approximation, electronic wavefunction of photoionized electrons from ground state  $|0\rangle$  to a continuum state  $|p\rangle$ , coupled by dipole matrix elements  $d_{p(t)}$  and strength of EUV field  $E_X$  in the momentum space, driven by laser fields is given by;

$$\Psi(p, \tau) = -i \int_{-\infty}^{\infty} e^{i\phi(t)} d_{p(t)} E_{EUV}(t - \tau) e^{i(W + I_P)t} dt \quad (\text{D.2})$$

$$\phi(t) = - \int_{-\infty}^{\infty} [p \cdot A(t') + A(t')^2 / 2] dt' \quad (\text{D.3})$$

As we see from the above equations, phase,  $\phi(t)$  is mainly altered by the vector potential of the laser field, hence attosecond streaking is phase gated analogue of FROG for visible pulses. An attosecond streaking spectrogram is nothing but  $|\Psi(p, \tau)|^2$ .

### Algorithm details

The first step of the iterative algorithm is to construct a spectrogram that mathematically imitates a real spectrogram. An outer product matrix ( $PG^T$ ) of a pair of discrete pulse  $P(i)$  and gate vectors  $G(j)$  followed by row shifting operation on it leads to a signal matrix  $S$ . The initial guess for the pulse can be a very broad bandwidth pulse and for gate it can be a column of unity vectors, as gate being a phase gate for attosecond streaking. The individual columns of the matrix  $S$  correspond to a composite signal of interaction between pulse and gate at a specific delay. A complex spectrogram  $\tilde{S}$  is obtained by Fourier transforming the columns of  $S$ . The crucial part of the algorithm is the application of intensity constraint between  $\tilde{S}$  and measured spectrogram  $\tilde{R}$  by the following relation;

$$\tilde{S}_{New} = \tilde{S} \sqrt{\frac{\tilde{R}}{\tilde{S}}} \quad (\text{D.4})$$

The complex spectrogram  $\tilde{S}_{New}$  resulting from this is then inverse Fourier transformed back into the time domain to get the new signal matrix  $\tilde{S}'_{New}$ . The guess for pulse and gate in the next iteration can be obtained by power method or singular value decomposition method (SVD).

$$P_{New} = \tilde{S}'_{New} \tilde{S}'_{New}{}^T P \quad (\text{D.5})$$

$$G_{New} = \tilde{S}'_{New}{}^T \tilde{S}'_{New} G \quad (\text{D.6})$$

The next signal matrix can be obtained from outer product of  $P_{New}$  and  $G_{New}$  followed by a row shifting operation on it. We can then use these vectors to construct the new signal matrix and then we iteratively repeat the above steps until we get best agreement between experimental and reconstructed spectrograms. The above mentioned steps constitute the principal component generalized projections algorithm (PCGPA), and the way of applying constraints is known as Generalized Projections, also commonly used in image processing, the steps are also summarized in the following flow chart.

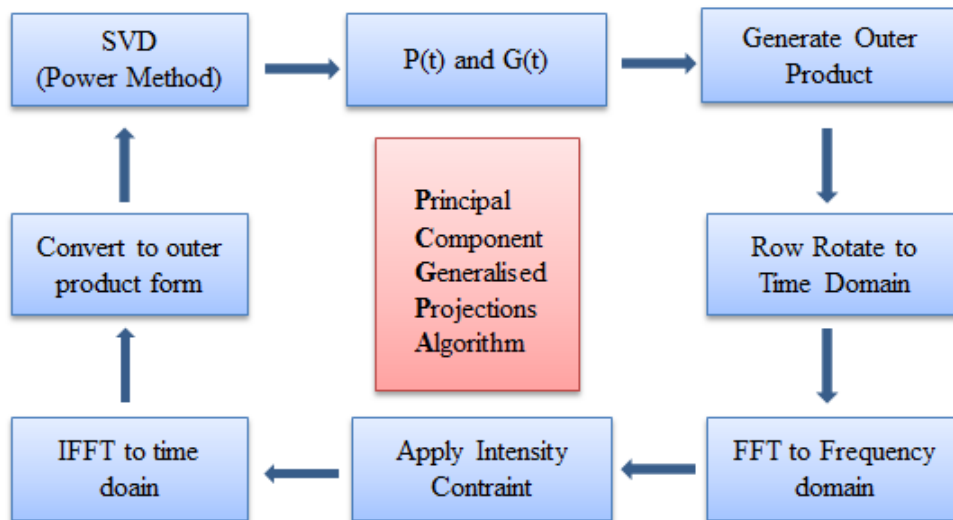


Figure D.1: PCGPA Flowchart: Description of PCGPA in reconstruction of pulse,  $P(t)$  and gate  $G(t)$  from experimental spectrograms.

# Appendix E

## Calibration of VUV spectrometer

Calibration of the energy axis of VUV spectrometer was performed with VUV emission coming from electric discharge of Deuterium  $D_2$  molecules; a comparison of VUV spectra from  $D_2$  as measured experimentally and the one pre-calibrated is shown in FigureE.1.

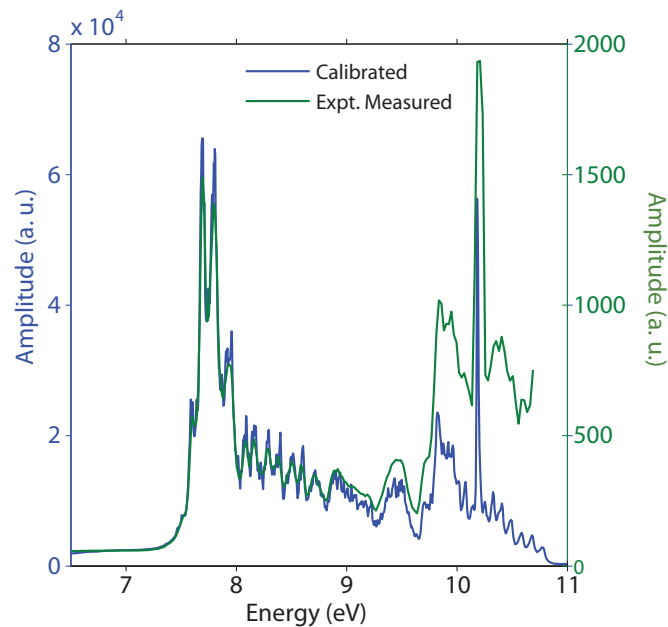


Figure E.1: Comparison of a measured spectrum from a  $D_2$  discharge tube in the VUV spectrometer with a pre-calibrated spectrum.

# Appendix F

## Data Archiving

The experimental raw data, evaluation files, and original figures can be found on the Data Archive Server of the Laboratory for Attosecond Physics at the Max Planck Institute of Quantum Optics: `/afs/rzg/mpq/lap/publication_archive`. Every figure presented in this thesis has its own folder inside the corresponding folder of the chapter incorporating the figure. All original data (`.mat`, `.dat` and `.txt` files) used to generate the figure can be found in that folder including the `.m` file for its analysis as well as an editable `.ai` figure file.

# Bibliography

- [1] T. H. Maiman, “Stimulated optical radiation in ruby,” *Nature*, vol. 187, pp. 493–494, Aug 1960.
- [2] K. Svoboda and R. Yasuda, “Principles of two-photon excitation microscopy and its applications to neuroscience,” *Neuron*, vol. 50, no. 6, pp. 823 – 839, 2006.
- [3] P. F. Moulton, “Spectroscopic and laser characteristics of ti:al2o3,” *J. Opt. Soc. Am. B*, vol. 3, pp. 125–133, Jan 1986.
- [4] A. H. Zewail, *Femtochemistry: Ultrafast Dynamics of the Chemical Bond*. 1994.
- [5] A. H. Zewail, “Femtochemistry: atomic-scale dynamics of the chemical bond,” *The Journal of Physical Chemistry A*, vol. 104, no. 24, pp. 5660–5694, 2000.
- [6] H. Niikura, F. Legare, R. Hasbani, A. D. Bandrauk, M. Y. Ivanov, D. M. Villeneuve, and P. B. Corkum, “Sub-laser-cycle electron pulses for probing molecular dynamics,” *Nature*, vol. 417, pp. 917–922, Jun 2002.
- [7] “Contributors,” in *Biological Events Probed by Ultrafast Laser Spectroscopy* (R. ALFANO, ed.), pp. ii –, Academic Press, 1982.
- [8] W. E. King, G. H. Campbell, A. Frank, B. Reed, J. F. Schmerge, B. J. Siwick, B. C. Stuart, and P. M. Weber, “Ultrafast electron microscopy in materials science, biology, and chemistry,” *Journal of Applied Physics*, vol. 97, no. 11, 2005.
- [9] M. Hentschel, R. Kienberger, C. Spielmann, G. A. Reider, N. Milosevic, T. Brabec, P. Corkum, U. Heinzmann, M. Drescher, and F. Krausz, “Attosecond metrology,” *Nature*, vol. 414, pp. 509–513, Nov 2001.
- [10] E. Goulielmakis, M. Schultze, M. Hofstetter, V. S. Yakovlev, J. Gagnon, M. Uiberacker, A. L. Aquila, E. M. Gullikson, D. T. Attwood, R. Kienberger, F. Krausz, and U. Kleineberg, “Single-cycle nonlinear optics,” *Science*, vol. 320, no. 5883, pp. 1614–1617, 2008.
- [11] M. Uiberacker, T. Uphues, M. Schultze, A. J. Verhoef, V. Yakovlev, M. F. Kling, J. Rauschenberger, N. M. Kabachnik, H. Schroder, M. Lezius, K. L. Kompa, H.-G. Muller, M. J. J. Vrakking, S. Hendel, U. Kleineberg, U. Heinzmann, M. Drescher,

- and F. Krausz, “Attosecond real-time observation of electron tunnelling in atoms,” *Nature*, vol. 446, pp. 627–632, Apr 2007.
- [12] M. Drescher, M. Hentschel, R. Kienberger, M. Uiberacker, V. Yakovlev, A. Scrinzi, T. Westerwalbesloh, U. Kleineberg, U. Heinzmann, and F. Krausz, “Time-resolved atomic inner-shell spectroscopy,” *Nature*, vol. 419, pp. 803–807, Oct 2002.
- [13] E. Goulielmakis, Z.-H. Loh, A. Wirth, R. Santra, N. Rohringer, V. S. Yakovlev, S. Zherebtsov, T. Pfeifer, A. M. Azzeer, M. F. Kling, S. R. Leone, and F. Krausz, “Real-time observation of valence electron motion,” *Nature*, vol. 466, pp. 739–743, Aug 2010.
- [14] R. Huber, F. Tauser, A. Brodschelm, M. Bichler, G. Abstreiter, and A. Leitenstorfer, “How many-particle interactions develop after ultrafast excitation of an electron-hole plasma,” *Nature*, vol. 414, pp. 286–289, Nov 2001.
- [15] P. Gaal, W. Kuehn, K. Reimann, M. Woerner, T. Elsaesser, and R. Hey, “Internal motions of a quasiparticle governing its ultrafast nonlinear response,” *Nature*, vol. 450, pp. 1210–1213, Dec 2007.
- [16] A. L. Cavalieri, N. Muller, T. Uphues, V. S. Yakovlev, A. Baltuska, B. Horvath, B. Schmidt, L. Blumel, R. Holzwarth, S. Hendel, M. Drescher, U. Kleineberg, P. M. Echenique, R. Kienberger, F. Krausz, and U. Heinzmann, “Attosecond spectroscopy in condensed matter,” *Nature*, vol. 449, pp. 1029–1032, Oct 2007.
- [17] P. Baum, D.-S. Yang, and A. H. Zewail, “4d visualization of transitional structures in phase transformations by electron diffraction,” *Science*, vol. 318, no. 5851, pp. 788–792, 2007.
- [18] C. Kealhofer, W. Schneider, D. Ehberger, A. Ryabov, F. Krausz, and P. Baum, “All-optical control and metrology of electron pulses,” *Science*, vol. 352, no. 6284, pp. 429–433, 2016.
- [19] P. B. Corkum, “Plasma perspective on strong field multiphoton ionization,” *Phys. Rev. Lett.*, vol. 71, pp. 1994–1997, Sep 1993.
- [20] J. Itatani, J. Levesque, D. Zeidler, H. Niikura, H. Pepin, J. C. Kieffer, P. B. Corkum, and D. M. Villeneuve, “Tomographic imaging of molecular orbitals,” *Nature*, vol. 432, pp. 867–871, Dec 2004.
- [21] O. Smirnova, Y. Mairesse, S. Patchkovskii, N. Dudovich, D. Villeneuve, P. Corkum, and M. Y. Ivanov, “High harmonic interferometry of multi-electron dynamics in molecules,” *Nature*, vol. 460, pp. 972–977, Aug 2009.
- [22] S. Ghimire, A. D. DiChiara, E. Sistrunk, P. Agostini, L. F. DiMauro, and D. A. Reis, “Observation of high-order harmonic generation in a bulk crystal,” *Nat Phys*, vol. 7, pp. 138–141, Feb 2011.

- [23] T. T. Luu, M. Garg, S. Y. Kruchinin, A. Moulet, M. T. Hassan, and E. Goulielmakis, “Extreme ultraviolet high-harmonic spectroscopy of solids,” *Nature*, vol. 521, pp. 498–502, May 2015.
- [24] L. Esaki and R. Tsu, “Superlattice and negative differential conductivity in semiconductors,” *IBM Journal of Research and Development*, vol. 14, pp. 61–65, Jan 1970.
- [25] J. Itatani, F. Quéré, G. L. Yudin, M. Y. Ivanov, F. Krausz, and P. B. Corkum, “Attosecond streak camera,” *Phys. Rev. Lett.*, vol. 88, p. 173903, Apr 2002.
- [26] E. Goulielmakis, M. Uiberacker, R. Kienberger, A. Baltuska, V. Yakovlev, A. Scrinzi, T. Westerwalbesloh, U. Kleineberg, U. Heinzmann, M. Drescher, and F. Krausz, “Direct measurement of light waves,” *Science*, vol. 305, no. 5688, pp. 1267–1269, 2004.
- [27] T. T. Luu, “Extreme ultraviolet high harmonic generation and spectroscopy in solids,” *LMU PhD Thesis*, 2015.
- [28] L. Keldysh, “Ionization in the field of a strong electromagnetic wave,” *JETP*, vol. 47, no. 5, p. 1307, 1965.
- [29] T. Tamaya, A. Ishikawa, T. Ogawa, and K. Tanaka, “Diabatic mechanisms of higher-order harmonic generation in solid-state materials under high-intensity electric fields,” *Phys. Rev. Lett.*, vol. 116, p. 016601, Jan 2016.
- [30] P. B. Corkum and F. Krausz, “Attosecond science,” *Nat Phys*, vol. 3, pp. 381–387, Jun 2007.
- [31] R. Kienberger, E. Goulielmakis, M. Uiberacker, A. Baltuska, V. Yakovlev, F. Bammer, A. Scrinzi, T. Westerwalbesloh, U. Kleineberg, U. Heinzmann, M. Drescher, and F. Krausz, “Atomic transient recorder,” *Nature*, vol. 427, pp. 817–821, Feb 2004.
- [32] M. B. Gaarde, J. L. Tate, and K. J. Schafer, “Macroscopic aspects of attosecond pulse generation,” *Journal of Physics B: Atomic, Molecular and Optical Physics*, vol. 41, no. 13, p. 132001, 2008.
- [33] Y. Mairesse, A. de Bohan, L. J. Frasinski, H. Merdji, L. C. Dinu, P. Monchicourt, P. Breger, M. Kovačev, R. Taïeb, B. Carré, H. G. Muller, P. Agostini, and P. Salières, “Attosecond synchronization of high-harmonic soft x-rays,” *Science*, vol. 302, no. 5650, pp. 1540–1543, 2003.
- [34] D. E. Spence, P. N. Kean, and W. Sibbett, “60-fsec pulse generation from a self-mode-locked ti:sapphire laser,” *Opt. Lett.*, vol. 16, pp. 42–44, Jan 1991.

- [35] D. J. Jones, S. A. Diddams, J. K. Ranka, A. Stentz, R. S. Windeler, J. L. Hall, and S. T. Cundiff, “Carrier-envelope phase control of femtosecond mode-locked lasers and direct optical frequency synthesis,” *Science*, vol. 288, no. 5466, pp. 635–639, 2000.
- [36] M. T. Hassan, A. Wirth, I. Grgura, A. Moulet, T. T. Luu, J. Gagnon, V. Pervak, and E. Goulielmakis, “Invited article: Attosecond photonics: Synthesis and control of light transients,” *Review of Scientific Instruments*, vol. 83, no. 11, 2012.
- [37] M. T. Hassan, T. T. Luu, A. Moulet, O. Raskazovskaya, P. Zhokhov, M. Garg, N. Karpowicz, A. M. Zheltikov, V. Pervak, F. Krausz, and E. Goulielmakis, “Optical attosecond pulses and tracking the nonlinear response of bound electrons,” *Nature*, vol. 530, pp. 66–70, Feb 2016. Letter.
- [38] M. Schultze, A. Wirth, I. Grguras, M. Uiberacker, T. Uphues, A. Verhoef, J. Gagnon, M. Hofstetter, U. Kleineberg, E. Goulielmakis, and F. Krausz, “State-of-the-art attosecond metrology,” *Journal of Electron Spectroscopy and Related Phenomena*, vol. 184, no. 36, pp. 68 – 77, 2011. Advances in Vacuum Ultraviolet and X-ray Physics The 37th International Conference on Vacuum Ultraviolet and X-ray Physics (VUVX2010).
- [39] E. Goulielmakis, V. S. Yakovlev, A. L. Cavalieri, M. Uiberacker, V. Pervak, A. Apolonski, R. Kienberger, U. Kleineberg, and F. Krausz, “Attosecond control and measurement: Lightwave electronics,” *Science*, vol. 317, no. 5839, pp. 769–775, 2007.
- [40] A. Wirth, “Attosecond transient absorption spectroscopy,” *LMU PhD Thesis*, 2011.
- [41] K. Svoboda and R. Yasuda, “Principles of two-photon excitation microscopy and its applications to neuroscience,” *Neuron*, vol. 50, no. 6, pp. 823 – 839, 2006.
- [42] S. Mukamel, *Principles of nonlinear optical spectroscopy*. 1995.
- [43] M. Ferray, A. L’Huillier, X. F. Li, L. A. Lompre, G. Mainfray, and C. Manus, “Multiple-harmonic conversion of 1064 nm radiation in rare gases,” *Journal of Physics B: Atomic, Molecular and Optical Physics*, vol. 21, no. 3, p. L31, 1988.
- [44] A. L’Huillier and P. Balcou, “High-order harmonic generation in rare gases with a 1-ps 1053-nm laser,” *Phys. Rev. Lett.*, vol. 70, pp. 774–777, Feb 1993.
- [45] G. D. Tsakiris, K. Eidmann, J. M. ter Vehn, and F. Krausz, “Route to intense single attosecond pulses,” *New Journal of Physics*, vol. 8, no. 1, p. 19, 2006.
- [46] A. K. Gupta, O. E. Alon, and N. Moiseyev, “Generation and control of high-order harmonics by the interaction of an infrared laser with a thin graphite layer,” *Phys. Rev. B*, vol. 68, p. 205101, Nov 2003.

- [47] D. Golde, T. Meier, and S. W. Koch, “High harmonics generated in semiconductor nanostructures by the coupled dynamics of optical inter- and intraband excitations,” *Phys. Rev. B*, vol. 77, p. 075330, Feb 2008.
- [48] Schubert O., Hohenleutner M., Langer F., Urbanek B., Lange C., Huttner U., Golde D., Meier T., Kira M., K. W., and Huber R., “Sub-cycle control of terahertz high-harmonic generation by dynamical Bloch oscillations,” *Nat Photon*, vol. 8, pp. 119–123, Feb 2014. Letter.
- [49] T. Higuchi, M. I. Stockman, and P. Hommelhoff, “Strong-field perspective on high-harmonic radiation from bulk solids,” *Phys. Rev. Lett.*, vol. 113, p. 213901, Nov 2014.
- [50] C. R. McDonald, G. Vampa, P. B. Corkum, and T. Brabec, “Interband Bloch oscillation mechanism for high-harmonic generation in semiconductor crystals,” *Phys. Rev. A*, vol. 92, p. 033845, Sep 2015.
- [51] G. Ndabashimiye, S. Ghimire, M. Wu, D. A. Browne, K. J. Schafer, M. B. Gaarde, and D. A. Reis, “Solid-state harmonics beyond the atomic limit,” *Nature*, vol. advance online publication, Jun 2016. Letter.
- [52] G. Vampa, T. J. Hammond, N. Thire, B. E. Schmidt, F. Legare, C. R. McDonald, T. Brabec, and P. B. Corkum, “Linking high harmonics from gases and solids,” *Nature*, vol. 522, pp. 462–464, Jun 2015. Letter.
- [53] O. Smirnova, Y. Mairesse, S. Patchkovskii, N. Dudovich, D. Villeneuve, P. Corkum, and M. Y. Ivanov, “High harmonic interferometry of multi-electron dynamics in molecules,” *Nature*, vol. 460, pp. 972–977, Aug 2009.
- [54] A. Damascelli, “Probing the electronic structure of complex systems by ARPES,” *Physica Scripta*, vol. 2004, no. T109, p. 61, 2004.
- [55] G. Vampa, T. J. Hammond, N. Thiré, B. E. Schmidt, F. Légaré, C. R. McDonald, T. Brabec, D. D. Klug, and P. B. Corkum, “All-optical reconstruction of crystal band structure,” *Phys. Rev. Lett.*, vol. 115, p. 193603, Nov 2015.
- [56] M. Hohenleutner, F. Langer, O. Schubert, M. Knorr, U. Huttner, S. W. Koch, M. Kira, and R. Huber, “Real-time observation of interfering crystal electrons in high-harmonic generation,” *Nature*, vol. 523, pp. 572–575, Jul 2015. Letter.
- [57] A. Wirth, M. T. Hassan, I. Grguraš, J. Gagnon, A. Moulet, T. T. Luu, S. Pabst, R. Santra, Z. A. Alahmed, A. M. Azzeer, V. S. Yakovlev, V. Pervak, F. Krausz, and E. Goulielmakis, “Synthesized light transients,” *Science*, vol. 334, no. 6053, pp. 195–200, 2011.

- [58] D. Golde, M. Kira, T. Meier, and S. W. Koch, “Microscopic theory of the extremely nonlinear terahertz response of semiconductors,” *physica status solidi (b)*, vol. 248, no. 4, pp. 863–866, 2011.
- [59] H. Haug and S. W. Koch, *Quantum Theory of the Optical and Electronic Properties of Semiconductors*. World Scientific, 2004.
- [60] M. Kira and S. W. Koch, *Semiconductor Quantum Optics*. World Scientific, 2012.
- [61] M. W. Feise and D. S. Citrin, “Semiclassical theory of terahertz multiple-harmonic generation in semiconductor superlattices,” *Applied Physics Letters*, vol. 75, no. 22, 1999.
- [62] P. Balcou, C. Cornaggia, A. S. L. Gomes, L. A. Lompre, and A. L’Huillier, “Optimizing high-order harmonic generation in strong fields,” *Journal of Physics B: Atomic, Molecular and Optical Physics*, vol. 25, no. 21, p. 4467, 1992.
- [63] X. He, M. Miranda, J. Schwenke, O. Guilbaud, T. Ruchon, C. Heyl, E. Georgadiou, R. Rakowski, A. Persson, M. B. Gaarde, and A. L’Huillier, “Spatial and spectral properties of the high-order harmonic emission in argon for seeding applications,” *Phys. Rev. A*, vol. 79, p. 063829, Jun 2009.
- [64] A. Baltuska, T. Udem, M. Uiberacker, M. Hentschel, E. Goulielmakis, C. Gohle, R. Holzwarth, V. S. Yakovlev, A. Scrinzi, T. W. Hansch, and F. Krausz, “Attosecond control of electronic processes by intense light fields,” *Nature*, vol. 421, pp. 611–615, Feb 2003.
- [65] M. Wegener, *Extreme Nonlinear Optics*, vol. 54. American Physical Society, 2005.
- [66] A. Cabasse, G. Machinet, A. Dubrouil, E. Cormier, and E. Constant, “Optimization and phase matching of fiber-laser-driven high-order harmonic generation at high repetition rate,” *Opt. Lett.*, vol. 37, pp. 4618–4620, Nov 2012.
- [67] E. Constant, D. Garzella, P. Breger, E. Mével, C. Dorrer, C. Le Blanc, F. Salin, and P. Agostini, “Optimizing high harmonic generation in absorbing gases: Model and experiment,” *Phys. Rev. Lett.*, vol. 82, pp. 1668–1671, Feb 1999.
- [68] E. D. Palik and G. Ghosh, *Handbook of optical constants of solids*. 1998.
- [69] B. L. Henke, E. M. Gullikson, and J. C. Davis, “X-ray interactions: photoabsorption, scattering, transmission, and reflection at  $e=50\text{--}30000$  eV,  $z=1\text{--}92$ ,” *Atomic Data and Nuclear Data Tables*, vol. 54, pp. 181–342, July 1993.
- [70] F. CAPASSO, “Band-gap engineering: From physics and materials to new semiconductor devices,” *Science*, vol. 235, no. 4785, pp. 172–176, 1987.

- [71] F. Langer, M. Hohenleutner, C. P. Schmid, C. Poellmann, P. Nagler, T. Korn, C. Schüller, M. S. Sherwin, U. Huttner, J. T. Steiner, S. W. Koch, M. Kira, and R. Huber, “Lightwave-driven quasiparticle collisions on a subcycle timescale,” *Nature*, vol. 533, pp. 225–229, May 2016. Letter.
- [72] M. Hofstetter, M. Schultze, M. Fieß, B. Dennhardt, A. Guggenmos, J. Gagnon, V. S. Yakovlev, E. Goulielmakis, R. Kienberger, E. M. Gullikson, F. Krausz, and U. Kleineberg, “Attosecond dispersion control by extreme ultraviolet multilayer mirrors,” *Opt. Express*, vol. 19, pp. 1767–1776, Jan 2011.
- [73] T. Carroll, J. Bozek, E. Kukk, V. Myrseth, L. Sthre, T. Thomas, and K. Wiesner, “Xenon n4,500 auger spectrums a useful calibration source,” *Journal of Electron Spectroscopy and Related Phenomena*, vol. 125, no. 2, pp. 127 – 132, 2002.
- [74] D. J. Kane, “Recent progress toward real-time measurement of ultrashort laser pulses,” *IEEE Journal of Quantum Electronics*, vol. 35, pp. 421–431, Apr 1999.
- [75] Y. Mairesse and F. Quéré, “Frequency-resolved optical gating for complete reconstruction of attosecond bursts,” *Phys. Rev. A*, vol. 71, p. 011401, Jan 2005.
- [76] H. Wei, A.-T. Le, T. Morishita, C. Yu, and C. D. Lin, “Benchmarking accurate spectral phase retrieval of single attosecond pulses,” *Phys. Rev. A*, vol. 91, p. 023407, Feb 2015.
- [77] M. Lewenstein, P. Balcou, M. Y. Ivanov, A. L’Huillier, and P. B. Corkum, “Theory of high-harmonic generation by low-frequency laser fields,” *Phys. Rev. A*, vol. 49, pp. 2117–2132, Mar 1994.
- [78] J. Gagnon, E. Goulielmakis, and V. Yakovlev, “The accurate frog characterization of attosecond pulses from streaking measurements,” *Applied Physics B*, vol. 92, no. 1, pp. 25–32, 2008.
- [79] “Atomistix toolkit version 2015.1.,” Feb QuantumWise A/S (www.quantumwise.com), 2015.
- [80] R. Binder and M. Lindberg, *Many-Body Effects in the Ultrafast Population Transfer in P-Doped Semiconductor Quantum Wells*, pp. 103–112. Dordrecht: Springer Netherlands, 1999.
- [81] J. R. Chelikowsky and M. Schlüter, “Electron states in  $\alpha$ -quartz: A self-consistent pseudopotential calculation,” *Phys. Rev. B*, vol. 15, pp. 4020–4029, Apr 1977.
- [82] M. V. Fischetti, D. J. DiMaria, S. D. Brorson, T. N. Theis, Kirtley, and J. R., “Theory of high-field electron transport in silicon dioxide,” *Phys. Rev. B*, vol. 31, pp. 8124–8142, Jun 1985.

- [83] M. Schultze, K. Ramasesha, C. Pemmaraju, S. Sato, D. Whitmore, A. Gandman, J. S. Prell, L. J. Borja, D. Prendergast, K. Yabana, D. M. Neumark, and S. R. Leone, “Attosecond band-gap dynamics in silicon,” *Science*, vol. 346, no. 6215, pp. 1348–1352, 2014.
- [84] K. Reimann, “Table-top sources of ultrashort thz pulses,” *Reports on Progress in Physics*, vol. 70, no. 10, p. 1597, 2007.
- [85] O. D. Mücke, “Isolated high-order harmonics pulse from two-color-driven bloch oscillations in bulk semiconductors,” *Phys. Rev. B*, vol. 84, p. 081202, Aug 2011.
- [86] M. Wu, S. Ghimire, D. A. Reis, K. J. Schafer, and M. B. Gaarde, “High-harmonic generation from bloch electrons in solids,” *Phys. Rev. A*, vol. 91, p. 043839, Apr 2015.
- [87] G. Vampa, C. R. McDonald, G. Orlando, D. D. Klug, P. B. Corkum, and T. Brabec, “Theoretical analysis of high-harmonic generation in solids,” *Phys. Rev. Lett.*, vol. 113, p. 073901, Aug 2014.
- [88] K. Leor, *High-Field Transport in Semiconductor Superlattices*. American Physical Society, 2003.
- [89] T. Hartmann, F. Keck, H. J. Korsch, and S. Mossmann, “Dynamics of bloch oscillations,” *New Journal of Physics*, vol. 6, no. 1, p. 2, 2004.
- [90] H. J. Caulfield and S. Dolev, “Why future supercomputing requires optics,” *Nat Photon*, vol. 4, pp. 261–263, May 2010.
- [91] A. Schiffrin, T. Paasch-Colberg, N. Karpowicz, V. Apalkov, D. Gerster, S. Muhlbrandt, M. Korbman, J. Reichert, M. Schultze, S. Holzner, J. V. Barth, R. Kienberger, R. Ernstorfer, V. S. Yakovlev, M. I. Stockman, and F. Krausz, “Optical-field-induced current in dielectrics,” *Nature*, vol. 493, pp. 70–74, Jan 2013.
- [92] W. Kuehn, P. Gaal, K. Reimann, M. Woerner, T. Elsaesser, and R. Hey, “Coherent ballistic motion of electrons in a periodic potential,” *Phys. Rev. Lett.*, vol. 104, p. 146602, Apr 2010.
- [93] Z. Mics, K.-J. Tielrooij, K. Parvez, S. A. Jensen, I. Ivanov, X. Feng, K. Mullen, M. Bonn, and D. Turchinovich, “Thermodynamic picture of ultrafast charge transport in graphene,” *Nat Commun*, vol. 6, Jul 2015. Article.
- [94] C. Liu, M. Reduzzi, A. Trabattoni, A. Sunilkumar, A. Dubrouil, F. Calegari, M. Nisoli, and G. Sansone, “Carrier-envelope phase effects of a single attosecond pulse in two-color photoionization,” *Phys. Rev. Lett.*, vol. 111, p. 123901, Sep 2013.

- [95] Y. Huismans, A. Rouzée, A. Gijsbertsen, J. H. Jungmann, A. S. Smolkowska, P. S. W. M. Logman, F. Lépine, C. Cauchy, S. Zamith, T. Marchenko, J. M. Bakker, G. Berden, B. Redlich, A. F. G. van der Meer, H. G. Muller, W. Vermin, K. J. Schafer, M. Spanner, M. Y. Ivanov, O. Smirnova, D. Bauer, S. V. Popruzhenko, and M. J. J. Vrakking, “Time-resolved holography with photoelectrons,” *Science*, vol. 331, no. 6013, pp. 61–64, 2011.
- [96] J. Eberly, J. Javanainen, and K. Rzaewski, “Above-threshold ionization,” *Physics Reports*, vol. 204, no. 5, pp. 331 – 383, 1991.
- [97] R. T. Carter and J. R. Huber, “Quantum beat spectroscopy in chemistry,” *Chem. Soc. Rev.*, vol. 29, pp. 305–314, 2000.
- [98] W. F. Chan, G. Cooper, X. Guo, G. R. Burton, and C. E. Brion, “Absolute optical oscillator strengths for the electronic excitation of atoms at high resolution. iii. the photoabsorption of argon, krypton, and xenon,” *Phys. Rev. A*, vol. 46, pp. 149–171, Jul 1992.
- [99] D. J. Tannor and S. A. Rice, “Control of selectivity of chemical reaction via control of wave packet evolution,” *The Journal of Chemical Physics*, vol. 83, no. 10, 1985.
- [100] W. L. Hase, S.-W. Cho, D. hong Lu, and K. N. Swamy, “The role of state specificity in unimolecular rate theory,” *Chemical Physics*, vol. 139, no. 1, pp. 1 – 13, 1989.
- [101] M. Shapiro and P. Brumer, *Strong-Field Coherent Control*. Wiley-VCH Verlag GmbH Co. KGaA, 2011.
- [102] D. J. Tannor, R. Kosloff, and S. A. Rice, “Coherent pulse sequence induced control of selectivity of reactions: Exact quantum mechanical calculations,” *The Journal of Chemical Physics*, vol. 85, no. 10, 1986.

## Acknowledgements

I would like to express my earnest gratitude to Dr. Eleftherios Goulielmakis for supervising my research work and providing me a great scientific training during these last four years of my doctoral studies. I am more than thankful to him for his endless patience in scientific discussions to overcome the obstacles I have come across during my doctoral research work. Moreover, I have learnt the virtue of optimism and continuous efforts in experiments and science in general from him.

I am grateful to Prof. Ferenc Krausz for giving me the opportunity to pursue doctoral studies in his division of Laboratory for attosecond and high field physics at Max Planck Institute of Quantum optics.

The work presented in this thesis would not have been possible without cooperation with excellent team members of the group Attoselectronics. Most of the work in this thesis has been performed in close cooperation with Dr. Minjie Zhan and Dr. Tran Trung Luu, I feel highly obliged to them for their support and would like to thank them compassionately. I would also like express my sincere thanks to Harshit Lakotia, Hee Yong Kim and Till Klostermann for being very cooperative and collegial. I also appreciate all my colleagues in the Attoselectronics group for making the environment outside the lab very friendly and filled with optimism. I am grateful to Alexander Guggenmos for his support in providing EUV optics used extensively in performing experiments reported in this thesis.

I am thankful to former members of our group Dr. Mohammed Hassan, Dr. Antoine Moulet and Dr. Julien Bertrand for their constant support and fruitful discussions in and outside the lab.

Finally, I would like to thank my parents Shri V. D. Garg and Smt. Urmila Garg, my brother Sudeep Garg whose unwavering support and encouragement made everything possible.

# Multi-petahertz electronic metrology

M. Garg<sup>1</sup>, M. Zhan<sup>1</sup>, T. T. Luu<sup>1</sup>, H. Lakhotia<sup>1</sup>, T. Klostermann<sup>1</sup>, A. Guggenmos<sup>1</sup> & E. Goulielmakis<sup>1</sup>

**The frequency of electric currents associated with charge carriers moving in the electronic bands of solids determines the speed limit of electronics and thereby that of information and signal processing<sup>1</sup>. The use of light fields to drive electrons promises access to vastly higher frequencies than conventionally used, as electric currents can be induced and manipulated on timescales faster than that of the quantum dephasing of charge carriers in solids<sup>2</sup>. This forms the basis of terahertz ( $10^{12}$  hertz) electronics in artificial superlattices<sup>2</sup>, and has enabled light-based switches<sup>3–5</sup> and sampling of currents extending in frequency up to a few hundred terahertz. Here we demonstrate the extension of electronic metrology to the multi-petahertz ( $10^{15}$  hertz) frequency range. We use single-cycle intense optical fields (about one volt per ångström) to drive electron motion in the bulk of silicon dioxide, and then probe its dynamics by using attosecond ( $10^{-18}$  seconds) streaking<sup>6,7</sup> to map the time structure of emerging isolated attosecond extreme ultraviolet transients and their optical driver. The data establish a firm link between the emission of the extreme ultraviolet radiation and the light-induced intraband, phase-coherent electric currents that extend in frequency up to about eight petahertz, and enable access to the dynamic nonlinear conductivity of silicon dioxide. Direct probing, confinement and control of the waveform of intraband currents inside solids on attosecond timescales establish a method of realizing multi-petahertz coherent electronics. We expect this technique to enable new ways of exploring the interplay between electron dynamics and the structure of condensed matter on the atomic scale.**

Although the inventor of the rectifying diode, Braun, alluded in his Nobel lecture to his unsuccessful attempts to detect light-induced electric currents inside a solid<sup>8</sup>, laser fields are now widely used to control electronic processes in the condensed phase. But whereas optical techniques<sup>9–11</sup> can induce and track electric currents in solids at frequencies nearing the petahertz (PHz) range, advancing electronic metrology to the multi-petahertz realm calls for the ability to capture the dynamics encoded in radiation emitted at frequencies extending into the extreme ultraviolet (EUV) range and beyond. Here we employ attosecond streaking<sup>6,7</sup> and photoelectron interferometry<sup>12</sup> to realize multi-petahertz metrology of solids.

Recent spectral-domain studies of laser-driven semiconductors and dielectrics have suggested that the coherent radiation emerging in these interactions (in the visible and ultraviolet<sup>13</sup>, as well as in the extreme ultraviolet<sup>14</sup>, EUV) could be directly associated with laser-induced, intraband currents in the bulk, and could therefore serve as a unique macroscopic probe of the microscopic electric currents. Nevertheless, time-resolved studies using mid-infrared and terahertz fields support a different picture; interband polarization, encapsulated in a generalized re-collision model<sup>15</sup> or the interplay<sup>16,17</sup> between interband and intraband dynamics (Fig. 1a), is essential to describe the nonlinear response of these systems. Theoretical studies<sup>15,18–21</sup> can now offer valuable insight into these interactions but their conclusions are sensitive to electronic dephasing, which is challenging to account for precisely<sup>15–17,19–22</sup>. As a result, the question of whether the emerging radiation from the laser-driven solids is linked to the

nonlinear motion of charge carriers in bands (intraband) or to the dipole induced among bands (interband) has been a subject of an escalating debate<sup>14,18,23,24</sup>. An answer to this question comprises a critical step for extending coherent electronics to the multi-petahertz realm.

To experimentally address this question, we used attosecond streaking to record the temporal profile of EUV transients generated in polycrystalline SiO<sub>2</sub> nanofilms ( $\sim 120$  nm thick) by single-cycle (precisely 1.2-cycle) optical pulses (peak field strength,  $F_0 \approx 1.1$  V Å<sup>-1</sup>) produced in a light-field synthesizer<sup>25</sup>. A streaking spectrogram recorded using our experimental set-up (Fig. 1b; see also Supplementary Information section I) and its numerical reconstruction<sup>26</sup> (Supplementary Information section II) are displayed in Fig. 1c and d, respectively. The reconstruction reveals an isolated attosecond EUV pulse, as shown in Fig. 1e, with a duration of  $\tau_{\text{EUV}} \approx 470$  as measured at the full-width at half-maximum (FWHM) of its intensity profile; this duration is only slightly longer than the bandwidth-limited value ( $\tau_{\text{BL}} \approx 460$  as) and is precisely synchronized to the peak of the driving field. The retrieved spectral phase and spectrum of the attosecond burst are presented in Fig. 1f.

To identify the physical mechanism underlying the nonlinear EUV emission in SiO<sub>2</sub>, we performed time–frequency analysis (see Supplementary Information section III) of the retrieved attosecond pulse presented in Fig. 1e, as shown in Fig. 2b. We then compared the results with the nonlinear dipoles obtained through the numerical solution of the semiconductor Bloch equations (SBEs)<sup>19–21</sup> in SiO<sub>2</sub> including Coulomb interactions among the carriers<sup>21</sup> and using parameters identical to those in our experiments, such as the retrieved optical field waveform and its strength (Fig. 1e) (see also Supplementary Information section III).

In contrast to earlier SBE modelling of SiO<sub>2</sub> under intense ultrafast fields<sup>14</sup>, the incorporation of Coulomb interaction<sup>21</sup> and the tuning of its strength to reproduce the exciton response of SiO<sub>2</sub> (see Supplementary Information section VI) results in the dominance of the intraband contribution (Fig. 2a, green line) over the interband contribution (Fig. 2a, orange line). Importantly however, the genuine temporal dynamics associated with each of these contributions, earlier identified as macroscopic markers of the physics of the emission<sup>15,18</sup>, are virtually immune to Coulomb interactions under the conditions of this study (see Supplementary Information section VI). Indeed, interband dynamics gives rise to a positively chirped spectral response (Fig. 2c): that is, EUV photons of different energies are emitted at distinct moments following the excitation of carriers into the bands, their acceleration and their subsequent re-collision<sup>15</sup>. By contrast, the contribution of the intraband current yields a virtually concurrent spectral emission (Fig. 2d), which is typical of the nonlinear scattering of a particle in a non-parabolic band, giving rise to a nearly chirp-free EUV dipole synchronized to the peak of the driving field. As the total emission is dominated by the intraband current contribution (Fig. 2a), the chirp of the total EUV dipole (Fig. 2e) is virtually determined by the intraband current.

A comparison between the experimentally traced dynamics (Fig. 2b) and those evaluated for the intraband contribution (Fig. 2d)

<sup>1</sup>Max-Planck-Institut für Quantenoptik, Hans-Kopfermann-Strasse 1, D-85748 Garching, Germany.

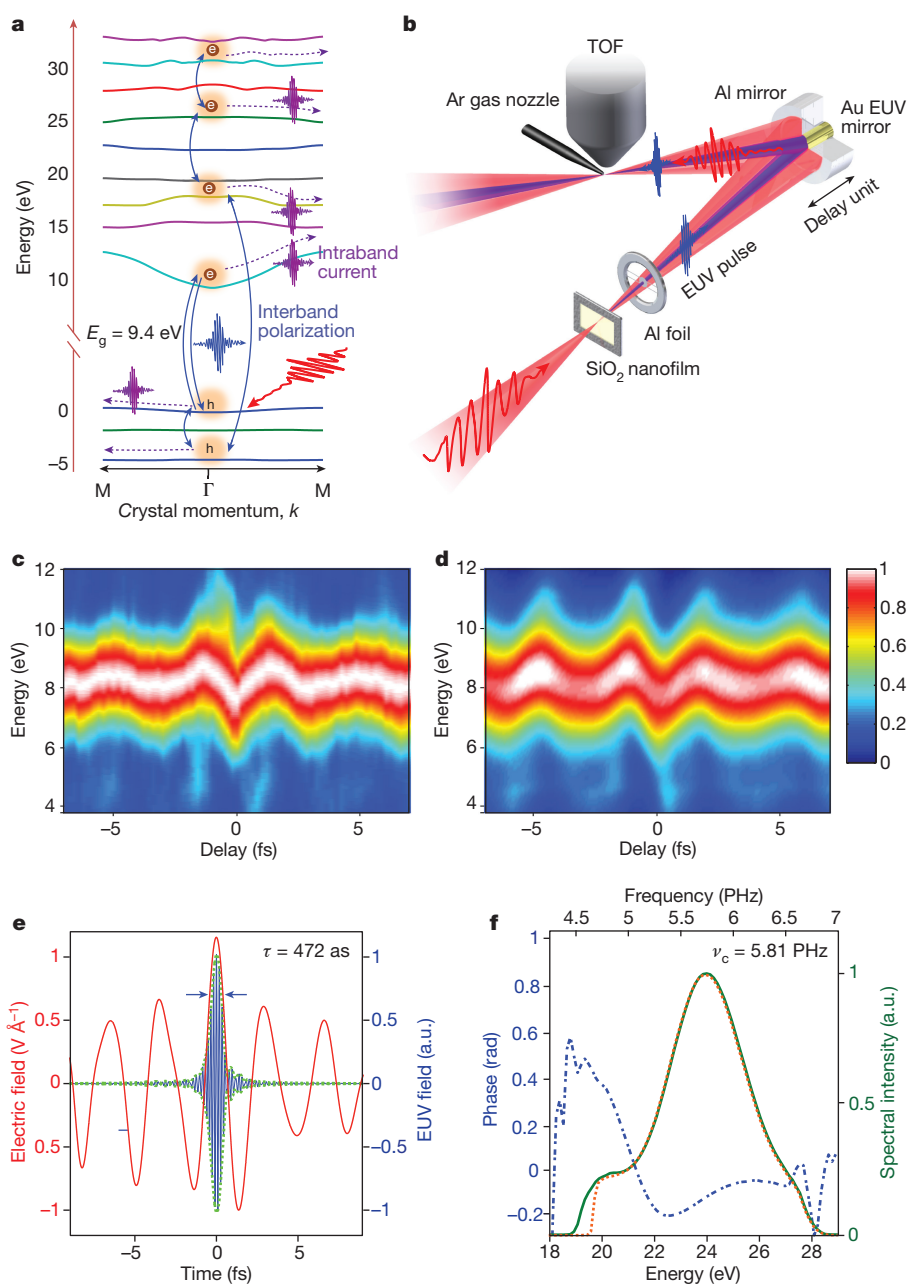


**Figure 1 | Attosecond pulse metrology in bulk SiO<sub>2</sub>.** **a**, Intraband and interband dynamics in optically driven SiO<sub>2</sub> and emission of extreme ultraviolet (EUV) radiation. Intraband currents are induced via the field-driven motion and scattering of electrons (e) and holes (h) along the dispersive band profiles. Dipole coupling between different bands gives rise to an interband contribution to the emitted radiation. **b**, SiO<sub>2</sub> nanofilms ( $\sim 120$  nm) are exposed to intense single-cycle optical fields (peak field strength,  $F_0 \approx 1.1 \text{ V \AA}^{-1}$ ) to generate coherent EUV radiation. A disk-shaped thin Al nanofilm and a concentric two-component, concave mirror-assembly (Al outer, Au inner) allow the spatiotemporal separation of optical and generated EUV pulses as well as their focusing onto an Ar gas jet. A time-of-flight (TOF) spectrometer records photoelectron

spectra generated in Ar as a function of the delay between EUV and the optical pulse. Access to the timing between EUV and optical field at the source is enabled via the absolute delay calibration of the two-component mirror assembly ('delay unit') via a high order autocorrelation of the optical beam (see Supplementary Information section I). **c**, Measured and **d**, reconstructed streaking spectrograms; colour scale represents photoelectron counts in arbitrary units. **e**, Retrieved EUV (blue) and optical (red line) pulse profiles, dashed green line shows the envelope of EUV pulse. **f**, Retrieved spectral phase (blue dashed line) and spectrum (orange dashed line) of the EUV pulse. Green curve indicates the spectrum of the EUV pulse in the absence of the optical probe.

and total polarization (Fig. 2e) reveals a striking agreement, highlighted by the precise synchrony of the peak of the EUV emission with the single intense crest of the optical field and the weak temporal chirp of the generated EUV transients. In contrast, the dynamics of the interband contribution (Fig. 2c) fail to capture the measured attosecond response of the system. A spectrogram (Fig. 2f) simulated using a semiclassical approach (Supplementary Information section IV), in which a pre-excited electron is scattered along the texture of the first conduction

band in the  $\Gamma$ -M direction of a SiO<sub>2</sub> crystal<sup>14</sup>, also yields a very good agreement with the experiment.

A detailed comparison with the experimental results (Fig. 2g, black line) of the group delays (emission times) evaluated from the interband contribution (Fig. 2g, orange line), the intraband current (Fig. 2g, green line) and the total dipole (Fig. 2g, orange dashed line) further strengthens the above conclusions, and enables the visualization of the finer details of the dynamic response of the system to the optical

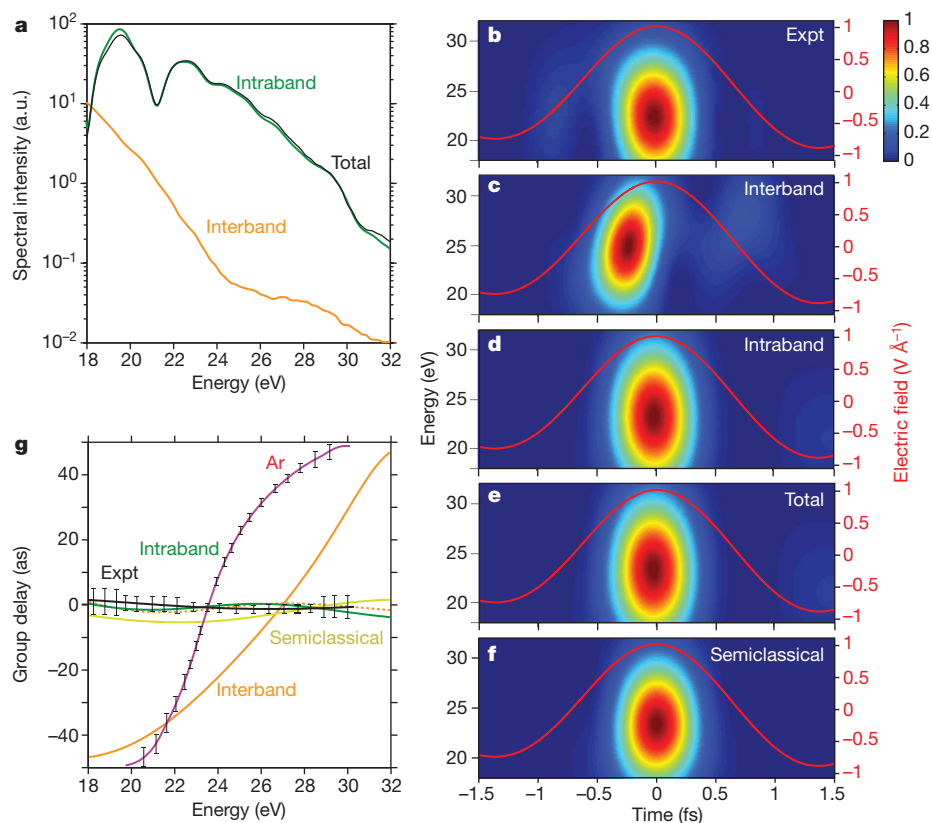


**Figure 2 | Interband versus intraband dynamics in SiO<sub>2</sub>.** **a**, EUV spectra in SiO<sub>2</sub> associated with interband and intraband contributions, and total polarization simulated for the measured optical field shown in Fig. 1e. **b–f**, Time–frequency spectrograms of EUV pulses: **b**, measured in our experiments (Fig. 1e), **c**, interband contribution, **d**, intraband contribution, **e**, total polarization, and **f**, the semiclassical model used in our simulations. Red lines represent the driving electric field (right-

hand y axis). Spectral intensity is shown with the colour scale in arbitrary units. **g**, Retrieved group delays of the EUV emission in SiO<sub>2</sub> ('Expt'; black line) and Ar gas (violet line); standard error in the retrieved group delay is presented with error bars. Shown are group delays of the emission associated with the interband contribution (orange line), the intraband contribution (green line) and total polarization (orange dashed curve), and as modelled using a semiclassical approach (yellow line).

field. Our measurements reveal a weak but statistically significant chirp in the EUV emission that matches the chirp predicted for the intraband current in SBEs and the semiclassical model. Experiments under identical conditions performed in Ar (see also Supplementary Information section I) reproduced earlier recognized chirp-dynamics of gas-phase EUV emission<sup>27,28</sup>, as shown in Fig. 2g (violet curve), which is in very good agreement with the predictions of semiclassical theory (Supplementary Fig. 10) and serve here as a benchmark of the temporal resolution of our apparatus. Additional measurements in crystalline SiO<sub>2</sub> (see Supplementary Information section VII) as well as measurements performed at different field strengths of the optical driver further substantiate the above conclusions (see Supplementary Information section V).

In a second set of experiments, we probe the nonlinearity of the emission process directly in the time domain, by using attosecond streaking to trace the temporal structure of EUV bursts generated by single-cycle pulses whose carrier envelope phase ( $\varphi_{CE}$ ) is adjusted to produce near-cosine and near-sine waveforms (white lines in Fig. 3a, b). The contrast in field strengths between the two most intense half-cycles in each of these waveforms was 1.6 to 1 (Fig. 3a) and 1.16 to 1 (Fig. 3b), respectively. For both the above driving waveforms the experiments reveal the emergence of an isolated burst of radiation (Fig. 3c, d), which is precisely synchronized to their most intense field crest. This feature is well reproduced in our simulations by intraband current (Fig. 3e, f, green lines) and total polarization (Fig. 3g, h), and it is compatible with the findings of previous time-integrated studies<sup>14</sup> in which an  $\sim F^{18}$  scaling of the EUV emission versus the electric field of the driving pulse ( $F$ ) was identified. Based on that nonlinearity, a contrast of several orders of magnitude between main and satellite burst is predicted for

both  $\varphi_{CE}$  values studied here, in agreement with our experiments. The onset and disappearance of a pulse pedestal (Fig. 3c, d, black arrows) is compatible with a  $\varphi_{CE}$ -induced spectral shaping of the EUV emission and is well reproduced by our theoretical modelling via intraband dynamics (Fig. 3e, f; see also Supplementary Information section VIII). This dynamic variation of properties of the EUV pulse via the  $\varphi_{CE}$  of the driver demonstrates the capability of controlling the frequency and the time structure of the laser-induced electric current in a solid. Dynamics pertaining to the interband contribution in our model suggest the generation of a single EUV burst for the near-cosine pulse (Fig. 3e) but also the formation of a sizable satellite burst for a near-sine pulse (Fig. 3f); both are generated at a time offset with respect to the peaks of the driving fields, as presented in Fig. 3e, f. These dynamics bear a similarity to those revealed in  $\varphi_{CE}$  studies of EUV pulse generation in gases at the single-cycle limit<sup>28</sup>, but do not match the experimental findings of the present study.

Attosecond streaking has thus far provided direct access to the envelope and frequency sweep (chirp) of the multi-petahertz electric currents, but the establishment of multi-petahertz electronics requires access to, and confirmation of, the phase coherence of these currents: that is, the reproducibility of their instantaneous waveform from pulse to pulse and immunity of this waveform to  $\varphi_{CE}$  fluctuations of the optical driver. So far, access to the phase coherence of EUV pulse trains has been demonstrated in gases<sup>29</sup>, but in solids, and at the isolated attosecond pulse limit, phase coherence has remained unexplored. To study the waveform reproducibility of our EUV pulses, we have employed an earlier proposed methodology<sup>12</sup> in which  $\varphi_{CE}$  dynamics can be accessed via the interference in photoelectron spectra, generated in a gas jet (here Ar) via the direct photoionization by the EUV pulse

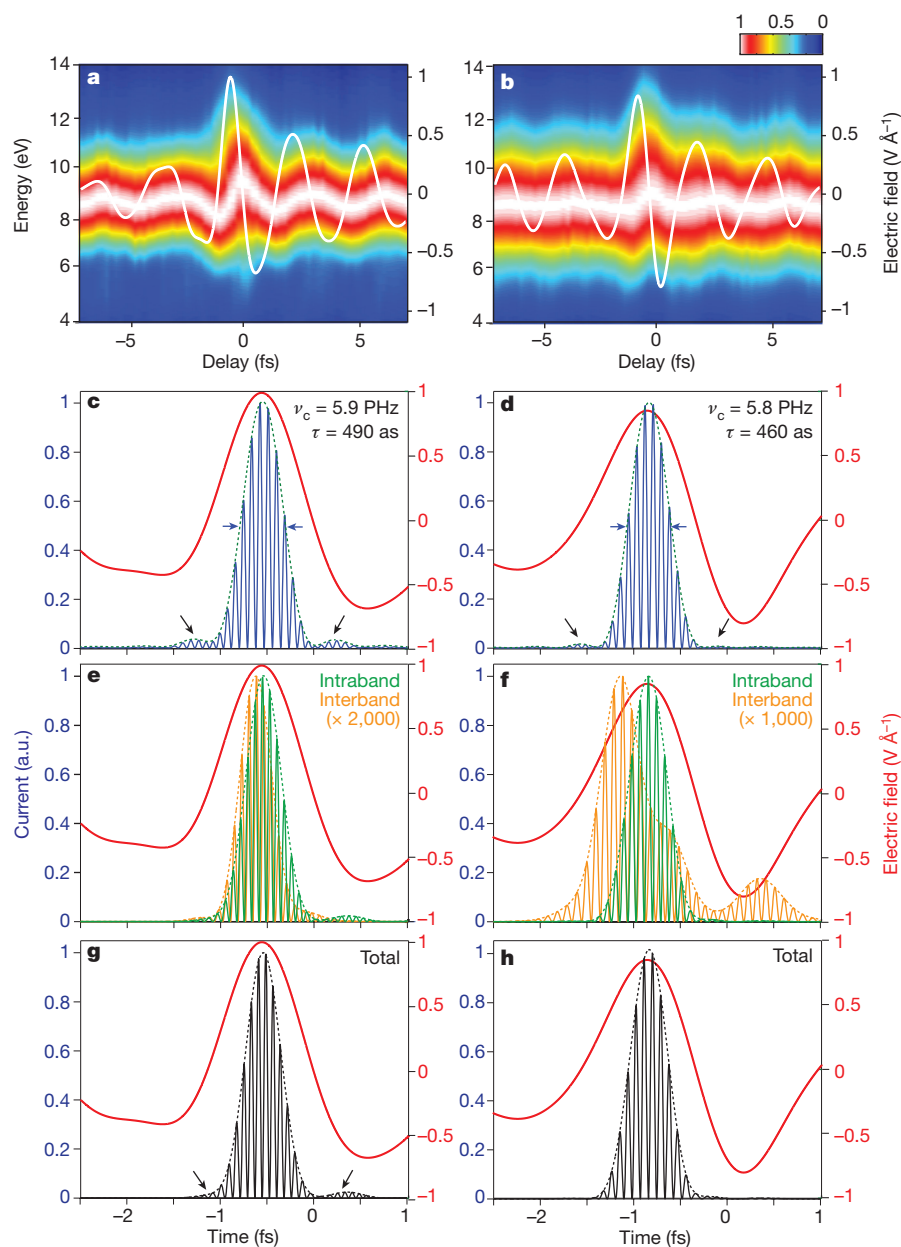


**Figure 3 | Control of multi-petahertz currents in SiO<sub>2</sub>.** **a, b**, Attosecond streaking spectrograms recorded for two  $\varphi_{CE}$  settings of the single-cycle driving pulse (white lines; right-hand y axis), differing by  $\sim\pi/2$  rad; colour scale shows photoelectron counts in arbitrary units. **c, d**, EUV transients (instantaneous intensity) retrieved from the spectrograms shown in **a** and **b**, respectively. Blue and red lines represent the intensity profile and field waveform of EUV transients and optical driver respectively, green dashed curve shows the envelope of EUV transients.  $\nu_c$  and  $\tau$  are carrier frequency and pulse duration of the EUV transients respectively. **e, f**, Instantaneous intensity profiles of EUV pulses predicted for the intraband contribution (green curve) in our simulation for experimentally recorded optical waveforms (red lines). Interband contributions (orange line) are scaled in **e, f**, to ease comparison with intraband contributions (green line). **g, h**, Total polarization dynamics (black lines) simulated for the two driving waveforms (red lines). Black arrows highlight the temporal features in EUV transients in **c** and **g**.

and through above-threshold ionization (ATI) by the optical field (see Supplementary Information, section X). Figure 4a shows such interference fringes recorded over a time period of 15 min. The  $\varphi_{CE}$  stability evaluated from the interference pattern (Fig. 4b) was better than  $\sim\pi/10$  rad, as displayed in Fig. 4c, implying that the EUV waveform and thus that of the intraband current are reproducible with an accuracy better than one-twentieth of their carrier period. Detailed control of the  $\varphi_{CE}$  phase of the EUV pulses (see Supplementary Information section X) further verifies the accuracy of our approach. For a nonlinear medium with a length less than the driving pulse wavelength, the field profiles of the EUV pulse and that of the intraband current are related as:  $E_{EUV}(t) \propto J(t)$  (see Supplementary Information section XI). As a result, the EUV fields displayed in Fig. 1e, Fig. 3a, b and Supplementary Fig. 17 comprise the first demonstration of the use of optical pulses to generate, measure, confine (at the attosecond level) and control waveform-reproducible multi-petahertz currents in solids.

To gain quantitative insight into the electronic properties of SiO<sub>2</sub> in the multi-petahertz regime, we measured the photon yield of the emitted EUV light, which in turn allowed us to evaluate the amplitude of  $E_{EUV}(t)$  in the bulk of SiO<sub>2</sub> (see Supplementary Information section XI) as well as the nonlinear current density in our sample as shown

in Fig. 4d. The current density reaches values of  $\sim 10^{11}$  A m<sup>-2</sup>, which is approximately an order of magnitude higher than earlier efforts in sub-petahertz ranges<sup>3</sup>. The dynamic nonlinear conductivity<sup>30</sup>  $\sigma(t)$  shown in Fig. 4e, which is evaluated from the precise knowledge of driving optical field  $F(t)$ , current density profile  $j(t)$  and their relative timing as  $\sigma(t) = j(t)/F(t)$ , builds up within approximately  $\sim 0.7$  fs and switches periodically at the frequency of the generated EUV field: that is, it turns on and off within approximately  $\sim 30$  as (Fig. 4e inset). Negative values of the dynamic conductivity imply that electrons move in opposite directions with respect to the applied field force every second half cycle of their oscillation (Fig. 4e); such a regime was earlier recognized in intraband coherent electron motions in semiconductor superlattices<sup>2</sup>, and is here extended into the multi-petahertz range.

Identifying, measuring in real-time and controlling multi-petahertz intraband electric currents in solids, and similarly understanding the dynamic electronic properties of solids in the multi-petahertz regime, opens up new prospects of study and applications at the interface of photonics and electronics. Owing to the high sensitivity of these currents to the atomic-scale structure of materials (which in turn dictates the details of the dispersion profiles of the electronic bands<sup>14</sup>), laser-induced intraband currents and their probing via the emitted

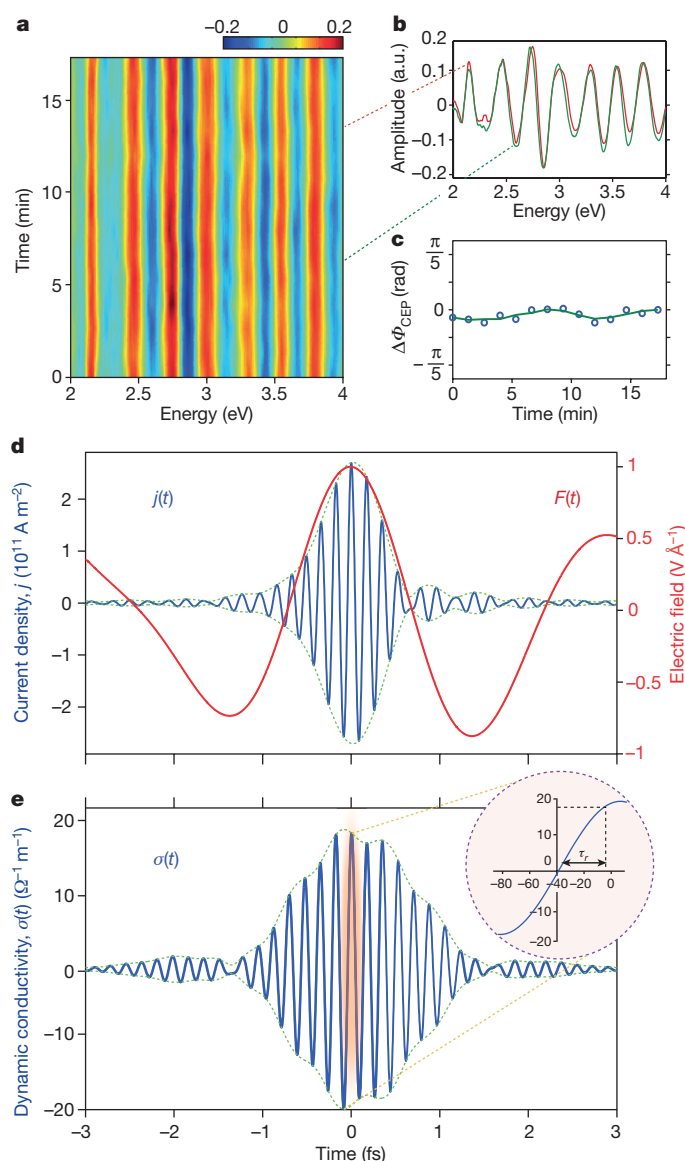


**Figure 4 | Phase coherence of multi-petahertz currents and the dynamic conductivity of SiO<sub>2</sub>.** **a**, Spectral interference between ATI and EUV photoelectrons in Ar, recorded for a time period of  $\sim 15$  min, colour scale represents spectral intensity in arbitrary units. **b**, Interference pattern (red and green lines) at two representative instances of the measurement in **a**. **c**, Evaluated  $\varphi_{\text{CEP}}$  (blue circles) variation of the EUV pulse (and the corresponding intraband current), green line is to guide the eye. **d**, Nonlinear current density,  $j(t)$  (blue curve). Red curve shows the driving optical field,  $F(t)$ , green dashed curve shows the envelope of  $j(t)$ . **e**, Induced nonlinear dynamic conductivity  $\sigma(t)$  in SiO<sub>2</sub> (blue curve). Inset highlights the rapid switching of the conductivity within  $\tau_r \approx 30$  as. Vertical axis, as main panel; horizontal axis, time in as.

EUV transients may soon enable direct probing of the periodic potentials of solids.

Received 26 February; accepted 30 August 2016.

1. Caulfield, H. J. & Dolev, S. Why future supercomputing requires optics. *Nat. Photon.* **4**, 261–263 (2010).
2. Leo, K. *High-Field Transport in Semiconductor Superlattices* (Springer, 2003).
3. Schiffrin, A. *et al.* Optical-field-induced current in dielectrics. *Nature* **493**, 70–74 (2012).

4. Krüger, M., Schenk, M. & Hommelhoff, P. Attosecond control of electrons emitted from a nanoscale metal tip. *Nature* **475**, 78–81 (2011).
5. Somma, C., Reimann, K., Flytzanis, C., Elsaesser, T. & Woerner, M. High-field terahertz bulk photovoltaic effect in lithium niobate. *Phys. Rev. Lett.* **112**, 146602 (2014).
6. Itatani, J. *et al.* Attosecond streak camera. *Phys. Rev. Lett.* **88**, 173903 (2002).
7. Goulielmakis, E. *et al.* Direct measurement of light waves. *Science* **305**, 1267–1269 (2004).
8. Braun, F. Electrical oscillations and wireless telegraphy. In *Nobel Lectures, Physics 1901–1921* (Elsevier, 1967).
9. Gaal, P. *et al.* Internal motions of a quasiparticle governing its ultrafast nonlinear response. *Nature* **450**, 1210–1213 (2007).
10. Huber, R. *et al.* How many-particle interactions develop after ultrafast excitation of an electron-hole plasma. *Nature* **414**, 286–289 (2001).
11. Gudde, J., Rohleder, M., Meier, T., Koch, S. W. & Hofer, U. Time-resolved investigation of coherently controlled electric currents at a metal surface. *Science* **318**, 1287–1291 (2007).
12. Liu, C. D. *et al.* Carrier-envelope phase effects of a single attosecond pulse in two-color photoionization. *Phys. Rev. Lett.* **111**, 123901 (2013).
13. Ghimire, S. *et al.* Observation of high-order harmonic generation in a bulk crystal. *Nat. Phys.* **7**, 138–141 (2011).
14. Luu, T. T. *et al.* Extreme ultraviolet high-harmonic spectroscopy of solids. *Nature* **521**, 498–502 (2015).
15. Vampa, G. *et al.* Linking high harmonics from gases and solids. *Nature* **522**, 462–464 (2015).
16. Hohenleutner, M. *et al.* Real-time observation of interfering crystal electrons in high-harmonic generation. *Nature* **523**, 572–575 (2015).
17. Schubert, O. *et al.* Sub-cycle control of terahertz high-harmonic generation by dynamical Bloch oscillations. *Nat. Photon.* **8**, 119–123 (2014).
18. Wu, M. X., Ghimire, S., Reis, D. A., Schafer, K. J. & Gaarde, M. B. High-harmonic generation from Bloch electrons in solids. *Phys. Rev. A* **91**, 043839 (2015).
19. Kira, M. & Koch, S. W. *Semiconductor Quantum Optics* (Cambridge Univ. Press, 2012).
20. Golde, D., Meier, T. & Koch, S. W. High harmonics generated in semiconductor nanostructures by the coupled dynamics of optical inter- and intraband excitations. *Phys. Rev. B* **77**, 075330 (2008).
21. Haug, H. & Koch, S. W. *Quantum Theory of the Optical and Electronic Properties of Semiconductors* 5th edn (World Scientific, 2009).
22. Schultze, M. *et al.* Attosecond band-gap dynamics in silicon. *Science* **346**, 1348–1352 (2014).
23. McDonald, C. R., Vampa, G., Corkum, P. B. & Brabec, T. Interband Bloch oscillation mechanism for high-harmonic generation in semiconductor crystals. *Phys. Rev. A* **92**, 033845 (2015).
24. Tamaya, T., Ishikawa, A., Ogawa, T. & Tanaka, K. Diabatic mechanisms of higher-order harmonic generation in solid-state materials under high-intensity electric fields. *Phys. Rev. Lett.* **116**, 016601 (2016).
25. Hassan, M. T. *et al.* Optical attosecond pulses and tracking the nonlinear response of bound electrons. *Nature* **530**, 66–70 (2016).
26. Mairesse, Y. & Quere, F. Frequency-resolved optical gating for complete reconstruction of attosecond bursts. *Phys. Rev. A* **71**, 011401(R) (2005).
27. Corkum, P. B. Plasma perspective on strong-field multiphoton ionization. *Phys. Rev. Lett.* **71**, 1994–1997 (1993).
28. Goulielmakis, E. *et al.* Single-cycle nonlinear optics. *Science* **320**, 1614–1617 (2008).
29. Benko, C. *et al.* Extreme ultraviolet radiation with coherence time greater than 1 s. *Nat. Photon.* **8**, 530–536 (2014).
30. Mics, Z. *et al.* Thermodynamic picture of ultrafast charge transport in graphene. *Nat. Commun.* **6**, 7655 (2015).

Supplementary Information is available in the online version of the paper.

**Acknowledgements** This work was supported by a European Research Council grant (Attoelectronics-258501), the Deutsche Forschungsgemeinschaft Cluster of Excellence, Munich Centre for Advanced Photonics, the Max Planck Society and the European Research Training Network MEDEA.

**Author Contributions** M.G. and M.Z. conducted the experiments; E.G. planned the experiments and supervised the project; M.G., H.L., T.K., T.T.L. and A.G. conducted the simulations; and M.G. and E.G. interpreted the experimental data and contributed to the preparation of the manuscript.

**Author Information** Reprints and permissions information is available at [www.nature.com/reprints](http://www.nature.com/reprints). The authors declare no competing financial interests. Readers are welcome to comment on the online version of the paper. Correspondence and requests for materials should be addressed to E.G. (elgo@mpq.mpg.de).

**Reviewer Information** Nature thanks M. Chini, U. Höfer and the other anonymous reviewer(s) for their contribution to the peer review of this work.

# Curriculum Vitae

## Manish Garg

Phone: (+49) 8932905751

Mobile: (+49)15145528228

Max Planck Institute of Quantum Optics

Laboratory for Attosecond and High-Field Physics

Hans-Kopfermann Str. 1

D-85748 Garching, Germany

January 26, 2017

E-mail: manish.garg@mpq.mpg.de

manishgargiiserk@gmail.com

Web: www.attoworld.de

## Personal

Born: 2<sup>nd</sup> July, 1988, Shahdol, India

Status: Single

Citizenship: Indian

## Education

- **Max Planck Institute for Quantum Optics** Garching, Germany  
*PhD* . . . . . *Nov. 2012 - till date*
- **Indian Institute of Science Education and Research** Kolkata, India  
*Integrated B.S. - M.S.* . . . . . *2007 - 2012*  
 – Thesis: Quantum Dynamics in Ultrashort Intense Laser Pulses

## Grants & Scholarsips

- **INSPIRE Fellowship, Department of Science and Technology, India**  
*Integrated B.S. - M.S.* . . . . . *2007 - 2012*
- **IMPRS - APS**  
*PhD* . . . . . *Nov. 2012 - till date*
- **DAAD-RISE Germany-USA** . . . . . *2014*  
*(Research Internships in Science and Engineering)*

## Publications

6 peer-reviewed publications in scientific journals. 1 conference proceedings.